UNIVERSITA' DEGLI STUDI DI NAPOLI "FEDERICO II"

TESI DI DOTTORATO DI RICERCA IN

TECNOLOGIE INNOVATIVE PER MATERIALI, SENSORI ED IMAGING

Lidar study of high density aerosol clouds: The Aerosol Multi-wavelength Polarization Lidar Experiment

Tesi di dottorato di
Gianluca Pisani

Tutors
Prof. Nicola Spinelli
Dr. Xuan Wang

XXV CICLO

ANNI ACCADEMICI 2010-2013

Coordinatore: Prof. Luciano Lanotte

Introduction

Atmospheric aerosols considerably affect the Earth's radiation balance and are considered at present one of the major source of uncertainty in climate forcing predictions. Their concentrations and properties are still poorly known[1]. The geoscience community requires continuous observational data to monitor and understand suspended particles and to initialize, validate and improve dispersal models. In particular, the aerosol scientists are still struggling with the problem that an adequate amount of spatially and temporally widespread observations does not exist. To study the climate change, weather forecast and environmental pollution associated with fine particles, volcanic ashes transport information on aerosol sources and synoptic scale measurements (possibly with a time series perspective) are hence necessary. For these reasons, the knowledge of aerosol distribution and atmospheric residence time is necessary.

Aerosols can be detected by measuring their light scattering or absorption properties. Hence, remote sensing can act as a powerful tool to investigate atmospheric aerosol properties. For instance, air/space-borne remote sensing for atmospheric research is currently being used to measure columnar properties of water vapour, carbon dioxide, cloud and aerosols from local to large scale. By the way, these methods cannot resolve locally the vertical distribution of the absorbing species, which can be located at every distance from the sensor in the measured column.

Light detection and ranging (lidar) is one of the most effective tools to study and profiling Earth's atmosphere. The lidar seems to be an ideal sensor to monitor the atmospheric constituents in 4D (space and time) since it allows to obtain high spatial and temporal resolution, near on-line data availability and high range sounding distance (several tens of kilometres of altitudes). It basically consists of a transmitter and a receiver. Short laser pulses (which wavelengths range from near UV to far IR) are fired into atmosphere and a telescope collects backscatter photons; hence the latter are spectrally analysed to obtain a great deal of information on the basis of the lidar specific application[2]. Range resolved measurements performed by single wavelength elastic lidar can retrieve only few aerosol properties, while the estimation of microphysical properties requires measurements of both backscatter and extinction coefficient, possibly at several wavelengths[3]. Furthermore, simultaneous measurements of the depolarization signal and water vapour mixing ratio are particular useful to

correlate aerosol optical properties with their shape, thermodynamic phase and hygroscopicity. Moreover, scanning capability of lidar devices can dramatically improve the possibility to monitor the aerosol volume distribution by 4D mapping of the atmosphere. Moreover, aerosols can be used as a tracer for other substances. Hence, in the monitoring of pollution by employed lidars in a network, they can provide information about air masses trajectories. To this point, it is clear the importance of the knowledge the atmospheric dynamics in order to manage the problem of air pollution, which of course depend both on the type of polluting source and on the chemical reaction occurring during the transport of pollutants.

In this work a particular effort has been devoted to the study and measurement of the aerosol produced during volcanic activities. The interest in this study comes from the volcanic ash clouds large dispersion scale and long residence times, since these particles represent a serious hazard to aircraft engines. In fact, recently, the Eyjafjallajökull volcano eruption in Iceland raised this problem, demonstrating the high vulnerability of the human flight transport system. Since lidar measurements can detect and map aerosol layers and, under suitable conditions, allows estimating the column height, such data represent key elements to reliably forecast plume dispersal using volcanic ash transport and dispersal models[4]. Furthermore, from lidar measurements ash mass concentrations with a certain degree of uncertainty can be evaluated. This parameter together with depolarization measurements can contribute to discriminate volcanic ash from desert dust, so having a potential strong influence on air-traffic decision management.

On the other hand, it is well know that Eastern Asia is one of the major sources of anthropogenic pollutants as well as of wind-blown mineral dust aerosols. Since the properties of pollution aerosols (not associated with dust) are poorly known, to better understand the influence of two aerosol components on the East Asia environment, a systematic investigation on the aerosol properties for both pollution and dust particles is needed.

In this context, the National Consortium for Physical Sciences of the Matter, CNISM, Unit of Napoli activated two scientific cooperation programs with Istituto Nazionale di Geofisica e Vulcanologia, INGV, Section of Catania, (Italy) and the Beijing Research Institute for Telemetry, BRIT, (People's Republic of China) to furnish two lidar system suitable for the specific operational contest.

Hence, the main objective of this thesis is the implementation of a new, versatile and portable scanning lidar system to be used as sensor to carry out 4-D (space and time) profiling of the atmospheric aerosol distributions, their optical properties, and microphysical characterization. The device was delivered in two copies; the first was installed on the slope of the Mt. Etna at the astronomical observatory of Serra la Nave (Catania, Italy) (in cooperation with Istituto Nazionale di

Astrofisica, INAF, Sezione di Catania) and the second was installed in Beijing, at BRIT to monitor the urban atmosphere. Hopefully, the new lidar devices should contribute to make a point in to the unresolved issue of the distinction between the anthropogenic contribution and natural sources to the atmospheric particulate. Indeed, the typing of the atmospheric aerosol and the investigation of their nature require the study of the spatial-temporal distribution of their optical and microphysical properties. The outline of this thesis is as follows: in the first chapter a general description of the scientific problem of the aerosol detection and monitoring in the Earth's atmosphere is done. The second chapter is used to describe the physical principle of the lidar technique based on light-matter interactions. Then, the lidar equation is developed according to classical literature. In the third chapter it is shown as the lidar equation can be inverted to retrieve the optical proprieties of particles. The fourth chapter is devoted to the description of lidar systems used and to the design of the new AMPLE (Aerosol Multi-wavelengths Polarization Lidar experiment) system. Finally, results of the field campaign and preliminary analysis are done in chapter 5.

1. Lidar Atmospheric Sensing

Earth's atmosphere is a complex and huge thermodynamic system, which can be modelled with a higher precision as long as new details are considered and implemented in the model. In particular, it is a mixture of several gases, whose principal components are listed in Tab. 1.1. It is interesting to note that in the 1% of "trace gases" are responsible for the main characteristics of atmosphere and that they drive some fundamental processes. For instance, water vapour is extremely variable with latitude and altitude and can vary from some parts-per-million (ppm) in the desert regions to some parts-per-thousand in tropical regions. Together with carbon dioxide and methane, the water vapour is the main responsible for the greenhouse effect. Besides, the ozone layer (mainly located in stratosphere) shields Earth's surface from ultra violet radiation and prevents damages of biological tissues.

Tab. 1.1. Chemical composition of Earth's atmosphere. In the last two columns the principal production and destruction processes of gases are showed. (Adapted from Visconti G.)

Gas	Percentage (f_i) %	Source	Sink
N_2	78.1	biological	biological
O_2	20.9	biological	biological
Ar	0.0093	degassing	
H_2O	<0.04	evaporation	condensation
CO_2	0.0034	combustion, biol.	biological
$^{36,38}Ar$	0.000037	degassing	
$^{20,22}Ne$	0.0000182	degassing	
CH_4	$1.7 \div 3 \cdot 10^{-6}$	biological	photo-oxidation
N_2O	$3.1 \cdot 10^{-6}$	biological	photo-dissociation
CO	$0.4 \div 2 \cdot 10^{-7}$	photochemical	photochemical
O_3	$0.1 \div 1 \cdot 10^{-7}$	photochemical	photochemical
NO, NO_2	$0.2 \div 5 \cdot 10^{-10}$	combustion, biol.	photo-oxidation
SO_2	$3 \cdot 10^{-10}$	combustion	photo-oxidation

In addition to those quoted types of gases, aerosols must be considerate as atmospheric constituents since they play an important role in the atmospheric dynamic and energetic balance. Processes of scattering and absorption by particles, both in aerosols layers and clouds, play a major role in regulation of Earth atmosphere radiative balance. Hence, in the last decades, a large number of studies have been carried out aiming to understand direct and indirect effects of aerosol on the radiation budget and to reduce the uncertainty in climate forcing studies[5]. A great effort at the international level has gone in coordinating systematic observations of aerosol optical parameters and of their profiling[6,7]. Moreover, high interest has been devoted to develop and implement new and enhanced sensors[8,9,10] and to improve numerical forecasting models[11,12].

1.1 Atmospheric monitoring

Concerning the study and the characterization of Earth's atmosphere, different kinds of monitoring techniques have been developed. The different adopted procedures allow to distinguish *"in situ"* and *"remote sensing"* techniques. The former ones allow obtaining direct information on single and limited air parcel, with direct contact between technical instrument and sounded atmospheric volume. On the other hand, the last ones allow collecting data on the entire air column (profiling) without a modification of the target, because such kind of measure is based on optical analysis techniques. Remote sensing techniques have been undergone a quick development after the invention of lasers; in fact, such kind of tools are based on radiation-matter interaction. So, they can warrant extremely high selectivity and sensibility and they aren't invasive. Furthermore, in some cases, remote sensing techniques can furnish a continuous time monitoring of the target.

Generally speaking, remote sensing techniques can be distinguished in *passive* and *active*. The first kind provides only the detection of the electromagnetic field from the object, while the second one provide both the emission of electromagnetic field with specific, well known characteristic (wavelength, amplitude and phase…), and the detection of the radiation coming out from object, whose characteristics contain the physical information of interest. For passive sensing, the analysis of the fluctuation of signal and its spectral characteristics are needed in order to extract the physical information about the object. On the other hand, for active sensing, those characteristics are incorporated both in the amplitude of the produced signal, and in its phase distortion. Along with the coherent mode, for active sensing incoherent sources are available as well, but of course they do not allow to handling the phase of the e.m. field.

The obvious advantage of the passive remote sensing in the atmospheric measurements techniques is in the use of natural radiation (mostly the Sun light). The detected signal is, hence, produced by spontaneous transition between roto-vibrational levels of gases molecules. The main instrumental category used in that kind of measure is the radiometer. Artificial light used in the active remote sensing have the possibility of using it as required for the specific experiment, even if, when airborne or space borne instrument are considered, specific power supply needs to be considered. Finally, one of the main advantages of active remote sensing is the possibility of sampling the radiation path to obtain spatial profiling of the chosen physical parameter.

1.2 Atmospheric aerosol

An aerosol is an extended colloidal dispersion of solid or liquid particles in a gaseous medium, such as smoke, fog, sea salt, soil dust, combustion products, etc.. Aerosols can vary greatly in concentration,

chemical composition, as well as dimensions, making them difficult to measure and model. The crucial role in the climate system of aerosol is one of the major uncertainties of present climate predictions, so aerosol, together with clouds, could have a fundamental influence in climate change. In fact, the aerosols role in atmospheric chemistry and their effect on other potentially harmful atmospheric constituents, e.g. ozone, are still unclear. Aerosols influence the Earth's radiative balance, acting directly in UV part of the spectrum and indirectly as clouds condensation nuclei. Aerosols can have relevant effects on human life as well, because of their harmfulness or toxicity. Afterwards, it is necessary to understand the generation, transport and removal processes of atmospheric aerosols. Furthermore, the different types of clouds are responsible for almost 50% of the coverage of the sky[13] and in some cases they act as greenhouse gas by reflecting part of the solar radiation and absorbing thermal radiation from Earth. The incomplete knowledge of clouds properties and characteristics is another important source of uncertainty in climate change prediction[14].

Aerosol types have been classified by size, by geographical region of formation, and by production mechanism. Junge[15] classified aerosols by their geographical source region: maritime, continental, and background. Whitby[16] categorized aerosols into groups according to their production mechanism. The various production mechanisms include gas-to-particle conversion, growth and coagulation, sea spray, wind-blown effects, anthropogenic emissions, and meteoric dust.

The gas-to-particle conversion processes are responsible of the generation of ultrafine particles. In fact, when in free atmosphere the vapour concentrations are sufficiently high, particles may be formed by homogeneous nucleation. Particle formed by this process have a range size between 0.001–0.1 μm. This process usually occurs when photochemical processes are active, so for new particle formation clear sky and dry condition are required[17]. Concentration of newly formed particles has been found to correlate with solar irradiance and ambient concentrations of H_2SO_4. On the other hand, ultrafine particles are produced by combustion processes in automobile engines and heavy industry. Among sources of intermediate size particles, they have to be included combustion and chemical transformations of gases to produce secondary products: sulphates, nitrates, and organics. Wind-blown effect is the major responsible for generation of particle larger than 2.5 μm. For instance, wide amount of desert dust aerosol (about 1000Mt/yr) is formed by dust particles produced by wind erosion in desert areas. Since from the early seventy, several studies show that dust storms are the main event responsible for soil aerosol injection in the Earth's atmosphere[18, 19].

Tropospheric particles cover a wide size range spectrum, starting from molecular clusters (~1 nm), and ending to particles greater than 100 μm in diameter (hydrometeors). As figure 1.1a shows, the ultrafine particles have the maximum particle number concentrations in the dimensional spectrum; such particles are nominally smaller than 0.1 μm in diameter and are originated from combustion and

nucleation processes. Of course, the ultrafine mode contains the most particles; nevertheless such mode generally contains negligible mass (volume) and little surface area with respect to other modes. So it needs to have many particles in this mode to affect the optical scattering intensity. On the other hand, aerosol volume distribution (figure 1.1b) is dominated by fine and coarse particles, also denoted as $PM_{2.5}$, which define the mass concentration of particles with effective diameter smaller than 2.5 μm. Finally, coarse particles are designates by label PM_{10}, and they are defined as the total mass concentration of particles with size up to 10 μm. Beside, from figure 1.1b it is clear that the coarse mode particles are the least plentiful in number, nevertheless they are responsible for the majority of the visibility degradation and the majority of aerosol volume in the troposphere. Anyway, due to their large size and weight, coarse mode aerosols generally fall out rapidly from the atmosphere because of gravitational settling[20, 21].

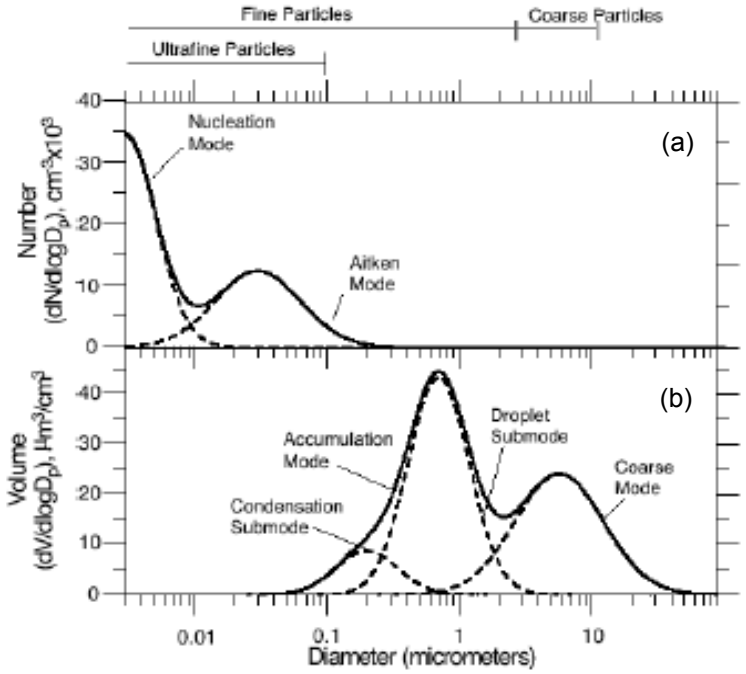

Fig. 1. 1 Number and volume distributions for atmospheric aerosol [Part. Mat. Sc., 2003].

Concerning the particles role in the atmospheric dynamic, here it should be stressed that they have an important role as tracers of dynamic itself. For instance, natural and anthropogenic aerosols participate to turbulent motion of planetary boundary layer (PBL) defining its height because of gradient of aerosol concentration between PBL and free troposphere[22]. Beside, an important role is played by aerosol on the synaptic range: in fact, aerosols are involved in long range transport event, as desert dust outbreaks or volcanic ash plumes long range transport. Figure 1.2 (a) and (b) shows two examples of such events.

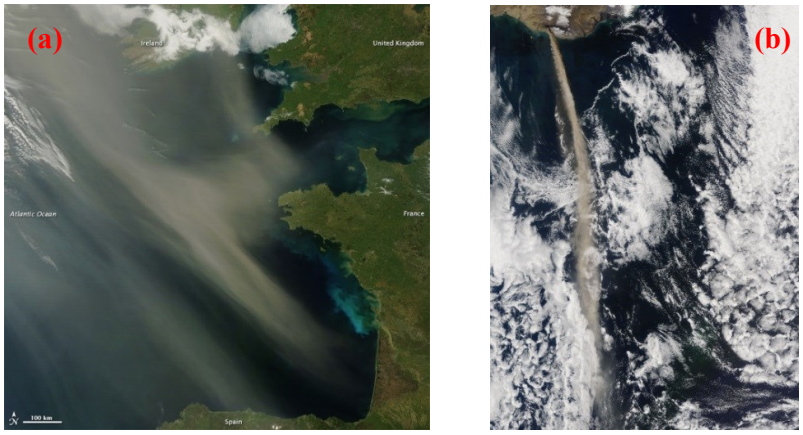

Fig. 1. 2 Two examples of natural-color images from the Moderate Resolution Imaging Spectroradiometer (MODIS) on NASA's Terra satellite. (a) On April 8, 2011, a desert dust plume from Sahara is travelling on Atlantic Ocean northward toward the United Kingdom and Ireland. (b) On May 11, 2010, the ash plume from Iceland's Eyjafjallajökull Volcano was streaming almost directly south, visibly extending almost 900km from Iceland [http://visibleearth.nasa.gov/view_rec.php?id=2197]

1.3 Sounding the atmospheric aerosol by lidar

Due to their vertical distribution and composition, atmospheric aerosol and clouds are the ideal targets to be study by LIDAR (LIght Detecting And Ranging, from now on *lidar*). Lidar technique is based on the same principle of the RADAR (RAdio Detecting And Ranging). The lidar technique consists in the transmission of a short light pulse toward the target and in the analysis of the backscattered radiation. The figure 1.3 shows the principle of a lidar measure. Briefly, it consists on both the measure of the time of flight for light pulse to return back to the receiver allows determining the distance of the target and the analysis of the intensity and of the spectral distribution of the detected radiation. This last can gives information about the optical properties of the target.

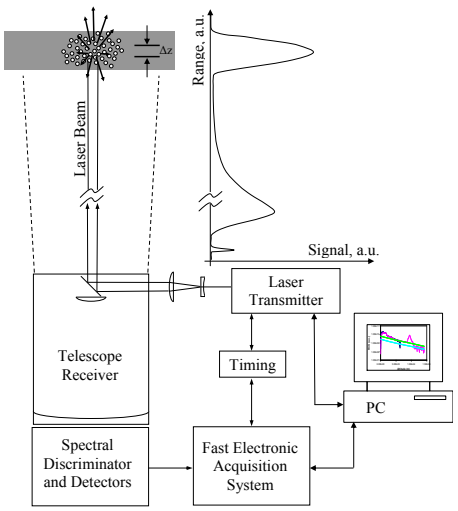

Fig. 1. 3 Schematic drawing of the LIDAR setup. The distance of the target is obtained by measuring the time elapsed between the transmission of the laser beam and the detection of the backscattered radiation. The spatial resolution of the measurement depends on the laser pulse duration and the time resolution of the electronics.

Lidar applications are related to climatological studies, as well as to agricultural and forest monitoring, to archaeological and architectonic heritage monitoring, to range finding and terrain mapping, to bathymetry and to several others non-scientific applications as the traffic speed law enforcement for vehicle speed measurement.

The first lidars were based on ruby lasers and were used for atmospheric studies related to composition, structure, clouds, and aerosols. The improvements in the lasers technology has been crucial for the lidars development and the characteristics of laser presently available allowed to free the huge potential of laser remote sensing.

The most direct implementation of the lidar principle is in range finding devices, which allow high resolution measurements of the target's distance and its reconstruction in a 3D image or map. In this field particular relevance have the air-borne systems. In those devices, the laser beam in fired directly toward the Earth's surface utilizing scanning technology so that the lidar can probe the ground sweeping in orthogonal direction with respect to the line of flight. The collected data can then be used to create a high-resolution 3D model of ground surface (Digital Terrain Model – DTM), which are extremely accurate (accuracy of the order of the mm- and cm-) because of the short duration of the laser pulse and precise sensor platform orientation and position that is guarantee by differential GPS with at least two stations[23].

Mainly, the scientific applications of lidar technology is based on elastic and inelastic (Raman) scattering from particles and gases. Different levels of knowledge of the aerosol properties can be achieved by arranging different configurations of the lidar system making it sensible to specific optical interactions. The first type is typically used for aerosol and cloud detecting: backscattered radiation is detected at the same wavelength of the transmitted laser beam. On the other hand, Raman lidars are used to identify specific gas of interest so allowing independent quantitative measurements of the aerosol backscatter and extinction coefficient profiles. Further information about geometrical properties and thermodynamic state of the aerosol particles can be retrieved from the measurement of the changes of the polarization status of the backscattered radiation with respect to the incident beam. Particular set up of lidar allow to measure the speed of the target. In fact, lidars based on Doppler effect can be used to measure wind speed along the beam by measuring the frequency shift of the backscattered light.

The lidar technique is, actually, recognized as a well-established tool for aerosol profiling since it gives detailed information on the particle properties with high vertical and temporal resolutions. Hence, in the last decade, backscatter and Raman lidar have been and are still used (especially if used in a network) to carry out a large number of studies aiming to understand direct and indirect effects of aerosol on the radiation budget, to reduce the uncertainty in climate forcing studies due to the aerosol, and to contribute to the understanding of aerosol generation, their long range transport, and their

contribution to clouds modifications. Of course, these measurements can help to improve physics model treatment of atmosphere and satellite data retrieval since it is know that satellite data could suffer for aerosol bias.

An elastic backscatter lidar typically uses laser sources from near UV to near IR spectral range. The main scientific objective of such a simple configuration is to define the height, structure and time evolution of aerosol layers in the atmosphere[24].

The aerosol content in the atmosphere is related to the aerosol backscatter coefficient, which profile can be obtained from elastic lidar measurements by following the Klett-Fernald retrieval methods (see chapter 3). This method requires a hypothesis on the extinction-to-backscattering ratio (L), which depends on chemical composition, refractive index, shape, and particles size distribution[25]. An elastic backscatter lidar also allows to follow the temporal and spatial evolution of aerosol layers by means of long records of vertically resolved profiles being so it is a basic tool for monitoring of long range transport events. Together with the elastic configuration, the depolarization lidar technique can be considered as one of the best tools to discriminate between liquid and solid aerosol particles. An example of global measurement coverage of clouds properties are presently derived from the NASA space-borne lidar CALIPSO (Cloud-Aerosol LIDAR and Infrared Pathfinder Satellite Observation)[26], which main goal is to determine the base and the top of the clouds and aerosol layers and their overlap, identify the composition of clouds and the presence of sub-visible (or "invisible" clouds), and to estimate the abundance and sources of aerosols[27]. Being the lidar on board of CALIPSO a backscatter system, it cannot provide direct measurement of measurements of aerosol optical properties profiles.

Advanced Raman lidar systems can provide a more relevant scientific contribution to monitor aerosol optical and microphysical properties. In fact, the simultaneous measurement of the elastic and the Raman nitrogen (or oxygen) molecules backscatter signals allows measuring independently the profiles of both particles extinction and backscattering coefficients. The spectral dependence of backscattering and extinction coefficients obtained through multi-wavelength Raman lidar also allow to estimate the aerosol particle size. Furthermore, aerosol typing is possible by using multi-wavelength Raman lidar measurements.

A very interesting application of Elastic/Raman lidar is the study of the evolution of potentially hazardous aerosols as dust aerosol or ashes from volcanic activities. For instance, long-range transport events of mineral dust were simultaneously monitored both close to the Sahara desert and far away from source region, in order to evaluate geometrical and optical properties of that dust plume[28,29]. Those field campaigns provided also a good opportunity to analyze the impact of dust on cirrus cloud formation[30]. Moreover, although large continental-scale dust plumes from Gobi desert and high anthropogenic pollution from industrial districts in Asia contribute to modify the Earth's climate balance[31], the ability to quantify these effects has been limited by a lack of field observations in these regions.

Furthermore, since from the first observations of airborne volcanic ash layers in the 1990s, recently it is grown the interest in the study of volcanic ash plumes dispersion. Lidars have improved our knowledge in this topic and, in particular, the depolarization technique has been used to distinguish shape and thermodynamic phase of atmospheric aerosol[32,33,34]. Moreover, under suitable conditions, lidar measurements may estimate the column height of the volcanic plume so allowing to improve the reliably of plume dispersal forecast using volcanic ash transport and dispersal models, as well as the evaluations of the ash mass concentration emitted plume. In this sense, the eruption of the Icelandic volcano Eyjafjallajökull in April/May 2010 represents a perfect example of the capability of a lidar network to evaluate the impact of volcanic emissions on a continental scale[35].

2. Lidar technique

Ground-based elastic lidar can be used to provide height- and time-resolved measurements of atmospheric aerosol properties like backscatter coefficient, depolarization ratio, and a measure of multiple scattering. Raman lidar can also use to measure aerosol extinction, water vapour, temperature, and ozone profiles. Physical principle of lidar is the scattering of light from atom, molecules, and aerosol in atmosphere. The idea to use light as a sound for atmospheric components analysis is preceding laser invention. Laser has been utilized for first time in atmospheric remote sensing by Fiocco and Smullin[36] in 1963, when they measured week lidar echoes from high altitude (60 km) clouds. Then, in 1967, Barrett e Ben-dov[37] showed the possibility to use lidar to measure atmospheric pollutants and retrieved particles concentration profiles up to 1.5 km. Finally, Collis[38]proposed several investigation fields for lidar including studying of high clouds structure, atmospheric turbulence, gravity waves, and planetary boundary layer dynamic. From that it can be evicted the extreme flexibility of lidar technique to sounding and retrieving atmospheric optical properties. A short overview of involved physical processes is described in the following lines.

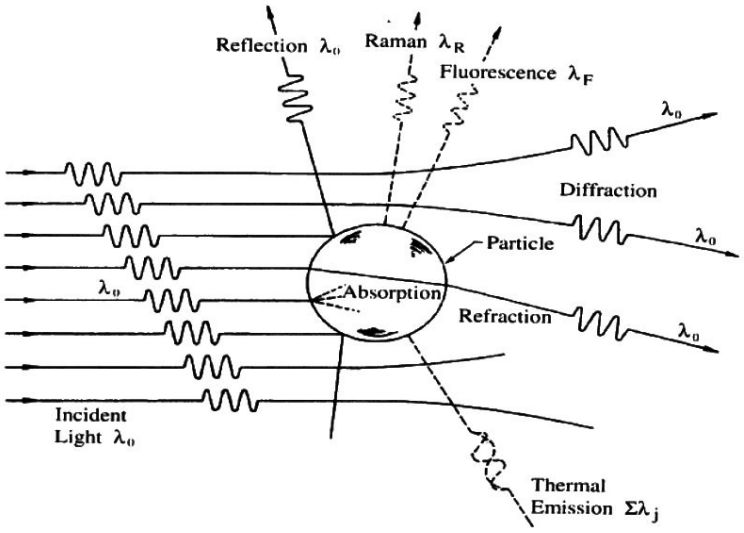

Fig.2. 1 Mechanisms of interaction between incident radiation and a particle. From Seinfeld and Pandis, 1998.

Figure 2.1 the processes that occur when radiation of wavelength λ_0 interacts with a target (molecule or particle). When the incoming beam impinges on a target, electric charges are excited into

oscillatory motion. The excited electric charges re-radiate energy in all directions (scattering) and may convert a part of the incident radiation into internal energy (absorption).

2.1. Scattering

When a target is situated on path of electromagnetic wave the scattering process occurs (Figure 2.1). This process is the subtraction of energy from incoming field to irradiate in neighbour space that is defined by solid angle centred on the scattering target. Process take place if e.m. wave undergoes a discontinuity in propagating medium, namely if complex refraction index of the target is different with respect to that one of the propagating medium.

The dimensions of aerosol suspended in the Earth's atmosphere can cover a wide range of amplitude. Furthermore, aerosols are composed by different type of particles that are different for shapes, dimensions, chemical and physical properties, so the theory of light scattering is rather complex and it vary according to the dimensions of target considered. The ratio between linear dimension of scattering particle a and the wavelength of incoming light λ is a common parameter of appropriate theories. Indeed, if a is much lower than λ, as for atmospheric gas molecule, radiation is scattered in space by target as $(1+\cos^2\theta)$ (being θ the scattering angle between incoming and scattered radiation), its intensity is proportional to λ^{-4} and it can be described by Rayleigh theory. As long as dimension increases a maximum of intensity of scattered light appears in forward direction. When a is much greater than λ, the intensity of scattered is almost wavelength independent and then Mie theory shall be used. Finally Raman theory describes anelastic scattering by atmospheric gasses.

2.1.1. Scattering Rayleigh

Rayleigh scattering refers to the light scattering from the air molecules, and can be extended to scattering from particles up to about a tenth of the light wavelength. In this model molecules are assumed spherical, and isotropic. Molecular scattering can be explained with absorption and subsequent emission of radiation from a molecule. Definitely, it could be considered as an anelastic (because there is absorption of incoming photon) and resonant (because the energy of incoming photon is equal to energy acquired by molecule) process. In the classical model, the molecule is represented by harmonic oscillator located in the origin of the coordinate system, with a single valence electron bounded enough to be influenced by electric applied by e.m. incoming wave $\vec{E}$. Naming α the polarizability the dipole moment produced by incoming electric field is $\vec{\mu} = \alpha\vec{E}$. For the incoming linear polarized and monochromatic e.m. wave (like laser beam), electric field can be express in terms of its angular frequency and a unit polarization vector $\hat{\varepsilon}$, $\vec{E} = \hat{\varepsilon}\, E_0 \exp[-i\omega t]$, being E_0 incoming electric field amplitude, ω the angular frequency of incoming wave.

As long as electric accelerated charges produce electromagnetic waves, electron forced to oscillate by e.m. wave is subjected to radiate an electric field (scattered field). For sinusoidal incoming e.m. wave, at distance *r* from oscillating electric dipole, the intensity of scattered radiation is:

$$I(\theta) = \frac{1}{16\pi^2 \varepsilon_0 c^3} \frac{\sin\theta}{r^2} \left(\frac{d^2\mu}{dt^2} \right)^2 \tag{2.1}$$

where θ is the observing angle between dipole axes and observing direction. If eq. (2.1) is integrated on the entire solid angle, the total scattered power is:

$$P = \frac{1}{6\pi \varepsilon_0 c^3} \left(\frac{d^2\mu}{dt^2} \right)^2 \tag{2.2}.$$

For sine wave, dipole moment is $\mu = \alpha E_0 \sin(\omega t)$, which, substituted in (2.1) and (2.2), furnish the average intensity and power scattered at the direction θ:

$$I(\theta, \lambda) = \frac{c\pi^2}{2\varepsilon_0 r^2 \lambda^4} \alpha^2 E_0^2 \sin^2\theta \tag{2.3}$$

$$P(\lambda) = \frac{4c\pi^3}{3\varepsilon_0} \frac{\alpha^2 E_0^2}{\lambda^4} \tag{2.4}.$$

The last two expressions give the general formulation for single dipole Rayleigh scattering. It should be stressed following points:

1. intensity and power of scattered wave are directly proportional to fourth power of the inverse of the wavelength of the incoming radiation;
2. there is no scattered radiation along the dipole axes path.

Now, to quantify the efficiency of the scattering process, a new parameter shall be introduced. It is defined as the ratio of scattered power in the solid angle unit around direction θ and the intensity of the incident e.m. wave. Such a parameter is known as *differential scattering cross section*. For sine wave it is:

$$\frac{d\sigma(\theta, \lambda)}{d\Omega} = \frac{I(\theta, \lambda)}{\frac{c\varepsilon_0}{2} E_0^2} = \frac{\pi^2 \alpha^2}{\varepsilon_0^2 \lambda^4} \sin^2\theta \tag{2.6}.$$

that describes the behaviour of differential scattering cross section. Actually, when the angular frequency of incoming wave ω approaches the molecule resonance angular frequency ω_0, the differential cross section becomes large, then the process is very efficient. Instead, when incident wave has an angular frequency far from ω_0, the scattering process loses efficiency because of the decreasing of cross section.

Previous formulation is valid for single dipole (atom or molecule), while for real atmospheric case the number density of scatterers N has to be introduced. Afterwards, if *n* is the refractive index of the medium, the following expression can be obtained for σ:

$$\sigma(\theta,\lambda)=\frac{9\pi^2}{N^2\lambda^4}\left(\frac{n^2-1}{n^2+2}\right)^2\sin^2\theta \qquad (2.7)$$

The total cross section for Rayleigh scattering process is derived integrating the eq. (2.7) on all the solid angle:

$$\sigma(\lambda)=\frac{8\pi}{3}\left[\frac{\pi^2\left(n^2-1\right)^2}{N^2\lambda^4}\right] \qquad (2.8).$$

The already emphasized λ^{-4} dependence of the process is at the origin of much of visual effect in the Earth's atmosphere, first of all the blue sky. The sky blue colour is caused by Rayleigh scattering of sunlight from atmospheric molecules. In fact, scattering at the shortest wavelength of the visible spectrum is more efficient that for longer ones giving the appearance of blue sky at large angles with respect to the direction of the sun's light. Another nice visual effect explained with Rayleigh scattering is red sun during sunset and sunrise. It happens because of short wavelengths are scattered out of the beam of sunlight before it reaches observer, so red component of spectrum is more visible.

Anyway, the fraction of scattered radiation interesting in lidar remote sensing is the *backscattered* one, i.e. that one scattered at an angle of π with respect to the laser beam. The backscattering cross section is obtained for θ = 180°:

$$\sigma^{\pi}(\lambda)=\frac{\pi^2\left(n^2-1\right)^2}{N^2\lambda^4} \qquad (2.9).$$

To take into account the numeric density of scatterers is more convenient to introduce the backscatter coefficient defined as the product of cross section σ and numeric density N. Afterwards, the backscatter coefficient is:

$$\beta^{\pi}(\lambda) = \frac{\pi^2 \left(n^2 - 1\right)^2}{N\lambda^4} \qquad (2.10).$$

For atmospheric gas mixture and under 100 km the Rayleigh backscattering cross section has been studied[39] and the following wavelength dependence has been found:

$$\sigma^{\pi}(\lambda) = 5.45\left(\frac{550}{\lambda(\mu m)}\right)^4 \cdot 10^{-28} cm^2 sr^{-1}.$$

Then, if the density profile is known, the molecular backscatter coefficient profile can be evaluated from (2.10).

2.1.2. Mie Scattering

Scattered light from particles (aerosols) does not follow Rayleigh rule because of large size (a is not much lower than λ). The theory to describe their scattering becomes extremely complex as the particle dimension approaches the wavelength of incident light λ. So, it is convenient to define a *size parameter* $x \equiv k\,a = 2\pi\,a/\lambda$. For small isotropic dielectric targets (x<0.5), scattering properties can be derived from Rayleigh theory. Indicating the polarization angle with φ, the corresponding differential cross section is:

$$\frac{d\sigma(\theta,\varphi,\lambda)}{d\Omega} = a^2\, x^4 \left(\frac{n^2-1}{n^2+2}\right)^2 \left(\cos^2\varphi \cos^2\theta + \sin^2\varphi\right) \qquad (2.11).$$

Again, from (2.11) the backscattering cross section is obtained for θ = π:

$$\sigma^{\pi} = a^2 \left(\frac{2\pi}{\lambda} a\right)^4 \left(\frac{n^2-1}{n^2+2}\right)^2 \qquad (2.12).$$

As it appears from (2.12) the dependence from the inverse of fourth power of wavelength is kept as in Rayleigh scattering; this mean that the spectral dependence of the scattering from very small dielectric target is equal to that one from molecules. The main difference between the two processes is the magnitude of scattering. Actually, the larger is the dimension of target, the larger is the cross section. So, scattering cross section increases with the dimension of dielectric particles.

Above the value of 0.5 for particle size parameter, the scattering process becomes very complex: the cross section is then a complicated function of x, n and θ. The first attempt to describe the scattering theory for large particle is due to Gustav Mie, who derived formal rigorous solution that is valid only for spherical particles. Nevertheless an approximate derivation can be considered[40]. As a

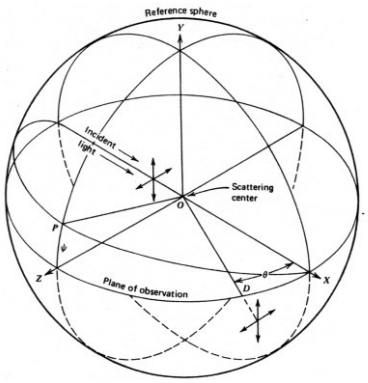

Fig. 2. 2 Mie scattering geometry.

matter of fact, particles scattering process can be considered as a scattering process from each single dipoles that go to make up the entire particle, and for which the theory is known. Then the resulting scattered wave can be considered as the sum of the single scattered waves from fundamental dipoles. Actually, each fundamental dipole is subject to incoming wave and each of them emits a secondary wave. By calculating the interference of partial waves as a function of the observing angle, it is possible to know the scattered intensity. Due to the fact that the size of large particle is often much larger than wavelength, the phase of each partial wave will depend on the phase of incoming wave of fundamental dipole. Afterwards, the intensity of interference pattern will be a function of temporal and spatial phase difference. This implies that the intensity of scattered light will depend from the observing angle. This can be seen by considering the geometry of Mie scattering (Fig. 2.2). N particles are placed in unitary volume, which is in the centre of Cartesian reference frame. An incident light beam is travelling on path defined by X axes and the detector D is placed far from particles, so that the distance OD is large if compared with linear dimension of unitary volume containing particles. θ is the angle between X axes and OD (observing angle). The intensity of scattered light at angle θ can be considered as the sum of the intensity of *p* (parallel to plane observing XZ) and *s* (perpendicular to plane XZ) polarized components $I_p(\theta)$ and $I_s(\theta)$, respectively. Such intensity components are proportional to two distribution intensity functions i_1 and i_2, which are expressed as following series:

$$i_1(x,n,\theta)=|S_1|^2=\left|\sum_{j=1}^{\infty}\frac{2j+1}{j(j+1)}\left(a_j\pi_j+b_j\tau_j\right)\right|^2=|\,\mathrm{Re}(S_1)+\mathrm{Im}(S_1)\,|^2$$

$$i_2(x,n,\theta)=|S_2|^2=\left|\sum_{j=1}^{\infty}\frac{2j+1}{j(j+1)}\left(a_j\tau_j+b_j\pi_j\right)\right|^2=|\,\mathrm{Re}(S_2)+\mathrm{Im}(S_2)|^2$$

where:

- x is the particle size parameter;
- n is the particle complex refractive index;
- S1 and S2 are complex amplitudes of observed waves;
- a_j and b_j are Ricatti-Bessel complex functions;
- π_j and τ_j are functions containing the first and second derivative of Legendre's polynomial of j^{th} order.

For linear polarized incoming light beam, if ψ is the polarization angle, then the intensity of plane scattered light is:

$$I(\theta,\psi)=E_\psi\frac{\lambda^2}{4\pi^2}\left(i_1\sin^2\psi+i_2\cos^2\psi\right) \qquad (2.13)$$

That is, the scattered light suffers of a polarization change; in fact (2.13) is the general condition for elliptically polarized light. The limit cases in which $\psi = \pi/2$ and $\psi = 0$, for scattered intensity are:

$$I_s(\theta)=E_s\frac{\lambda^2}{4\pi^2}i_1 \qquad I_p(\theta)=E_p\frac{\lambda^2}{4\pi^2}i_2 \qquad (2.14),$$

respectively. Finally, for unpolarized incident light scattered intensity is:

$$I(\theta)=\frac{I_s(\theta)+I_p(\theta)}{2}=E\frac{\lambda^2}{4\pi^2}\left(\frac{i_1+i_2}{2}\right) \qquad (2.15).$$

The cross section for Mie scattering process can be found similarly to the Rayleigh one. For unpolarized light it is:

$$\sigma(\theta)=\frac{I_s(\theta)+I_p}{2E_0}=\frac{\lambda^2}{4\pi^2}\left(\frac{i_1+i_2}{2}\right) \qquad (2.16).$$

For the real case of scatterers that are different in shape, dimensions, and chemical composition an analysis can be done considering $N(a)$ as the dimensional distribution function of particles, with refraction index n and effective radius in range a, $a+da$. Generally speaking, it is a multi-modal lognormal distribution:

$$N(a) = \sum_{j=1}^{n} \frac{1}{a} \frac{1}{\sqrt{2\pi}\,\ln\sigma_j} \exp\left[-\frac{\left(\ln a - \ln a_{mod_j}\right)^2}{2\left(\ln\sigma_j\right)^2} \right]$$

where j is referred to j^{th} mode, a_{modj} are the size of the j^{th} mode and σ_j are the mode's amplitude. Then, the backscatter coefficient can be considered as the integral over the entire dimensional spectrum:

$$\beta(\theta) = \int_{a_1}^{a_2} N(a)\,\sigma(a,\lambda,n)\,da \qquad (2.17).$$

The dependence of the particles cross section on dimension, wavelength, and refraction index can be expressed as:

$$\sigma(a,\lambda,n) = \pi a^2\, Q(x,n)$$

where $Q(x, n)$ is backscatter efficiency, defined as the ratio of backscatter cross section and geometrical cross section, which dependence from particles dimensional distribution and wavelength is through the size parameter x.

2.1.3. Raman Scattering

In the field of laser remote sensing, Raman lidar represents a powerful tool to detecting and measure atmospheric gaseous component and/or pollutants. Raman effect is based on inelastic scattering of light, which means that light scattered from molecules suffer a wavelength shift. Such a shift is characteristic of the irradiate molecule and depends from the energy of stationary state. Real molecules are complex systems having both translational and vibro-rotational degrees of freedom. In particular, if ω_v is the angular frequency associated to molecule vibrations, then its polarizability α oscillates with the same frequency ω_V:

$$\alpha = \alpha_0 + \alpha_1 \sin(\omega_v t) \qquad (2.18)$$

being α_0 the polarizability at equilibrium. When $\alpha_1 << \alpha_0$ the e.m. wave induced polarizability produce an induced dipole moments:

$$\mu = \alpha_0 E_0 \sin(\omega t) + \frac{1}{2}\alpha_1 E_0 \left[\cos(\omega - \omega_v)t - \cos(\omega + \omega_v)t\right] \qquad (2.19).$$

Each term of (2.19) have a role in total scattering:

- $\alpha_0 E_0 \sin(\omega t)$ is responsible for Rayleigh scattering;
- $\frac{1}{2}\alpha_1 E_0 \cos(\omega - \omega_v)t$ is responsible for Stokes component Raman scattering;
- $-\frac{1}{2}\alpha_1 E_0 \cos(\omega + \omega_v)t$ is responsible for anti-Stokes component Raman scattering;

So, in addition to Rayleigh component, also $\omega+\omega_v$, or $\omega- \omega_v$ components can be observed in the scattered light. Raman scattering can be observed when a sample of gas is illuminated with monochromatic light a frequency ω. When incident photons collide with a molecule, in most cases, the

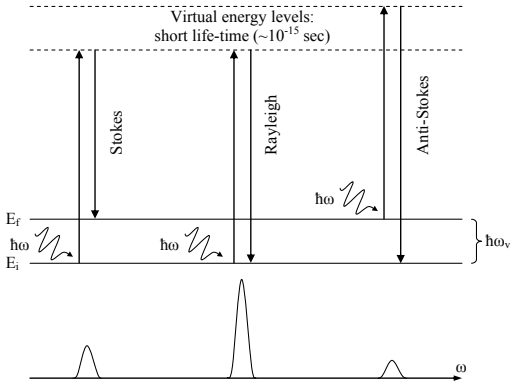

Fig. 2. 3. Energy level diagram for Raman scattering. Different intensity of Stokes and anti-Stokes lines depends from molecules energy level statistical distribution (Boltzmann).

molecule returns to ground state and the photon is scattered with the same energy of the incoming photon, only shifted slightly by the Doppler velocity of the molecule. Nevertheless sometimes, energy is left to the molecule and the scattered photons have lower energy and then longer wavelength. The frequency shifts correspond to the energy quanta associated with the vibrational energy states of the particular molecule. If the molecule is already in an excited state, the photons may gain energy from the molecule by forcing it to return to the ground state: the scattered photons will have increased energy, higher frequency, and shorter wavelength with respect to the incident photons. Energy level diagram is showed in figure 2.3 to explain the process. An incident photon (ħω) can excite molecule from initial energy level E_i to a virtual energy level. When the molecule decays, it can return to E_i or to E_f, which is shifted by $\hbar\omega_v$ from E_i. The energy difference is transferred to emitted photon. The line with lower energy (with respect to ħω) is called Stokes line, while the higher energy line is the anti-Stokes line. Because of the selection rules not all transitions between vibrational levels are allowed. If v is the quantic number for vibrational level, only transition $\Delta v=\pm 1$ are allowed.

For rotational motions of the molecules a similar to (2.19) expression can be obtained. In this case Raman frequency shift for scattered photon will be $2\omega_r$, where ω_r is angular frequency of the rotation of molecule. The selection rules allow transition only if $\Delta J=0, \pm 2$.

It is important to underline that the energy difference E_f - E_i is characteristic for each species, therefore the measurement of such a difference furnishes a direct identification of the specie itself. The main difficulty to use Raman technique lies in the low value of the cross section, which is about tree order of magnitude lower than that one of the elastic Rayleigh scattering.

2.2. Absorption

To explain gas absorption of e.m. waves, an additional term taking in to account the interaction due to the polarization field that each molecule experiences of neighbours, in addition to electric field applied by electromagnetic wave. If N is the numeric density of medium molecules, and f_0 is the fraction of them that can be excited at frequency ω_0, assuming for electron displacement the solution like $x = x\exp(-i\omega t)$, for dipole moment can be written as:

$$\mu = \frac{e}{m_e \varepsilon_0}\left[\omega_0^2 - \omega^2 - i\,\gamma\,\omega - \frac{N e^2 f_0}{3 m_e \varepsilon_0}\right]^{-1}$$

From the previous relation and recalling that $\varepsilon = \varepsilon_0 + \vec{P}/\vec{E}$ and $n = \varepsilon/\varepsilon_0$, it is possible to know the refractive index:

$$\frac{n^2 - 1}{n^2 + 2} = \frac{N e^2}{3 m_e \varepsilon_0}\left[\frac{f_0}{\omega_0^2 - \omega^2 - i\,\gamma\,\omega}\right] \qquad (2.20).$$

For $n \rightarrow 1$ the case of dilute gasses is obtained and (2.20) can be rewrite as:

$$n(\omega)^2 = \left[1 + \frac{N e^2}{3 m_e \varepsilon_0}\left(\frac{f_0}{\omega_0^2 - \omega^2 - i\,\gamma\,\omega}\right)\right]^2 \qquad (2.21).$$

Afterwards, the refractive index can be divided into real and imaginary parts:

$$n(\omega) = \eta(\omega) + i\frac{\chi(\omega)}{2} \qquad (2.22).$$

The real part (2.24) is the experimentally measurable refractive index, while the imaginary part is related to the molecule's ability to absorb radiation.

A plane electromagnetic wave travelling with phase velocity $v = \omega/k = c/n$ in z-direction is:

$$E(z,t) = E_0\, e^{i(kz-\omega t)}.$$

Form the above discussion it follows:

$$E(z,t) = E_0\, e^{i\omega\left(n\frac{z}{c}-t\right)} = E_0\, e^{i\omega\left(\eta(\omega)\frac{z}{c}-t\right)-\omega\chi(\omega)\frac{z}{2c}} \qquad (2.23).$$

At this point, the *absorption coefficient* can be defined as:

$$\kappa(\omega) = \frac{\omega\chi(\omega)}{c}$$

The irradiance of the considered wave will be then:

$$I(z) = \frac{1}{2}\varepsilon_0 c E_0^2 e^{-\kappa(\omega)z}$$

which is the well-known Lambert-Beer relation. It can be put in the usual form:

$$I(z,\omega) = I_0\, e^{-\kappa(\omega)z} \qquad (2.24)$$

if $I_0 = \frac{1}{2}\varepsilon_0 c E_0^2$ is introduced. From (2.24) it is clear that if a monochromatic plane wave is propagating through a medium, it will attenuate by dI for each elementary thickness dz:

$$dI(\omega) = -\kappa(z,\omega)I(\omega)\,dz$$

At the end of all thickness the irradiance of wave will be:

$$I(z,\omega) = I_0\, e^{-\int_0^z \kappa(\zeta,\omega)I(\omega)\,d\zeta}.$$

The quantity $\int_0^z \kappa(\omega,\zeta)d\zeta$ is denoted as optical depth, while $\exp\left[-\int_0^z \kappa(\omega,\zeta)d\zeta\right] = T(\omega,z)$ is denoted as transmission factor.

2.3. The lidar equation

Only an outline of the mathematical process to derive the lidar equation will be derived here, as the, full theory can be found elsewhere[41].

For a monostatic pulsed lidar system, the measured optical power between the incremental wavelengths of λ, $\lambda + \Delta\lambda$ on an incremental height of z, $z + \Delta z$ is given by:

$$P(\lambda,\lambda_L,z) = \int J(\lambda,\lambda_L,z,r)\cdot\Delta\lambda\cdot\Delta z\cdot dA(z,r)\cdot p(\lambda,z,r) \qquad (2.25)$$

where:

- $J(\lambda,\lambda_L,z,r)$ is the laser induced spectral radiance at wavelength λ, at position r
- λ_L is the laser emitted wavelength
- λ is the revealed wavelength
- Δλ is the observed bandwidth
- $dA(z,r)$ is the element of the laser target area at range z and location r
- $p(\lambda,z,r)$ is the probability that radiance incoming from the element $dA(z,r)$ at wavelength λ will hit the detector.

The probability $p(\lambda,z,r)$ can be written as:

$$p(\lambda,r,z) = \frac{A_0}{z^2}\cdot T(\lambda,z)\cdot\xi(\lambda)\cdot\xi(z,r) \qquad (2.26).$$

where A_0 is the receiver collecting surface, A_0/z^2 is solid angle over which the induced spectral radiance must be integrated, T(λ, z) is the atmospheric transmission factor at wavelength λ over the range z , ξ(λ) is the spectral transmission function of the receiver and ξ(z, r) is the probability for the light coming from the range z and location r in the target plane to reach the receiver (often called *geometrical form factor*), respectively.

Concerning the spectral radiance of target, it depends by the nature of laser radiation and medium, so it can be written as the product of laser irradiance I(z, r) and the volume backscatter coefficient[a] at position r and range z:

$$J(\lambda,\lambda_L,r,z)=\beta(\lambda,\lambda_L,r,z)\cdot I(z,r) \qquad (2.27).$$

The total power returned from range z and detected at time t in the lidar spectral window $\Delta\lambda_0$ is:

$$P(\lambda,\lambda_L,z)=\int_0^z d\zeta \int_{\Delta\lambda_0} d\lambda \int J(\lambda,z,r)\,p(\lambda,z,r)\,dA(z,r).$$

Using (2.25) and (2.27) we obtain:

$$P(\lambda,z)=A_0\int_0^{ct/2}\frac{dz}{z^2}\int_{\Delta\lambda_0}\xi(\lambda)d\lambda\int\beta(\lambda,\lambda_L z,r)\,I(z,r)\,T(z,r)\,\xi(z,r)\,dA(z,r) \qquad (2.28).$$

In lidar remote sensing the band of the observed radiation is narrow (comparable with the laser bandwidth), then $L_i(\lambda)$, and therefore β can be consider as a δ-function of λ. Besides, it can be assumed $\xi(z, r)$ equal to 1 where the field of view of receiving system overlaps the laser beam and zero elsewhere and the laser energy distribution is considered as uniform on the interested surface $A_L(z)$. With such hypotheses the eq. (2.28) becomes:

$$P(\lambda,z)=A_0\,\xi(\lambda)\int_0^{ct/2}\beta(\lambda,\lambda_L,z)\,I(z)\,T(z)\,\xi(z)\,A_L(z)\frac{dz}{z^2} \qquad (2.29).$$

In the general case, for a laser pulse with temporal behaviour described by $\varphi(t^*)$[b], the laser irradiance can be written as:

$$I(z^*)=\frac{E_L\,T(\lambda_L,z)}{\tau_L A_L(z^*)}\varphi(t^*)$$

---

[a] It can be express as a function of emitted and scattered wavelength (λ_L, λ) and target properties (numerical density $n_i(z,r)$, differential cross section $\frac{d\sigma(\lambda_L)}{d\Omega}$, the probability that the backscattered radiation is between λ and $\lambda+\Delta\lambda$ $L_i(\lambda)$ for each species) $\beta=\int_{\Delta\lambda}\sum_i n_i(z,r)\left(\frac{d\sigma(\lambda_L)}{d\Omega}\right)_i L_i(\lambda)d\lambda$.

[b] t^* represents the time needed to the forward edge of laser pulse to go from R* to R and to the scattered pulse to come back to R*, so: $t^*=\frac{2(z-z^*)}{c}$. Beside for $\varphi(t^*)$ results: $\int_0^\infty \varphi(t^*)\,dt^*=1$.

where E_L is the output energy of laser, $T(\lambda_L, z^*)$ is the atmospheric transmission factor at laser wavelength from 0 to z, and τ_L is the laser pulse time width. In these hypotheses, after the elapsed time t, corresponding to range z, from equation (2.32) we obtain:

$$P(\lambda, z) = E_L \, A_0 \, \xi(\lambda) \int_0^{ct/2} \beta(\lambda, \lambda_L, z^*) \varphi(z^*) T(z^*) \xi(z^*) A_L(z^*) \frac{dz^*}{z^{*2}}$$

Since the effective laser pulse length is small ($c\tau_L$) if compared to the sounded range, the integral in the preceding equation becomes simpler and the previous equation can be written as:

$$P(\lambda, z) = P_L \frac{A_0}{z^2} \frac{c\tau_L}{2} \xi(\lambda) \beta(\lambda, \lambda_L, z) \xi(z) e^{-\int_0^z \alpha(\varsigma) d\varsigma} \qquad (2.30).$$

In eq. (2.30) the atmospheric transmission factor $T(z, \lambda)$ has been represented in explicit form according to the Lambert-Beer law. Furthermore, because of two-way path of light, the extinction coefficient is:

$$\alpha = \alpha(\lambda_L, z) + \alpha(\lambda, z) \qquad (2.31).$$

Nevertheless, for elastic scattering (Mie or Rayleigh), the wavelength observed is the same emitted by the laser, then the eq. (2.30) can be written:

$$P(\lambda, z) = P_L \frac{A_0}{z^2} \frac{c\tau_L}{2} \xi(\lambda) \beta(\lambda, \lambda_L, z) \xi(z) e^{-2\int_0^z \alpha(\lambda_L, \varsigma) d\varsigma} \qquad (2.32).$$

In conclusion, the eq.s (2.32) and (2.34) are the most used expressions for lidar equation, but they are valid only in case of single scattering. The former is more general, when the detected wavelength is different from laser emitted one; the latter one describes the special case of elastic scattering.

2.4. The extinction coefficient

Some additional considerations are needed for extinction coefficient α present both in eqs (2.32) and (2.34). Extinction is defined as the total attenuation of a laser beam through the atmosphere due to scattering and absorption by both aerosols and molecules. Afterwards:

$$\alpha = \alpha_{mol} + \alpha_{aer} = \alpha_{mol,abs} + \alpha_{mol,scatt} + \alpha_{aer,abs} + \alpha_{aer,scatt} \qquad (2.33)$$

where:

- $\alpha_{mol,\,abs}$ is the extinction due to molecular absorption;
- $\alpha_{mol,\,scatt}$ is extinction due to molecular scattering;
- $\alpha_{aer,\,abs}$ is extinction due to aerosol absorption;
- $\alpha_{aer,\,scatt}$ is extinction due to aerosol scattering.

Molecular scattering component of extinction can be derived from Rayleigh theory through Rayleigh cross section:

$$\alpha_{mol,scatt} = N_{mol}\sigma_R .$$

Concerning molecular absorption extinction component, it should be underlined that for wavelengths corresponding to molecules absorption lines $\alpha_{mol,\,abs}$ is dominant process. The link between the molecular backscattering coefficient and the total molecular extinction coefficient ($\alpha_{mol,\,abs} + \alpha_{mol,\,scatt} \equiv \alpha_{mol}$) can be derived again from Rayleigh theory:

$$\alpha_{mol} = \frac{\beta_{mol}}{0.119} .$$

Regarding the aerosol's contribution to the extinction coefficient, it can be written:

$$\alpha_{aer}(\lambda) = \int_{a_2}^{a_1} N_{aer}(a)\sigma_{ext}(a,\lambda,n)da$$

where α_{ext} is the total extinction cross section for particles of radius *a*, refractive index *n* at wavelength λ. Of course, both aerosol absorption and scattering contribute to α_{ext} . For the two processes the single cross sections are, respectively:

$$\sigma_{aer,scatt}(a,\lambda,n) = \pi a^2 Q_s(x,n)$$

$$\sigma_{aer,abs}(a,\lambda,n) = \pi a^2 Q_a(x,n)$$

and the scattering and absorption efficiencies (Q_s and Q_a) can be evaluated by numerical simulation.

Finally, regarding the Raman signal, the explicit formulation of lidar equation is:

$$P(\lambda, z) = P_L \frac{A_0}{z^2} \frac{c\tau_L}{2} \xi(\lambda) \frac{d\sigma_R(\pi)}{d\Omega} N_R(z) \xi(z) e^{-\int_0^z \alpha(\varsigma, \lambda_L) d\varsigma} e^{-\int_0^z \alpha(\varsigma, \lambda_R) d\varsigma} \quad (2.34).$$

In the above equation $N_R(z)$ represents numeric density of sounded species, which in the case of nitrogen corresponds to about 78% of total atmospheric density. Of course, for Raman extinction coefficient the molecular and aerosol contributions have to be introduced, as well as for the elastic one and the total extinction is the sum of both. Wavelength dependence of molecular part can be calculated from cross section for gases. On the contrary, wavelength dependence of the aerosol extinction coefficient is extremely complicated because it depends on the refractive index and shape as well. Afterwards, it is useful to introduce the following simplification[42]:

$$\frac{\alpha_{aer}(\lambda_R)}{\alpha_{aer}(\lambda_L)} = \left(\frac{\lambda_L}{\lambda_R} \right)^{\gamma}$$

where γ value varies depending on the size and composition of aerosols, as it is described in paragraph 3.1. Then, the problem of lidar equations inversion is to retrieve aerosol backscatter and extinction coefficients from (2.35) or (2.36).

2.5. Lidar data inversion

When the lidar signal is collected and backscatter and extinction profiles are known, then the problem of retrieving of microphysical properties of aerosol can be faced. In fact, the particles optical properties are related to their microphysical characteristics by two first kind Fredholm integral equations:

$$\beta_{aer}(\lambda, z) = \int_{a_{min}}^{a_{max}} K_\pi(a, \lambda; n) N(a, z) da = \int_{a_{min}}^{a_{max}} \pi r^2 Q_\pi(a, \lambda; n) N(a, z) da \quad (2.35)$$

$$\alpha_{aer}(\lambda, z) = \int_{a_{min}}^{a_{max}} K_{ext}(a, \lambda; n) N(a, z) da = \int_{a_{min}}^{a_{max}} \pi r^2 Q_{ext}(a, \lambda; n) N(a, z) da \quad (2.36)$$

where β(λ, z) denote the backscatter coefficient at wavelength λ and at height z, α(λ, z) is the respective extinction coefficient at the same height, *n* is the complex refraction index. K_i (i=π, ext) are the kernel efficiency for backscatter and extinction processes. The integration range a_{min} and a_{max} is extended on all possible values of the particles radius. N(*a*, z) is the dimensional distribution of particles, while $Q_\pi(a,\lambda;n)$ and $Q_{ext}(a, \lambda; n)$ are the efficiency of backscatter and extinction, respectively. In principle, those efficiencies can be derived from Mie theory; they are function of shape, dimension and chemical

particles composition. Finally, the quantity unknown in (2.37) and (2.38) is the numeric density profile N(a, z).

Several methods have been found to invert (2.35) and (2.36) both analytical and stochastic. An in-depth review of more used methods can be found elsewhere[43]. Here is enough to stress that analytic methods do not furnish (when existing) a simple solution of the problem, because it is an example of the so called ill-posed inverse problem[44]. Beside, lidar measurements are characterized by large errors and limited optical data (mainly backscatter coefficients) and this is a further difficulty to solve the problem. Actually, the solutions of (2.35) and (2.36) do not depend continuously by experimental data and they aren't unique. Anyway, to try to solve analytically the problem several assumptions are needed and regularization techniques are used to suppress instable solution, so that the problem can have only approximate solutions. Müller et al. proposed a method[45] to retrieve physical parameters of tropospheric aerosol starting from lidar profiles of backscattering at 6 wavelengths (355, 400, 532, 710, 800, and 1064 nm) and extinction at 2 wavelengths (355 and 532 nm), Regularization is performed by generalized cross-validation. Then, effective radius, volume, surface-area, and number concentrations, as well as the mean complex refractive can be determined. The method does not require any knowledge of the shape of the particle size distribution, while can use lidar data with relative error of the order of 20%. Another analytical method has been proposed by Böckmann[46] to retrieve the same quantity. This algorithm dose not requires a priori knowledge of the analytical shape of size distribution of particles nor an input guess distribution. It can be used to retrieve micro-physics aerosol parameters from lidar profiles of extinction at one wavelength and backscattering at three wavelengths, with relative errors up to 20%. A different point of view to invert (2.35) and (2.36) is based on probabilistic approach. Ligon et al.[47] [48] [49] proposed a stochastic method to invert the Fredholm equations, as long as the hypotheses of random distribution of particles in backscatter volume and single scattering process are assumed. An inverse Monte Carlo is used with both simulated and experimental data. Another stochastic method has been developed by Barnaba and Gobbi[50]. The method tries to obtain the functional relation that link backscatter coefficient with particles surface, volume and extinction coefficient. If uniquely determinate, such relation is a useful tool to estimate aerosol properties for single wavelength lidar. The Monte Carlo used method needs a large set of size distributions and composition.

3. Lidar Signal Analysis

The single scattering lidar equation described by (2.33) (or (2.35) for Raman signals) cannot be solved to derive vertical profiles of aerosol extinction α and backscatter β coefficients. To retrieve α and β profiles different methods have been proposed. If only elastically backscattered light at one wavelength is available, then aerosol backscatter profiles can be evaluated with some assumptions on aerosol extinction to backscatter coefficient ratio (lidar ratio, L) and for the value of the backscatter coefficient at a reference height. With Raman lidar no assumption are needed to measure the aerosol extinction profile with the exception of the knowledge of the backscattering value at a reference point. In addition, since the interaction between the atmospheric particles and polarized light is influenced by the particle shape, lidar depolarization measurements could improve the knowledge on shape and thermodynamic phase of such particles. Hence, calibration on measuring channel is needed to improve this kind of measure.

3.1. Extinction coefficient

Raman measurements that rely on pure molecular scattered signals at Raman shifted wavelengths from N_2 molecules can be used to get independent information on the aerosol extinction coefficient profile. Starting from Raman lidar equation, we follow the analytical method derived by Ansmann to retrieve aerosol extinction profiles[51]. From (2.35) the following equation is obtained:

$$\frac{P(z)z^2}{N_R(z)} = K \exp\left\{-\int_0^z \left[\alpha_{\lambda_L}^{aer}(\varsigma)+\alpha_{\lambda_L}^{mol}(\varsigma)\right]d\varsigma\right\}\exp\left\{-\int_0^z \left[\alpha_{\lambda_R}^{aer}(\varsigma)+\alpha_{\lambda_R}^{mol}(\varsigma)\right]d\varsigma\right\} \qquad (3.1)$$

where K contains all constant factors, overlap function have been considered 1, $N_R(z)=N_{N_2}(z)$ is the nitrogen density profile and it is evaluated through atmospheric standard model (it can be measured with radio sounding, as well), $\alpha_{\lambda_R}^{mol}(z)$ and $\alpha_{\lambda_{el}}^{mol}(z)$ are the molecular contributions to the aerosol extinction coefficient at N_2 Raman shifted wavelength and at the laser wavelength, respectively. Computing the logarithm of (3.1) and then the first derivative with respect to z, one can obtain:

$$\alpha_{\lambda_L}^{aer}(z)+\alpha_{\lambda_R}^{aer}(z) = -\frac{d}{dz}\left[\ln\left(\frac{P(z)z^2}{N_R(z)}\right)\right]-\alpha_{\lambda_L}^{mol}(z)-\alpha_{\lambda_R}^{aer}(z) \qquad (3.2).$$

The wavelength dependence of $\alpha_{\lambda_{el}}^{aer}(z)$ on the particle's microphysical properties and shape is taken into account by the coefficient γ. The equation describing such dependence is:

$$\frac{\alpha_{\lambda_R}^{aer}(z)}{\alpha_{\lambda_{el}}^{aer}(z)} = \left(\frac{\lambda_{el}}{\lambda_R}\right)^{\gamma(z)} \tag{3.3}$$

For our analysis γ has been set equal to 1 for sub micron aerosol particles or 0 for coarse particles, as ice crystals. Moreover, γ value can vary depending on the size and composition of aerosols. Some studies have been performed to evaluate the errors introduced in data analysis showing that this assumption does not contribute to significant errors[52,53]. From (3.2) and (3.3) the extinction coefficient can be obtained:

$$\alpha_{\lambda_{el}}^{aer}(z) = \frac{\frac{d}{dz}\left[\ln\left(\frac{N_{N_2}(z)}{P_{N_2}(z)\cdot z^2}\right)\right] - \alpha_{\lambda_{el}}^{mol}(z) - \alpha_{\lambda_R}^{mol}(z)}{1+\left(\frac{\lambda_R}{\lambda_{el}}\right)^{\gamma(z)}} \tag{3.4}$$

It should be underlined that for retrieving $\alpha_{\lambda_{el}}^{aer}(z)$ no critical input hypotheses have been done, so the uncertainty in the solution for aerosol extinction coefficient is almost completely due to the signal uncertainty.

3.2. Backscatter coefficient

In order to retrieve the particles backscatter coefficient profile two methods have been used depending on measurements lighting, i.e. for night-time or day-time conditions. In the former case, the Raman and elastic signals are needed to apply the so called Raman method[54]. From equations (2.33) and (2.35) molecular and particulate contribution can be made clear by writing:

$$P_{\lambda_L}(z) = \frac{K_{\lambda_L}}{z^2}\left[\beta_{\lambda_L}^{aer}(z)+\beta_{\lambda_L}^{mol}(z)\right]\exp\left\{-2\int_0^z\left[\alpha_{\lambda_L}^{aer}(\varsigma)+\alpha_{\lambda_L}^{mol}(\varsigma)\right]d\varsigma\right\} \tag{3.5}$$

$$P_{\lambda_R} = \frac{k_{\lambda_R}}{z^2}N_{N_2}(z_0)\frac{d\sigma_{\lambda_R}(\pi)}{d\Omega}\exp\left\{-\int_0^z\left[\alpha_{\lambda_R}^{aer}(\varsigma)+\alpha_{\lambda_R}^{mol}(\varsigma)\right]d\varsigma\right\}\exp\left\{-\int_0^z\left[\alpha_{\lambda_L}^{aer}(\varsigma)+\alpha_{\lambda_L}^{mol}(\varsigma)\right]d\varsigma\right\} \tag{3.6}$$

where λ_L is laser wavelength, λ_R is the Raman scattering response wavelength from the nitrogen molecule and k_{λ_i} (i=L, R) contain all the efficiency coefficients for the involved wavelengths. By mean of equations (3.5) and (3.6), the ratio:

$$\frac{P_{\lambda_L}(z)P_{\lambda_R}(z_0)}{P_{\lambda_L}(z_0)P_{\lambda_R}(z)} \tag{3.7}$$

can be evaluated. In (3.7) z_0 is a reference fixed height where the backscattering coefficient can be assumed known. Substituting (3.5) and (3.6) in the (3.7), the following relation can be obtained:

$$\beta_{\lambda_L}^{aer}(z)=\left[\beta_{\lambda_L}^{aer}(z_0)+\beta_{\lambda_L}^{mol}(z_0)\right]\frac{N_{N_2}(z)P_{\lambda_L}(z)P_{\lambda_R}(z_0)}{N_{N_2}(z_0)P_{\lambda_L}(z_0)P_{\lambda_R}(z)}\frac{e^{-\int_0^z\left[\alpha_{\lambda_R}^{aer}(\varsigma)+\alpha_{\lambda_R}^{mol}(\varsigma)\right]d\varsigma}}{e^{-\int_0^z\left[\alpha_{\lambda_L}^{aer}(\varsigma)+\alpha_{\lambda_L}^{mol}(\varsigma)\right]d\varsigma}}-\beta_{\lambda_L}^{mol}(z) \tag{3.8}.$$

In principle, as reference height can be chosen every z_0 where $\beta_{\lambda_{el}}^{aer}(z_0)$ is known, but in practice the height z_0 is chosen so that $\beta_{\lambda_{el}}^{aer}(z_0)<<\beta_{\lambda_{el}}^{mol}(z_0)$: this condition can take place in the free troposphere in absence of aerosol layers or clouds.

Using the relation (3.3) we obtain:

$$\beta_{\lambda_L}^{aer}(z)=\left[\beta_{\lambda_L}^{aer}(z_0)+\beta_{\lambda_L}^{mol}(z_0)\right]\frac{N_{N_2}(z)P_{\lambda_L}(z)P_{\lambda_R}(z_0)}{N_{N_2}(z_0)P_{\lambda_L}(z_0)P_{\lambda_R}(z)}\frac{e^{-\int_0^z\left[\left(\frac{\lambda_L}{\lambda_R}\right)^{\gamma}\alpha_{\lambda_L}^{aer}(\varsigma)+\alpha_{\lambda_R}^{mol}(\varsigma)\right]d\varsigma}}{e^{-\int_0^z\left[\alpha_{\lambda_L}^{aer}(\varsigma)+\alpha_{\lambda_L}^{mol}(\varsigma)\right]d\varsigma}}-\beta_{\lambda_L}^{mol}(z) \tag{3.9}$$

In this way, by using the value of the extinction coefficient determined from the Raman signal (3.4), the backscattering coefficient can be evaluated without ancillary hypothesis. The problem in using the Raman method to retrieve the particle backscattering is again linked to the low efficiency of the Raman process that entails a low signal to noise ratio for anelastic signal, so that the sounded range is limited to the first 3÷4 Km of the troposphere during day-time measurements.

Due to the above reported problem with the Raman efficiency, for day-time measurements, in general only the elastic signal can be used. Several methods have been proposed to resolved the ill-posed problem of the elastic lidar equation and to obtain quantitative profiles of extinction and/or backscattering coefficients from the single elastic lidar signal[55,56,57]. Here after the aerosol backscatter coefficient profiles is derived according the so-called Klett-Fernald algorithm[58,59]. To derive the algorithm, a function S(z) defined as the logarithm of the range corrected signal has to be introduced:

$$S(z)=\left[P_{\lambda_{el}}(z)z^2\right].$$

To make the lidar equation (2.35) independent from the parameters of the receiver, a reference height z_0 is chosen so that:

$$S(z)-S(z_0)=\ln\frac{\beta(z)}{\beta(z_0)}-2\int_{z_0}^{z}\alpha(\varsigma)d\varsigma \qquad (3.10).$$

By putting $\beta(z)=\beta$, $\beta(z_0)=\beta_0$ and deriving the previous relation with respect to z, the following differential equation is obtained:

$$\frac{dS(z)}{dz}=\frac{1}{\beta(z)}\frac{d\beta(z)}{dz}-2\alpha(z) \qquad (3.11).$$

To solve (3.11), the ratio between extinction and backscatter coefficients must be known. So, considering the backscatter coefficient as sum of aerosol and molecular contribution, the lidar ratio is defined as:

$$L(z)\equiv\frac{\alpha^{aer}(z)}{\beta^{aer}(z)} \qquad (3.12),$$

and the extinction can be written as:

$$\alpha(z)=L(z)\beta_{aer}(z)+\frac{\beta_{mol}(z)}{B_R(z)},\qquad B_R=0.119 \qquad (3.13).$$

From (3.11) and (3.13):

$$\frac{dS(z)}{dz}=\frac{1}{\beta(z)}\frac{d\beta(z)}{dz}-2\left[L(z)\beta_{aer}(z)+B_R{}^{-1}\beta_{mol}(z)\right]=\frac{1}{\beta(z)}\frac{d\beta(z)}{dz}-2L(z)\beta(z)+2\left[L(z)-B_R{}^{-1}\right]\beta_{mol}(z).$$

The new variable S'(z) is defined so that:

$$S'(z)-S_0'(z)=S(z)-S_0(z)+\frac{2}{B_R}\int_{z_0}^{z}\beta_{mol}(r)dr-2\int_{z_0}^{z}L(r)\beta_{mol}(r)dr$$

The previous equation can be differentiated with respect to z to give after some step:

$$\frac{d\beta(z)}{dz} - \beta(z)\frac{dS'(z)}{dz} = 2\beta^2(z)L(z) \qquad (3.14).$$

If a new variable is defined as $x = \beta^{-1}$, the equation (3.14) becomes a Bernoulli/Riccati equation:

$$-\frac{1}{x^2(z)}\frac{dx(z)}{dz} = \frac{dS'(z)}{dz}\frac{1}{x(z)} + \frac{2L(z)}{x^2(z)}$$

and the solution can be found as :

$$x(z) = \frac{\int_{z_0}^{z}\left(-2L(\varsigma)\exp\int_{z_0}^{z}\frac{dS'(\varsigma')}{d\varsigma'}d\varsigma'\right)d\varsigma + C}{\exp\left(\int_{z_0}^{z}\frac{dS'(\varsigma')}{d\varsigma'}d\varsigma'\right)}$$

and remembering that $x = \beta^{-1}$:

$$\beta(z) = \frac{\exp(S'-S_0')}{\beta_0^{-1} + 2\int_{z_0}^{z} L\exp\left(S'-S_0'\right)d\varsigma'} \qquad (3.15).$$

where, β_0 is the value of backscatter coefficient at the reference height z_0. Again β_0 can be estimated in an atmospheric range aerosol free.

Of course the main problem in applying the Fernald-Klett method is the assumption of extinction-to-backscatter ratio (L) as an input parameter. Actually, lidar ratio links two quantities (α and β) both dependent from particles refraction index, numerical and dimensional distribution of aerosols and from incoming wavelength. Afterwards, its profile cannot be estimated easily. Several authors reported values of the extinction to backscatter ratio as a function of the aerosol kind. L can vary from ~100sr (for urban aerosol) to ~10sr (for ice crystal in cirrus clouds)[60]. Some kind of aerosol can vary their dimensional distribution and refractive index with relative humidity as well (hygroscopic aerosol). A numerical analysis of L has been reported by Ackermann[61] for different kind of tropospheric aerosol, with particular attention to the dependence of the extinction-to-backscatter ratio on the relative humidity. Experimental measurements of the lidar ratios for different and climatically relevant aerosol types were summarized by Muller that reported for the first time a lidar ratio statistic solely based on direct measurements of that quantity[62].

3.3. Depolarization ratio

Measurements of the linear depolarization ratio can provide information about the shape and/or thermodynamic phase of suspended aerosol, and often require a low accuracy of the absolute values. Nevertheless, to carry out more detailed measures, it is necessary to carefully calibrate the system, thus making the lidar a perfect tool for atmospheric particle monitoring.

Several authors had already treated on depolarization measurements [see for instance, Sassen, 2005[63]] and hereafter a brief discussion on it will be developed. For the determination of the depolarization ratio, the backscattering radiation from sky is split in two receiver channels that acquire the parallel- and cross-polarized component of radiation with respect to the plane of the linear polarized output of the laser beam. Those components are typically separated in the receiver by means of polarizing beam-splitter. For sake of completeness, the lidar equation for depolarization system can be written as follow:

$$P_{P,S}(z) = K_{P,S}\,\frac{\beta_{P,S}(z)}{z^2}\,e^{-\int_0^z \alpha(\varsigma)\,d\varsigma}$$

where $P_{P,S}$ and $\beta_{P,S}$ are the backscattered power and total (molecular and particle) backscatter coefficient parallel and perpendicular, respectively, with respect to the polarization plane of the laser output. $K_{P,S}$ are the corresponding system constants including the laser emitted power and the telescope aperture. In the former equation, diattenuation of all optics before the splitting is assumed negligible, while the full overlap constant is assumed starting from ground.

The linear volume depolarization ratio, δ_V is defined as the calibrated power ratio between the perpendicular and parallel detected light component. Now, a very general expression of measured backscatter –P and –S components, which takes into account the polarization degree of the laser source (α) and cross talking of two channels ($B^{||}$ and $B^{\perp}$) was reported by Biele et al.[64] as:

$$\beta_P^m(z) = \frac{\beta_{T(z)}}{2}\left[1 + \frac{1-\delta_V(z)}{1+\delta_V(z)}\right](1-\alpha)\left(1-B^{||}\right)$$

$$\beta_S^m(z) = \frac{\beta_{T(z)}}{2}\left[1 - \frac{1-\delta_V(z)}{1+\delta_V(z)}\right](1-\alpha)\left(1-B^{\perp}\right)$$

where $\beta_T = \beta_P + \beta_S$. For our system, the contribution of not perfect polarization of the laser beam is the dominant effect, hence we can consider $(1- B^{||}) \approx (1- B^{\perp}) \approx 1$. The polarization degree of the laser

source α can be expressed in terms of the ratio between the components of the laser line $k = I_S/I_P$ (correction factor), we obtain $\alpha = 2k/(1+k)$ and the linear volume depolarization can be written as:

$$\delta_V(z) = \frac{\beta_S(z)}{\beta_P(z)} = \left[H\frac{S(z)}{P(z)} - k \right]\left[1 - kH\frac{S(z)}{P(z)} \right]^{-1} \tag{3.16}$$

where H (gain ratio) is the calibration constant, which takes into account the different efficiencies of the detection channels for power measured by the parallel, P(z), and perpendicular, S(z), polarization channels, and k takes into account the linear polarization degree of laser beam and the angular misalignment of the receiving optics.

The linear aerosol depolarization ratio δ_{aer} can be calculated then by introducing the scattering ratio $R=(\beta_{aer}+\beta_{mol})/\beta_{mol}$:

$$\delta_{aer}(z) = \frac{[1+\delta_{mol}(z)]\delta_V(z)R(z) - [1+\delta_V(z)]\delta_{mol}(z)}{[1+\delta_{mol}(z)]R(z) - [1+\delta_V(z)]} \tag{3.17}$$

where δ_{mol} is the molecular linear depolarization. This last parameter strictly depends on the specific lidar receiver since it is connected to the interferential filter bandwidth: actually, δ_{mol} varies by nearly a factor of 4 depending on whether the rotational Raman bands are considered in the detected signals or not[65].

3.4. Errors estimation

Of course, to have a realistic estimation of errors in atmospheric optical parameters profiling with lidar, many errors sources have to be considered: statistical error on signal, uncertainty on assumed atmospheric model, atmospheric instability, electronic noises, and uncertainty on overlap function. For backscatter coefficient (both Raman and Klett method) error on choice of the reference value is another source that must be taking into account. Because of different distributions of such error types it is quite difficult to apply analytical method to evaluating optical parameters final errors. So, a Monte Carlo method has been used because all error sources with different distributions can be included in this method.

Briefly, the evaluation of analogic signal errors is made through the evaluation of standard deviation on recorded 30 signal profiles (of 1 minute time length). Actually, this operation takes into account possible atmospheric fluctuations; for instance, significant variations can be present on the top of planetary boundary layer during measurement record because of high turbulence. To suppress

background, the average over high altitudes is calculated and then subtracted to the signal for each signal.

For the error coming from the photon counting system, a normal distribution is assumed because of large number of collected photons for each acquisition channel on multi-scaler. Defining $p_{k,j}(z_i)$ as the single shot signal at the height z_i, where k are the shot numbers (k=1,…, 1200 shot/min for Nd:YAG liar operating at a repetition frequency of 20 Hz), j are the minute length record number (j=1,…, 30 min, typically), and i are the numbers of channels (i=1,…, 2000 for a d-well time of $100 \cdot 10^{-9}$ sec). Then the total accumulated signal is:

$$P_{tot}(z_i) = \sum_j P_j(z_i) = \sum_j \sum_k p_{k,j}(z_i) \tag{3.19}$$

with a standard deviation of:

$$\sigma_1 = \sqrt{\sum_j \left[P_j - B_j - \frac{\sum_j (P_j - B_j)}{30} \right]^2} \tag{3.20}$$

where the background B_j is evaluated in the far field range (z_{n1}; z_{n2}) for each of measured lidar profiles. In the same range (where the lidar signal is negligible), the standard deviation is

$$\sigma_2 = \sqrt{\sum_i \left[P_i - \frac{\sum_i P_i}{n2 - n1} \right]^2} \tag{3.21}$$

It includes the statistic and the electrical noise. The former error is done by:

$$\sigma_3 = \sqrt{\frac{\sum_{i=n1}^{n2} P_i}{n2 - n1}} \tag{3.22}$$

On the other hand, the electrical noise and other instrumental errors are evaluated from high altitude signals (above 20km) where the signal is only due to background radiation: any deviation from the expected background registered signal is considered as instrumental error. Then, the instrumental error can be evaluated from the difference between (3.21) and (3.22):

$$\sigma_4 = \sqrt{\sigma_2^{\,2} - \sigma_3^{\,2}} \tag{3.23}.$$

Finally, the error for the accumulate signal P_i is:

$$\sigma_i = \sqrt{\sigma_1^2 + \sigma_4{}^2} \qquad (3.24).$$

The above treatment regards the evaluation on signal errors. To compute the errors on aerosol optical parameter the error propagation should be applied. For the extinction coefficient it is quite difficult to apply such procedure because of differentiation of the logarithm of the inverse of the Raman signal in (3.4). Afterwards, Monte Carlo procedure has been used in order to evaluate the extinction error. Besides, the experimental error on overlap function is taken into account. All treated error sources are combined together in the Monte Carlo error procedure as follow:

- A number of simulated N_2 Raman signals are generated extracting each data point from the statistical distribution of the experimental data, which take into account the signal statistical error, instrumental error and overlap function error. Usually, the number of 50 signals is enough to get stable results for extinction errors.
- From each of these lidar profiles, extinction profiles are determined by applying the above described algorithm. When applying these algorithms the uncertainty on the temperature is introduced and the same is done for the uncertainty in the choice of the reference point.

The error on extinction coefficient at the height z_i is evaluated as the standard deviation of simulated extinction coefficient. The same procedure is used to evaluate the error on backscattering through the Klett method.

Concerning the backscattering coefficient evaluated with Raman method (3.9):

$$\sigma_i = \sqrt{\left(\frac{\sigma_{i,P_{\lambda_{el}}}}{P_{i,\lambda_{el}}}\right)^2 + \left(\frac{\sigma_{i,P_{\lambda_{Ram}}}}{P_{i,\lambda_{Ram}}}\right)^2}\left(\beta_i^{aer} + \beta_i^{mol}\right) \qquad (3.25)$$

is the error evaluated analytically through the error propagation formula.

4. Lidar Systems

Lidar is an active remote sensing tool useful to study different aspects of Earth atmosphere. In particular, Raman lidars have evolved into powerful tool for atmospheric research. For instance, it can be used to study cirrus clouds[66], stratospheric polar clouds[67], stratospheric ozone[68], and tropospheric aerosol[69]. This makes lidars particularly suitable for meteorological and climatological studies. Two of the main features of lidar are the high spatial and temporal resolution that allows exploiting laser-radar for planetary boundary layer measurements[70]. Moreover, through a mobile scanning system it is possible to build a 3-D map of aerosol and/or pollutants distribution.

To profile the atmospheric aerosols, traditional lidars make use of flash-lamp lasers, with a typical repetition rate of 10Hz-30Hz and energies pulses of a few hundred mJ. Such lasers needs for liquid cooling, therefore are unwieldy and heavy. The high pulse energy usually leads to a saturation of the detectors and to compensate for this, one is forced to attenuate the return signal, thereby worsening the sounded range. Moreover, the complexity of this type of sources limits their use in the laboratory. To improve the survey capability of the lidar to evaluate effectively the microphysical characteristics and optical properties of the aerosols, a new scheme of lidar system has been developed. It is based on a novel concept that involves the use a high repetition rate laser source at low pulse energy. The average power sent into the atmosphere is still comparable to the one sent with the traditional systems, but the low energy per pulse prevents the saturation of phototubes and therefore allows expanding the overall dynamics of the system. Furthermore, this type of laser is air cooled thus allowing to obtain high performance in scanning systems.

4.1. Multi-wavelength Aerosol LIdar Apparatus - MALIA

MALIA is a lidar system operating at Physics Department of University of Napoli. It is part of the European project EARLINET[71] (Lidar observation for European Aerosol Research Lidar Network) and is based on an Nd:YAG laser source (QUANTEL mod. Brilliant-B) that works at fundamental wavelength of 1064 nm, and it is frequency doubled and tripled at 532 nm and 355 nm, respectively. The repetition rate is 20 Hz, while maximum pulse energies for each wavelengths are 0.65 J, 0.15 J and 0.1 J for the fundamental, 2nd and 3rd harmonic, respectively. Beam divergence is 0.5 mrad and pulse

duration is 5 nsec. The receiving system is based on the same 30 cm Newtonian telescope with a focal length of 120 cm. The sketch of the system is showed in figure 1.

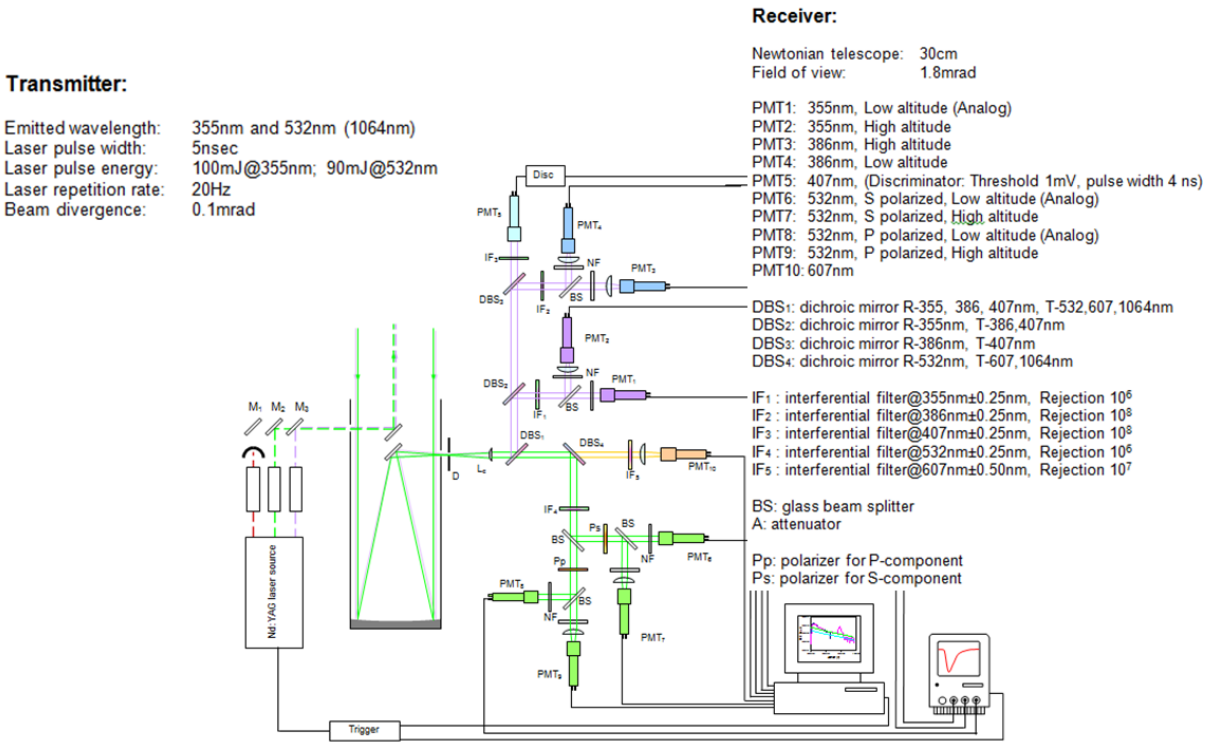

Fig.4. 1. Experimental set-up of MALIA lidar system. The diaphragm D selects the telescope field of view at 1.33 mrad. A fused silica plan-convex lens (Lc) is used to tally the collected backscattered light. The beam is separated from a system of dichroic beam splitters (DBSi). The UV-blue backscatter light is reflected from DBS1, while VIS light is transmitted toward DBS4. Afterwards DBS2 separates elastic 355nm backscatter radiation from Raman echoes from N2 and H2O molecule, which are the separated from DBS3. Finally the DBS4 splits the elastic 532nm component from the Raman echo at 607nm. Grey filters are used to prevent photocathode saturation after the 0.5nm bandwidth interferential filters. Polarization selection is performed through the two linear polarizer Pp and Ps.

Table 4. 1 Parameters of the MALIA Laser Transmitter System

MALIA laser transmitter

Emitted wavelength, nm	1064	532	355
Repetition rate (max), Hz		20	
Energy (typ), mJ	300	100	100
Pulse width, ns	≈6	≈6	≈7
Laser divergence, mrad		0.5 (fw at $1/e^2$ of energy)	
Beam expander		Galileian telescope	
Final divergence, mrad		<0.1	
Pointing stability, mrad		≈0.01	
Polarization orientation	Vertical	Horizontal	Vertical
Polarization purity	//	Better than 99% (linear)	//

In this configuration the laser beams can be fired in the atmosphere both in monostatic configuration or bi-static one. In the former case the telescope optical axis is coincident with the laser

beam axis, in the latter case laser beam can be fired so that the two axes are parallel (removing mirrors M_2, M_3, while at the moment the IR beam is not yet used). The choice between the two configurations is done referring to the atmospheric layer height to be studied and considering the overlap between laser beam and the telescope field of view. So, for upper troposphere and stratosphere, the bi-static configuration should be preferred, while the monostatic one should be used for PBL and lower atmosphere studies.

Table 4. 2 Parameters of the MALIA Laser Receiving System

Channel name	Detected wavelength(nm), polarization, range	Sensor (photmultiplier model)	Measurement mode	Raw spatial resolution (m)
PMT_1	355, high	Hamamatsu H6180	Photon Counting	15
PMT_2	355, low	ElectronTubes 9202QB	Analog	3
PMT_3	386.7, high	Hamamatsu H6180	Photon Counting	15
PMT_4	386.7, low	ElectronTubes PC25P	Photon Counting	15
PMT_5	407	Hamamatsu R1828	Photon Counting	15
PMT_6	532, S, high	Hamamatsu H6180	Photon Counting	15
PMT_7	532, S, low	ElectronTubes 9202QB	Analog	3
PMT_8	532, P, high	Hamamatsu H6180	Photon Counting	15
PMT_9	532, P, low	ElectronTubes 9202QB	Analog	3
PMT_{10}	607	Hamamatsu 7402-20	Photon Counting	15

Although fast photomultipliers are used for detecting light from the atmosphere, elastic and nitrogen Raman at 387nm signals need to be split in low/high range by a quartz plate to extend the system dynamic. For low altitudes the receiving photomultiplier has a stronger attenuation in order to warrant a linear response while for high altitudes a smaller attenuation can be used. Non-linearity due to the dead time phenomenon can be corrected through the formula $N=n/(1-nT)$, where N is the expected count rate, n is the measured count rate, and T is the detector dead time. The main aim of this procedure is to warrant a linear working range for both near and far field channels, so that the two acquired signals can be normalized over an extended range (2÷3Km at least). In these conditions merging of the two signals can be made by software.

Since the MALIA system is used mainly for aerosol measurements in the troposphere, an accurate evaluation of overlap function $\xi(\lambda, z)$ is needed. In monostatic configuration, the ξ function corrects the underestimated signal due to the shadow of secondary mirror of the telescope, which stops the atmospheric backscatter photons at lower heights. Besides, in bi-static configuration the underestimation of signal derives from no-overlapping of the laser beam and telescope field of view under some height, which can vary from few hundreds meter to some kilometer depending on the distance between telescope optical and laser beam axes. This evaluation has been performed several times in the years and results are used to correct the lidar signal at low heights. Afterwards, deep

knowledge of this function is really important, because the majority of aerosol load is in the lower atmospheric layers. Several methods have been proposed to know the overlap function profile. In principle, an analytical approach[72] can be applied for the evaluation of overlap function, but it requires heavy approximations on the system: laser beam is supposed to be Gaussian and its divergence should be small compared with the telescope field of view; the received beam should be perpendicular to all receiving optics; all optics should be aberration free; the PMT sensitive surface should be uniform. Often, all these hypotheses aren't verified in a real lidar system. The profile for real cases can be retrieved through an experimental approach based on a Wandinger work[73] that take advantage of the (realistic) hypothesis that both elastic and Raman measurements have the same overlap profile. With the knowledge of the overlap correction it is possible to retrieve backscattering profile starting from 200 m, while the first useful point for extinction measurements is situated at 400 m.

The MALIA system has the capability to acquire water vapour mixing ratio profiles. The water vapour signal is acquired at 407nm, which is the Raman shifted signal from H_2O molecules excited by 355nm laser radiation. General lidar equation for Raman scattering is:

$$P(\lambda_R, z) = P_0 \frac{c\tau}{2} \frac{A}{z^2} \frac{d\sigma_R(\pi)}{d\Omega} N_R(z) \xi(z,\lambda) e^{-\int_z^0 \alpha(\lambda_R,\zeta)d\zeta} e^{-2\int_0^z \alpha(\lambda_0,\zeta)d\zeta} \quad (4.1)$$

where:

- $P(\lambda_R, z)$ is measured backscatter power at wavelength λ_R;
- $P_0 = P(\lambda_0)$ is the laser emitted power;
- $c\tau/2$ is the half laser pulse time width, which is the maximum theoretical resolution of system;
- A is the primary mirror surface;
- $\frac{d\sigma_R(\pi)}{d\Omega}$ is the molecular Raman cross section;
- $N_R(z)$ is the scattering target density profile (number density);
- $\xi(\lambda,z)$ is the overlap function (assuming 1 the collecting efficiency of the system);
- $\int_0^z \alpha(\lambda_i,\zeta)d\zeta$ is the atmospheric optical dept (i=0, R);
- $\alpha(\lambda_i, z)$ is the extinction coefficient at wavelength λ_i (i=0, R).

Water vapour mixing ratio is then obtained from the ratio of its number density to the number density of the ambient air. Since Nitrogen molecules density profile have a well-known behavior, the Raman signal from N_2 can be used to determine the density of the ambient air since it represents a constant, well-known portion of dry air in the atmosphere. This ratio is known as the water vapour

mixing ratio and it is given in units of grams per kilogram. The eq. (4.1) describes the collected Raman signals both for nitrogen and water vapour, they are proportional to the numeric density of gasses. Through simultaneous measurements of backscattered signal from H_2O and N_2 molecules and re-writing (4.1) for each species, the ratio between the two signals can be written as[74]:

$$\chi_{H_2O} = K \frac{P\left(\lambda_{H_2O}, z\right)}{P\left(\lambda_{N_2}, z\right)} \frac{e^{-\int_0^z \alpha\left(\lambda_{H_2O}, \varsigma\right) d\varsigma}}{e^{-\int_0^z \alpha\left(\lambda_{N_2}, \varsigma\right) d\varsigma}} \qquad (4.2).$$

Many of the unknown factors in the lidar equation are cancelled out by taking the ratio of the two return signals. However, molecular scattering and ozone absorption (at ultraviolet wavelengths) are wavelength dependent parameters that do not cancel out in this ratio. The dependence can be illustrated by taking the ratio of the signals in the lidar equation. Knowing temperature profile, from (4.2) is possible retrieve the relative humidity profile. Calibration constant K takes into account differences between both the cross section of process for the two different species, and quantum efficiency of photocathode at different wavelengths. Furthermore, it takes into account the relative abundance of different gasses. For the determination of such a constant a reliable method is the comparison between lidar and radio-sonde measurements. Anyway, radio-sounding from Naples lidar site are not allowed because the site is very close to the aircrafts landing route for Naples International airport, and they fly over lidar station at less than 1 km of altitude. Afterwards, for calibration sounding from Rome - Pratica di Mare airport (available on WEB[75]) have been used, which is located 170 km far from Naples. On web site two daily soundings are available, at 00:00UT and at 12:00UT. Constant calibration K has been determined by fitting the measured mixing ratio with the water vapour data from radio-sonde balloons above planetary boundary layer. This choice has been done because it seems realistic that outside the PBL the water vapour concentration is near independent on local conditions like orography, local water vapour sources and so on. The presently utilized value for K is 0.140 $\pm$ 0.025, it has been calculate as the average of five measurements performed in different days.

According the Mie theory, the light interaction with an ideal homogeneous sphere does not change the polarization state of the incident radiation. In real cases, most of the atmospheric particles have different, irregular shapes and this can introduce a degree of depolarization on backscatter light. Therefore, lidar depolarization measurements can allow inferring information on shape and thermodynamic state of particles. The depolarization technique makes use of a linearly polarized laser transmitter and two-channel capable of measuring the components of the return signal polarized parallel and perpendicular with respect to the transmitted laser beam.

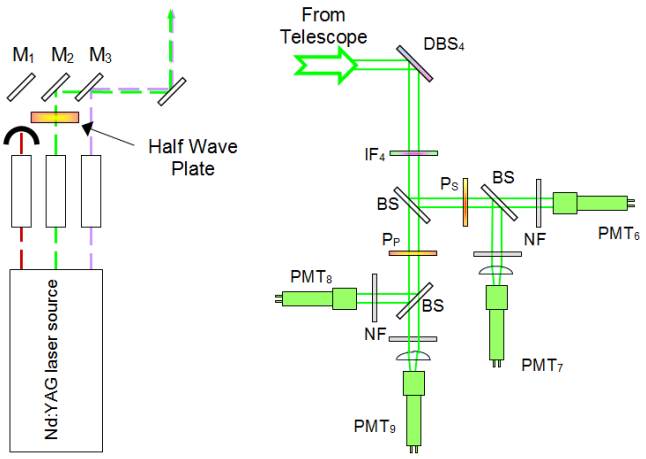

Fig.4. 2 In the picture above the polarization measurements set-up is shown. The half wave plate is used to turn the polarization plane of ±45°.

A polarizing beam splitter is used to split the perpendicular-polarized component of the backscatter signal (from now on, P-component) and the parallel component to the other (S-component)[76]. The calibrated power ratio between the light components detected in P and S channels is known as the linear volume depolarization ratio, δ_V.

In figure 4.2 the configuration for depolarization measurement is shown. The light coming from telescope is split from dichroic beam splitter DBS4 that separate the green component from Raman echoes at 607nm (see figure 4.1). An interferential filter at 532nm (FWHM 0.5nm) is placed before a quartz beam splitter which separates the incoming radiation into two beams. Downstream of the BS, two highly selective polarizers (named P_P and P_S) are positioned to define the component parallel (P) and orthogonal (S) of the acquired lidar signal with respect to the plane defined by the polarization of the outgoing laser beam. In addition, each polarization channel is split into high and low range to improve the dynamic range of the acquisition system.

Several methods[77,78,79] have been proposed to calibrate the gain ratio between the two depolarization channels, among them the most utilized are: the molecular technique[80,81,82], the orthogonal calibration method and the so called ±45° technique[83,84,85]. To obtain the calibration of t polarization channels, a rotating half wave plate has been positioned on outgoing beam, hence rotating it on ±22.5° a rotation of ±45° of the polarization plane of the laser beam is achieved. Starting from the equation (4.1) two set of measurements are needed:

$$P_{P,+45°}(z) = K_{P,+45°}\frac{\beta_{P,+45°}(z)}{z^2}e^{-\int_0^z \alpha(\varsigma)d\varsigma} \qquad P_{P,-45°}(z) = K_{P,-45°}\frac{\beta_{P,-45°}(z)}{z^2}e^{-\int_0^z \alpha(\varsigma)d\varsigma}$$

and

$$P_{S,+45°}(z) = K_{S,+45°}\frac{\beta_{S,+45°}(z)}{z^2}e^{-\int_0^z \alpha(\varsigma)d\varsigma} \qquad P_{S,-45°}(z) = K_{S,-45°}\frac{\beta_{S,-45°}(z)}{z^2}e^{-\int_0^z \alpha(\varsigma)d\varsigma}$$

Since two signals are supposed to be equal (i.e., $P_{P,+45}=P_{S,+45}$ and $P_{P,-45}=P_{S,-45}$), the calibration constant (from now on called *gain ratio* H) is:

$$H = 0.5\left[\frac{P_{S,-45°}(z)}{P_{P,-45°}(z)} + \frac{P_{S,+45°}(z)}{P_{P,+45°}(z)}\right]$$

The figure 4.3 shows an example of depolarization calibration measurements performed on July 2010. As figure 4.3 (c) shows, the gain ratio is constant with the altitude, save in the first hundreds meters where the different overlap between the channels have big influence over the signals.

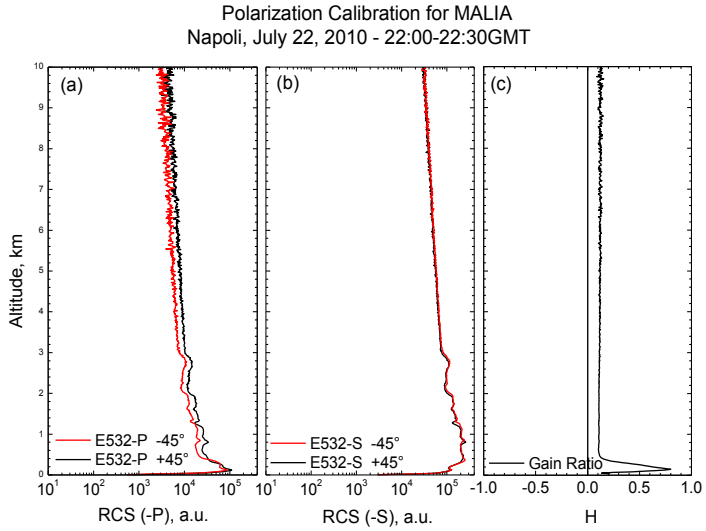

Fig. 4. 3 Figure shows an example of calibration measurement. Figure (a) reports the range corrected signal of parallel component (with respect to the polarization plane of the laser beam) of the signal, figure (b) reports the range corrected signal of perpendicular component of the signal, and (c) is the measured gain ratio.

Meteorological parameters at ground level are acquired by means of temperature, pressure, relative humidity, speed and direction of the wind. Those data are needed because the lidar signal is strictly linked to physical atmospheric parameters affecting the collected signal by mean of backscatter and extinction coefficients. The knowledge of temporal behaviour of meteorological parameters is useful to understand the atmospheric dynamics at ground level as well.

4.2 Volcanic Ashes by Measuring Polarization (VAMP) experiment

The VAMP system is a portable lidar based on the evolution of a former compact prototype of lidar[86]. Such a prototype has been designed to characterize the particle distribution in urban areas by measuring the elastic aerosols backscattering coefficient at two wavelengths, so allowing to calculate the backscattered-related Angstrom coefficient.

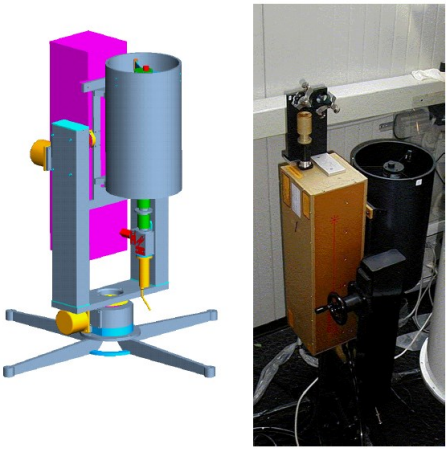

Fig.4. 4 (left) layout and (right) picture of the lidar prototype from which VAMP derives.

This lidar is based on a pulsed solid-state source (Nd:YAG laser). Fundamental harmonic is used for the pumping of nonlinear crystals which provide, alternately, outgoing laser radiation with wavelength equal to λ=532 nm (SHG) or λ=355 nm (THG). In both cases the energy distribution of the beam is Gaussian on planes perpendicular to the propagation direction. The frequency of Q-Switching is variable with a pitch of 100 Hz between 100 Hz and 5 KHz and with a pitch of 500Hz between 5 KHz and 10 KHz. It generally works to 1000 Hz. For depolarization measurement the system was used at 532 nm. At this wavelength, laser pulses are emitted with energy of 0.3 mJ, duration of 40 ns and a linear polarization better than 100:1. The beam divergence is reduced to less than 0.1 mrad FWHM by a five time beam expander. The lidar operates in biaxial configuration with distance between the laser beam and telescope axis of 27cm. The receiver is a Cassegrain telescope with a 20 cm aperture diameter, a focal length of 140 cm, and a field of view of 1 mrad, defined by a 1.4 mm field stop positioned of telescope focal plane. After the focus, an interferential filter (CWL 532 nm, FWHM 0.5 nm) is used for spectral selection. A thin film plate polarizing beamsplitter (extinction ratio better than 500:1) separates the components of the backscatter radiation, parallel (P) and cross-polarized (S) with respect to the polarization plane of the emitted laser beam. The cross-talk coefficients between the two polarization channels were measured resulting lower than 3% and 0.2% for the P and S channel, respectively. Two photon counting modules are used in channels detecting the two polarization sensitive components. The acquisition of lidar data has been made by two multi-channel scalers and signals were stored with a raw spatial resolution of 30 m. To increase the signal to noise ratio the final spatial resolution is reduced to 60 m for backscattering calculation. The whole lidar system is mounted on a motorized fork, allowing a scanning speed of 0.1 rad s^{-1}. The actual scanning speed is limited by the signal to noise ratio of the registered profile. During night-time measurements, single lidar profiles extend up to 20 km with a temporal integration of less than 20 s. In day-time conditions 1 min of time integration is required in order to have backscattering and aerosol linear depolarization ratio profiles extending up to 10 km.

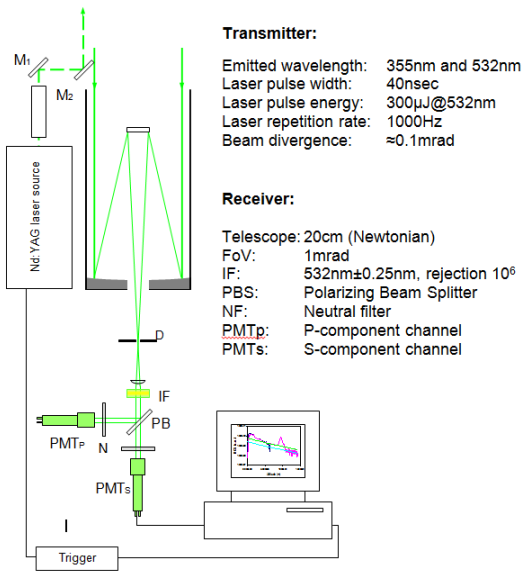

Fig.4. 5 Experimental set-up of VAMP lidar system. The diaphragm D selects the telescope field of view at 1 mrad. The beam is collimated by a fused silica plan-convex and that 0.5nm bandwidths interferential filter IF makes the spectral selection at 532 nm. The polarizing beam splitter PB than separate the component of polarized backscattered light. Grey filters are located just in front of the photocathode to prevent non linearity.

The accuracy of the system calibration is reflected in the quality of the depolarization lidar measurements. In order to determine the gain ratio H and the calibration constant k of the VAMP system, intercomparison measurements were performed between MALIA and VAMP in June-July 2010. The coefficients H and k for VAMP were determined by minimizing the quantity:

$$\sum_{z} \frac{\left(\delta_{V,M} - \delta_{V,V}\right)^2}{\sigma_M^2 + \sigma_V^2} \qquad (4.3)$$

where $\delta_{V,M}$ and $\delta_{V,V}$ represent the linear total depolarization obtained from MALIA and VAMP, respectively, and σ_M and σ_V are the corresponding errors. The error σ_M takes into account the errors on signals and on calibrations constants. The error σ_V is calculated from propagation of errors on S(z) and P(z) through $\delta_{V,M}$ and $\delta_{V,V}$, and assigning to H and k the values derived by a first minimization of the quantity (4.3), with σ_V =0. The sum is then calculated over the full range sounded by the two lidars. Figure x shows an example of intercomparison measurement that was carried out on June 9, 2010. The picture shows the –S component of the acquired signals for MALIA and VAMP as they are (figure 4.6a). After the minimization process the total signal is reconstructed as $P_{Tot} = P_P + HP_S$ (figure 4.6b). Finally, the linear volume depolarization profile can be retrieved after the calibration and the profiles of δ_V for MALIA and VAMP are reported in the figure 4.6.

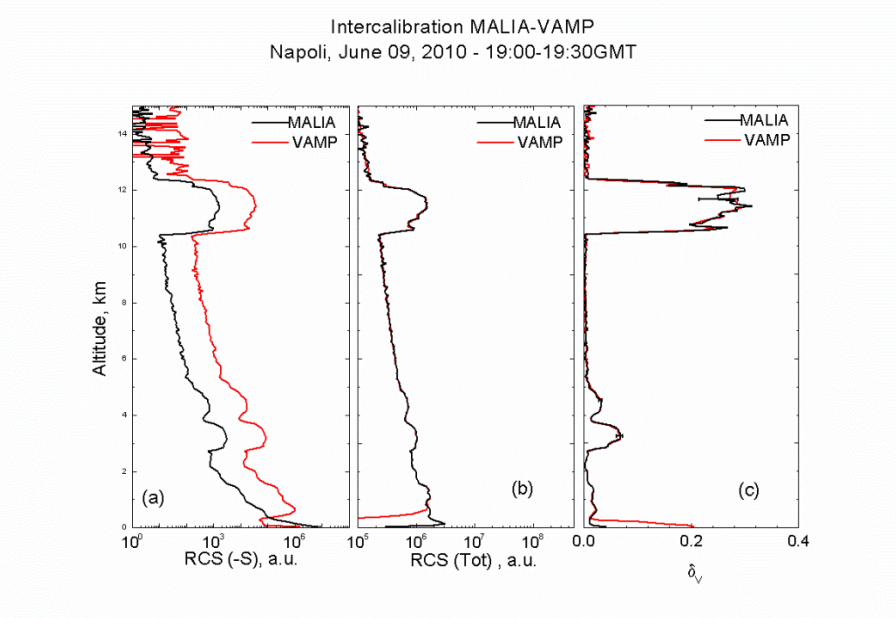

Fig.4. 6 Example of intercalibration measurement between MALIA and VAMP systems. Data were acquired pointing to the vertical direction with a spatial resolution of 60 m and an integration time of 1800 seconds, starting at 19:00 GMT. (a) Detected RCS –S signals, (b) total reconstructed RCS and (c) linear volume depolarization coefficient at 532 nm from VAMP and MALIA lidars.

To test the stability of the system, the intercalibration procedure was performed several times in day and night time conditions, with the presence of cirrus or Saharan dust layers. Mean values of 0.072±0.005 and 0.01±0.01 were obtained for H and k of the VAMP lidar, respectively; the errors on H and K take into account standard deviations and the systematic error due to the uncertainty on the MALIA system calibration constant, which is of the order of 2%, as determined from a long series of calibration procedures. The discrepancies below 1km are due to differences in the overlap functions of the two lidars. During these tests hasn't observed any optical misalignment. A further confirmation of the system stability came from the comparison with results of the molecular calibration procedure[87], systematically performed whenever possible.

4.3 Aerosol Multi-wavelength Polarization Lidar Experiment – AMPLE

The scientific purpose which led to the AMPLE project is based on the following considerations.

The natural aerosols are originated from dust storms, volcano eruptions, forest, and sea spray. Human activities, such as the burning of fossil fuels, industrial activities, and ground transport also generate aerosols. In high urbanized areas, often it happens that the atmospheric particulate matter concentration smaller than 2.5 μm (the so called $PM_{2.5}$) systematically exceeds the healthy limit values. Concerning the natural aerosols, they are mainly composed by mineral particles. The Sahara desert, for instance, is the major source on Earth of mineral dust. On the other hand, large amount of mineral atmospheric particles are also produced by the Gobi desert, in the border between Mongolia and

People's Republic of China. The city of Beijing is in the path of these desert sand outbreaks, so the air quality in this city is dramatically affected by natural dust. Furthermore, Beijing's air quality is also affected by anthropogenic factors like the increasing of car ownership, the industrial activities in the neighbouring cities and biomass burning. The air over Beijing is, hence, the result of a complex mixture of these natural and anthropogenic dusts. So, when natural dust and anthropic polluted aerosol are mixed together the result can be a thick haze mixture that appears like fog.

Another point that needs to be stressed is the detection and characterization of volcanic ash and the monitoring of their spatial distribution and temporal dynamics, being the ashes potentially dangerous for human health and for issues related to air traffic management. In fact, during a volcanic eruption, a large amount of solid particles and gas are emitted from the crater and injected directly into the atmosphere. Within this column several kinds of particles different for thermodynamic phases, shape and dimensions coexist. The volcanic ashes are a particular type of particles emitted from volcanoes being defined by the size, which must not exceed 2 mm in diameter (50 μm for thin ashes). These particles can travel also for thousands of kilometres when carried by the wind and can remain in suspension in the atmosphere for a quite large time. Generally speaking, volcanic ashes are not poisonous, but they can cause respiratory problems because of their inhalation, since they are composed mainly of silica and so can be very abrasive and cause several kinds of irritations. Moreover, a major role has the detection of volcanic ash in the aeronautical field. In fact, the ashes represent a danger to any aircraft that fly within a volcanic cloud, as both motors both other essential parts (control surfaces, windows …) can be easily damaged, even at concentrations absolutely undetectable by current radar sensors. The recent eruption of the Eyjafjallajökull in Iceland (in April 2010) had shown the vulnerability of the air control system from this point of view. Actually, for safety reasons, the air traffic control was forced to block all flights in most of northern Europe.

According to the above considerations, the need of a new advanced scanning lidar system raised to: a) the understanding of the formation, emission and diffusion of particulate from natural and anthropic sources; b) to characterize the chemical and physical properties of atmospheric aerosols, their spatial and temporal distribution, and the main transport mechanisms, c) to evaluate the relative contribution of natural and anthropogenic sources. The scanning capability of lidar device shall improve the possibility to monitor the aerosol volume distribution by 4-D (space and temporal dimension) mapping of the clouds. Therefore, the main goal of this PhD project is the design and implementation of a this new, versatile and portable scanning lidar system that will be used as sensor to carry out 4-D (space and time) imaging of the atmospheric aerosol distributions, their optical properties, and microphysical characterization in volcanic proximity and in the urban area of polluted city, as Beijing.

On the base of the experience acquired with MALIA and VAMP systems, a new prototype of lidar has been designed and developed at Physics Department of University of Napoli "Federico II". The AMPLE (Aerosol Multi-wavelength Polarization Lidar Experiment) system was designed starting from signals simulations. The main goal of this new system was to extend the dynamic range of the signal so that better, accurate measurements of aerosol optical properties can be provided in case of thick layers. Figure 4.6, in fact, shows that we found out that the dynamic of the signal could be improved (almost by two order of magnitude) by increasing the laser repetition rate, keeping constant the optical power.

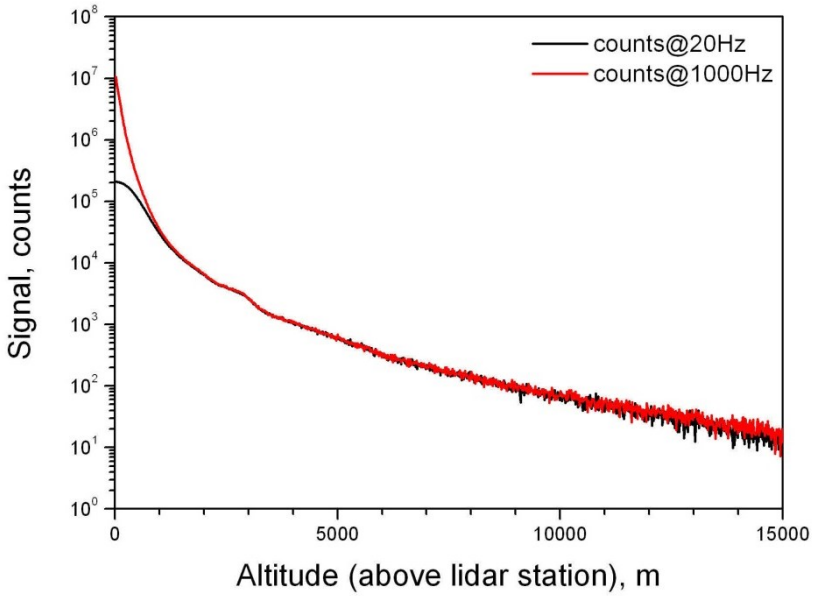

Fig.4. 7 Signal simulation for two different transmitter systems: black curve represents the signal corresponding to transmitted laser pulses of 0.1 J and repetition rate of 20 Hz, while the red curve represents the signal corresponding to transmitted laser pulses of 0.002 J and repetition rate of 1000 Hz. For both cases the dead time of the photomultiplier is considered to be 18 ns.

Starting from an actual measurement performed by MALIA, keeping constant the average emitted laser power and detector type, the simulation was performed considering the typical night time measurements condition, the dark noise of the detector and the photomultiplier module paralyzable dead time (18 ns, from Hamamatsu catalog). From results at low altitude (where the optical thickness is high) it is clear that the dynamics of the signal increases by almost 2 orders of magnitude using the high frequency laser.

Indeed, the keystone for the whole apparatus is the laser source, which is a doubled and tripled diode pumped Nd:YAG laser that has been especially designed for this device, with a repetition rate of 1KHz and 0.6W, 1.5W, 1.0W of mean optical power at 355, 532 and 1064nm, respectively, that allowed to detect both elastic and Raman lidar returns.

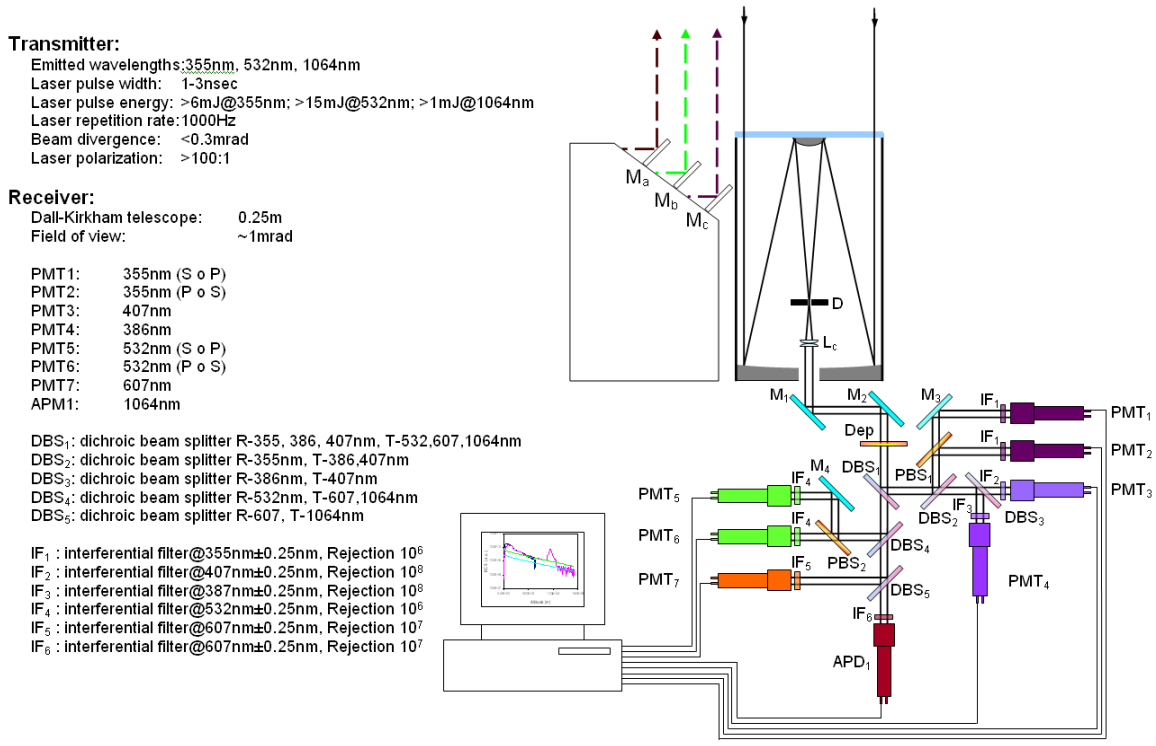

Fig.4. 8 Experimental set-up of AMPLE lidar system. The diaphragm D selects the telescope field of view at 1.0 mrad. A fused silica doublet (Lc) is used to tally the collected backscattered light. The two mirrors M_1 and M_2 need to align the receiver telescope with the polychromator system that uses the dichroic beam splitters (DBSi) to separate all the colour component of the backscattered signal. The UV-blue backscatter light is reflected from DBS1, while VIS light is transmitted toward DBS4. Afterwards DBS2 separates elastic 355nm backscatter radiation from Raman echoes from N2 and H_2O molecules, which are the separated from DBS3. The DBS4 splits the elastic 532nm component from the long wavelengths and, finally, the DBS5 separate the Raman echo at 607nm from 1064nm component. Grey filters are used to prevent photocathode saturation after the 0.5nm bandwidth interferential filters. Polarization selection is performed by means of the two linear polarizers PBS_1 at 355nm and PBS_2 at 532nm.

The AMPLE optical subsystems are mounted on an aluminum scanning system. The optical bench with the polychromator receiver is placed behind the telescope primary mirror and the photomultipliers are temperature-stabilized.

The AMPLE transmitter system is based on an OEM Nd:YAG laser source from Bright Solutions, namely the CC-WEDGE 11901 model. The laser is frequency doubled and tripled and its native repetition rate is 1 KHz. The transmitted laser beam is expanded tenfold with a Galilean type lens telescope so that the beam divergence in the atmosphere is less than 0.1 mrad. At the three wavelengths, the laser emits pulses having typical energy of 1mJ@1064nm, 1.5mJ@532nm, and 0.6mJ@355nm, with a pulse width of 1 ns. The three beams can be manually aligned with respect to the telescope optical axes through the steering mirror M_a, M_b, M_c (in the Figure 4.8), but in the next future the system can be equipped with micro-actuators for active alignment of the laser beam. The receiver telescope is in Dall-Kirkham configuration. The primary elliptic mirror has a diameter 250 mm, while the secondary mirror has a spherical shape so that the total focal length of the telescope is 1125

mm. The telescope is also shielded against dust by using a quarts window that actually acts as holder for the secondary mirror. In order to shorter the length of the telescope tube, the telescope focus is placed near the vertex of primary mirror and a field stop determines the field of view (FOV) of the system, which is fixed at 1 mrad. Actually the right position of the field stop with respect to the receiver focal point is a crucial parameter to determine the overlap function. So the position of the field stop can be slightly moved along the optical axes. After a collimating achromatic doublet, two folding mirrors direct the light toward an eight-channel polychromator unit (Figure 4.8).

The optical setup of AMPLE was optimized with the commercially available optical ray-tracing software ZEMAX[88]. Major design requirements were devoted to optimize the telescope size and all receiving channel so that the image of the far field were contained within the corresponding photocathode. Furthermore, transmission properties of all receiver channels were evaluated to optimize performance of all optical elements, also by considering polarizing effects and angular-dependent transmission properties of the polarizing beam splitters.

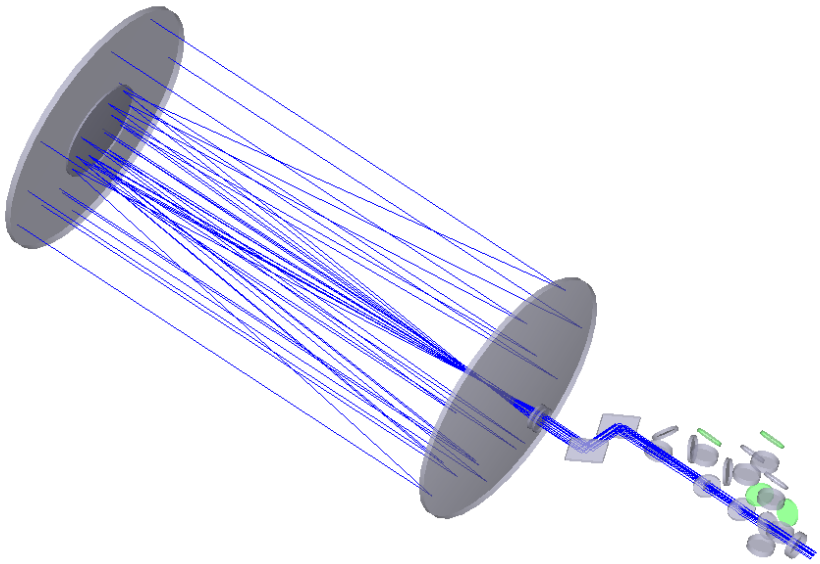

Fig.4. 9 Receiver system overview as designed through the ZEMAX ray tracing software.

The figure 4.8 represents the optical layout of the whole receiving system with the Dall-Kirkham telescope and the modeled optics behind the primary mirror. These optics are shown in detail in the figure 4.9 showing the optical configuration adopted for the receiving polychromator. In order to evaluate the optical efficiency of the whole system at each wavelength, the optical surfaces have been modeled considering its own coating.

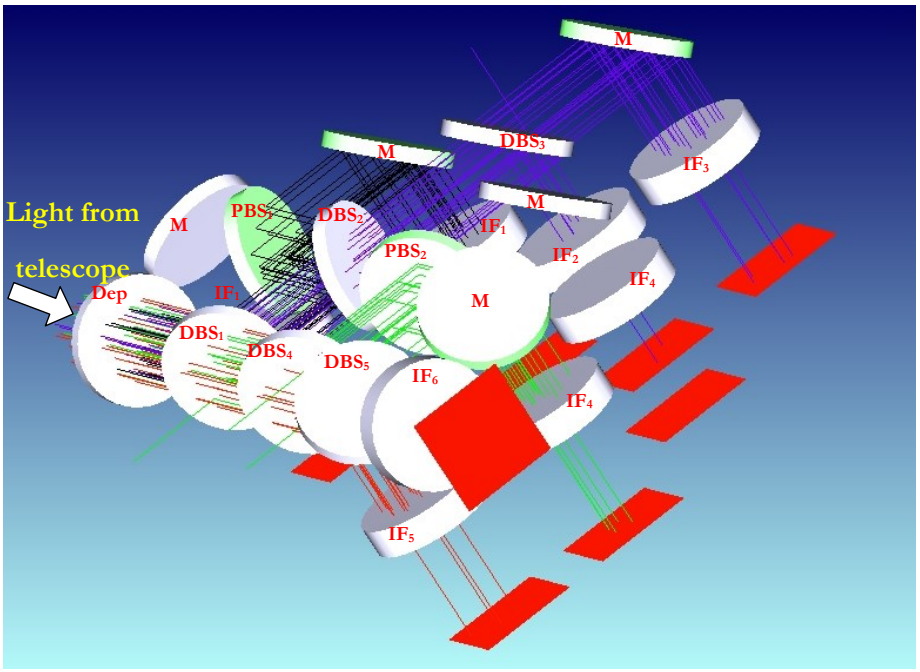

Fig.4. 10 Overview of the polychromator system as designed through the ZEMAX ray tracing software. The adopted nomenclature is the same of the figure 4.7. Red squares represent the positions of the detectors.

The positioning of the achromatic doublet L_c was carefully evaluated since from this parameter depends the collimation of the light beam inside the polychromator. In fact, the beam divergence (at all wavelengths) is a key parameter for the optical efficiency of the system because of the use of very selective interferential filters. Actually, interferential filters from BARR working at very narrow band have a good transmission only for normal incidence of light; otherwise losses of transmission efficiency can influence the measurements, especially in Raman channels. Figure 4.11 shows this effect.

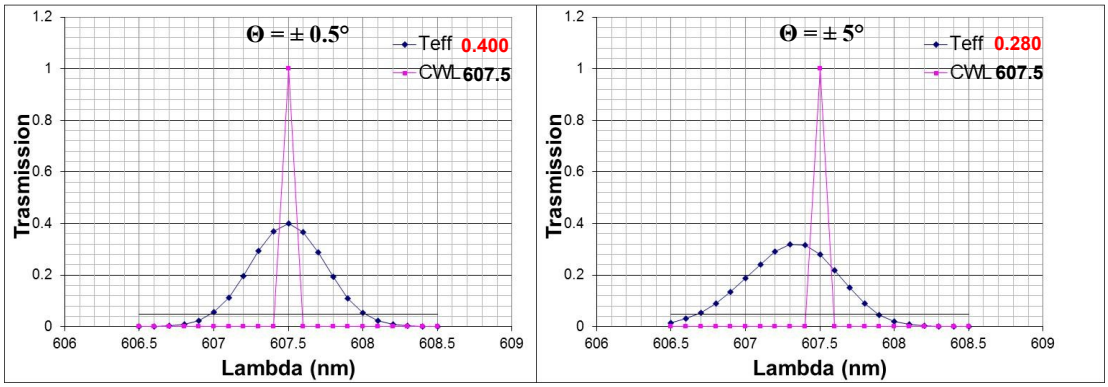

Fig.4. 11 Simulation showing the transmission drop (from 0.4 to 0.28), when angle of incidence on interferential filter goes from 0.5° to 5°.

Optimization process allowed keeping the final divergence to less than 1.5° for all the channels, thereby taking the effective transmissivity very close to that one stated from factory.

Furthermore, closely related to divergence of light beam, is the spot size on the photomultiplier input surface, clearly limited by the size of the photocathode itself. Pictures from 4.11 to 4.16 show the spot size for different channel, at right wavelength, and at the distance of photocathode.

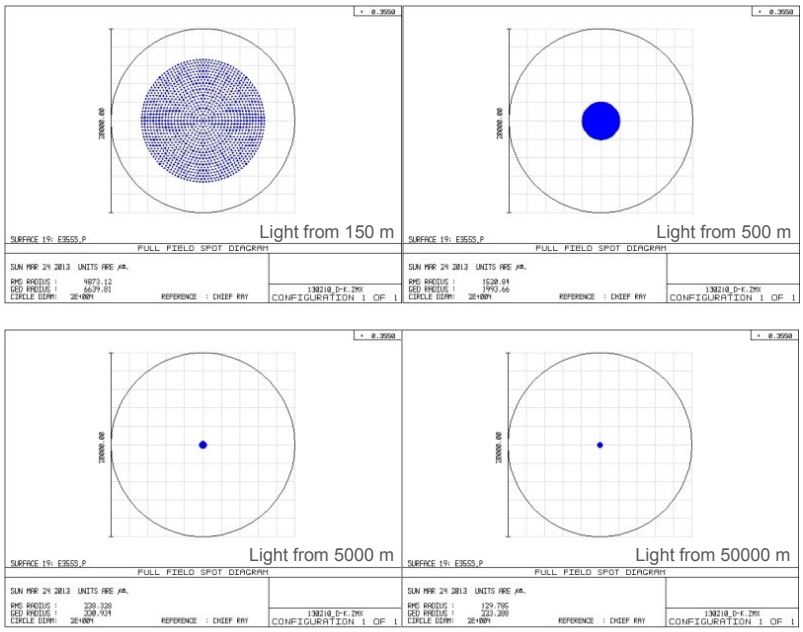

Fig.4. 3 Figure above shows the spot size at 355 nm compared with a circle of 20 mm that can be considered as the collecting effective area of the light detector.

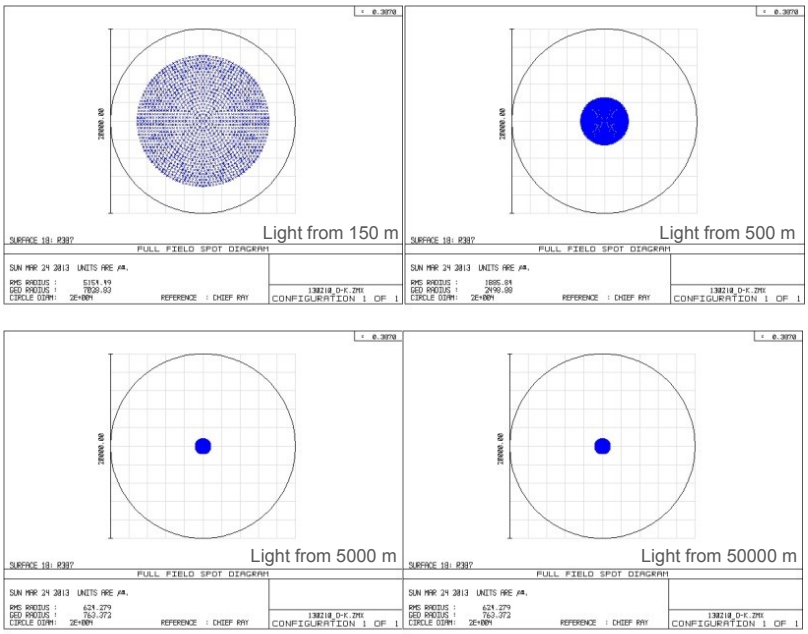

Fig.4. 4 Figure above shows the spot size at 387 nm compared with a circle of 20 mm that can be considered as the collecting effective area of the light detector.

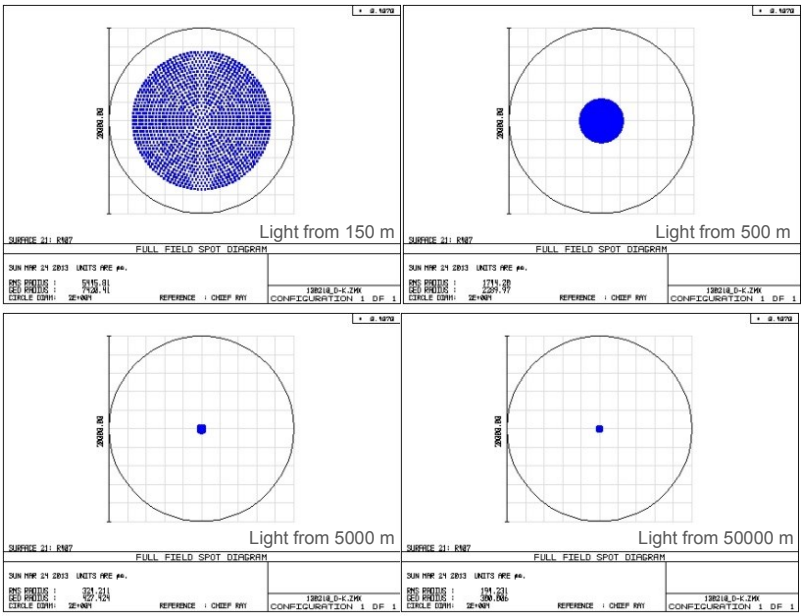

Fig.4. 5 Figure above shows the spot size at 407 nm compared with a circle of 20 mm that can be considered as the collecting effective area of the light detector.

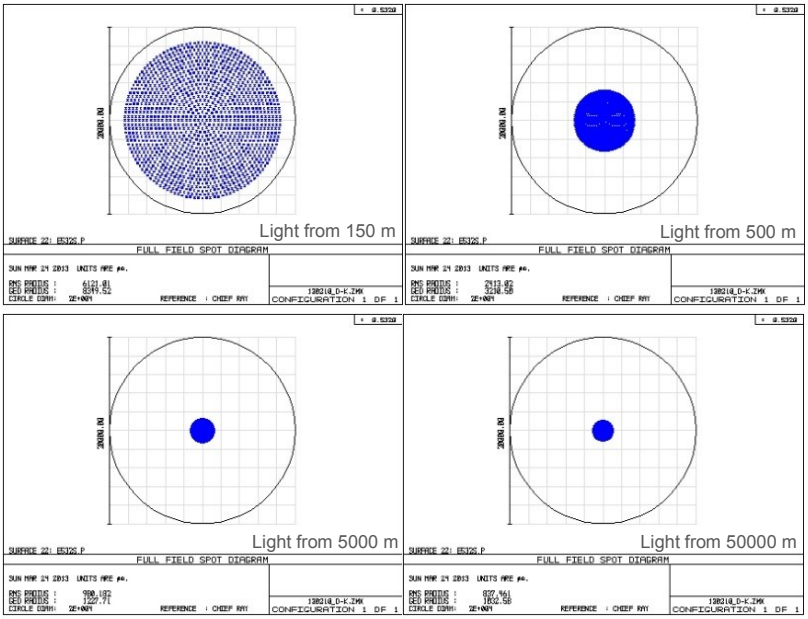

Fig.4. 6 Figure above shows the spot size at 532 nm compared with a circle of 20 mm that can be considered as the collecting effective area of the light detector.

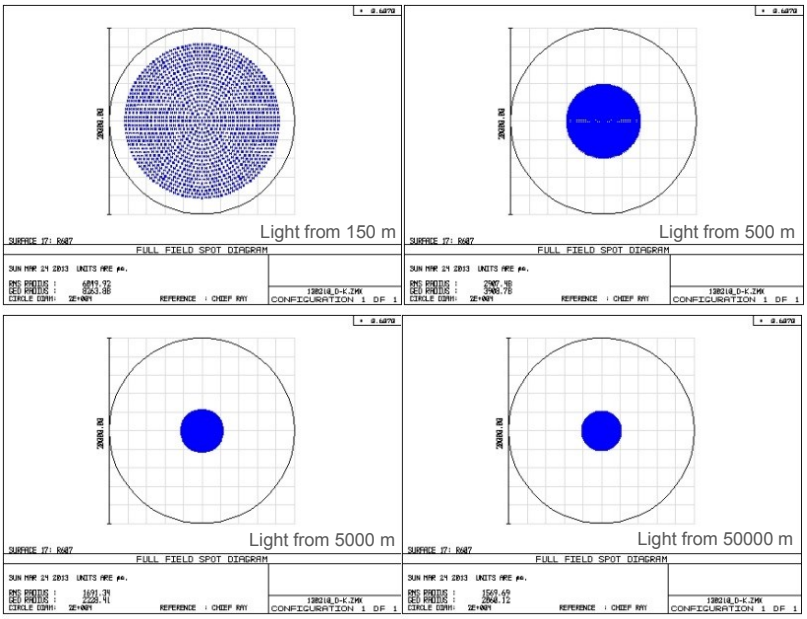

Fig.4. 7 Figure above shows the spot size at 607 nm compared with a circle of 20 mm that can be considered as the collecting effective area of the light detector.

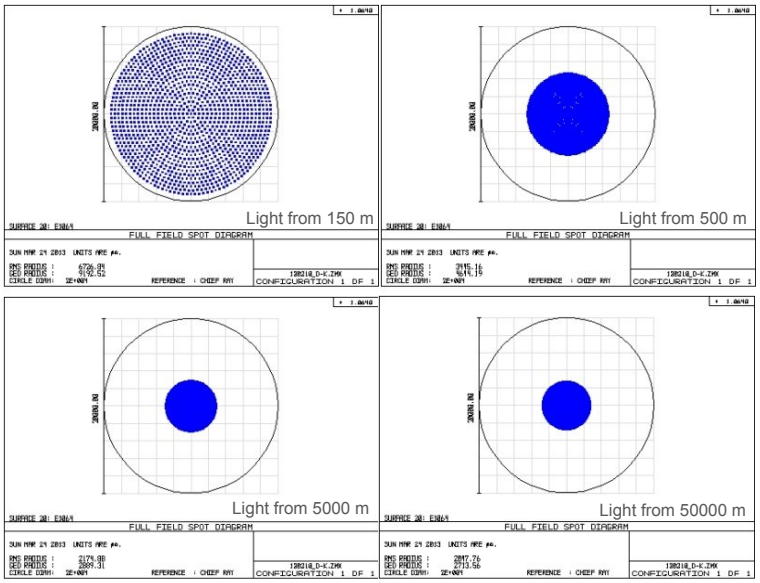

Fig.4. 8 Figure above shows the spot size at 1064 nm compared with a circle of 20 mm that can be considered as the collecting effective area of the light detector.

The lidar signals are detected with Hamamatsu head-on photomultiplier modules. The PMT model H7360-01 is used to detect the UV and green light, directly in photon counting mode. The implemented system does not mount yet the Raman channel at 607 nm and the elastic channel at 1064 nm. The detection of the former will be provided through a Hamamatsu H-7422-20 photomultiplier, in photon-counting mode. Finally, the IR radiation will be detected by a Licel avalanche photodiode

(Silicon type), i.e. model APD-3.0, through a transient recorder. All the remaining signals are acquired through a PCI fast commercially available four-input multiple-event time digitizers that can be used as ultrafast, single photon counting multiscaler. Each detected signal is acquired with a spatial resolution varying from 2 to 30 m. Moreover, polarization purity of laser line will allow performing polarization measurements at both 355 and 532 nm. Mechanical layout of the polichromator is shown in figure 4.18.

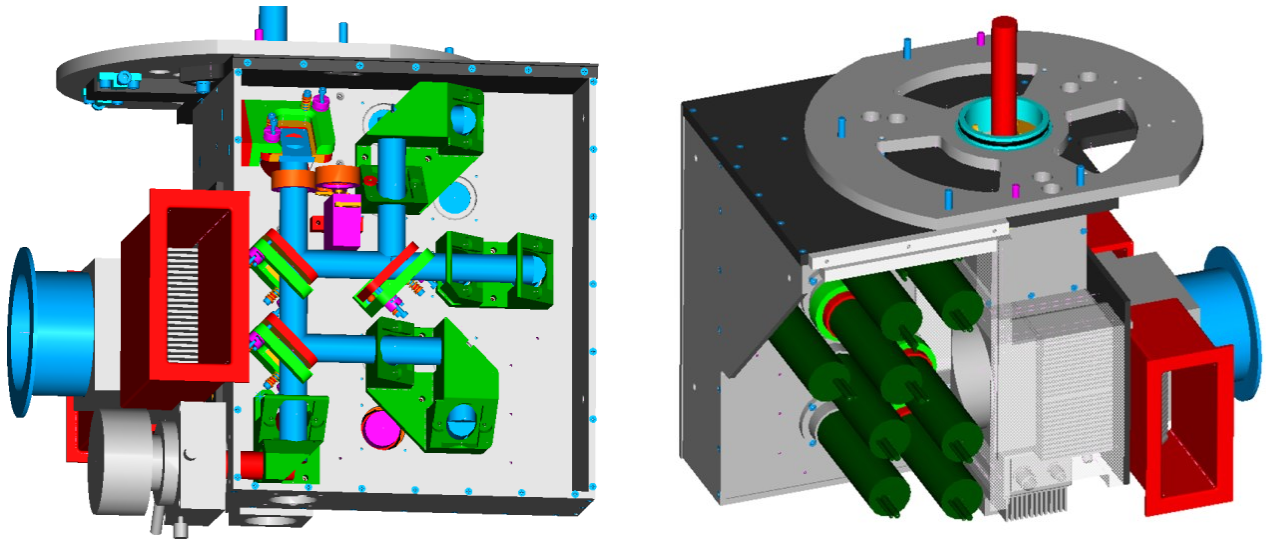

Fig. 4. 18 Mechanical layout of the polychromator. On the left the optical bench is put in foreground, while figure on the right highlights the detector arrangement.

The AMPLE system has been designed to perform 3D measurements by scanning the atmosphere along the azimuth and the zenith angles.

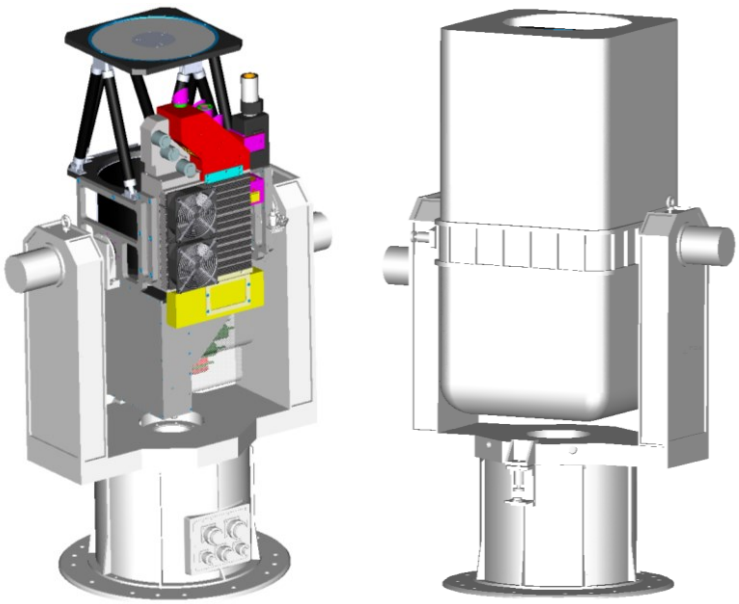

Fig. 4. 19 Mechanical Layout of the AMPLE system without (left) and with cover (right).

By means of two synchronous motors and two absolute optical encoders, the system can be pointed with a scanning speed of $10° s^{-1}$ in both directions, with a precision better than 1'. In the figure 4.19 the layout of the complete system is illustrated. The mechanical support for the scanning sub-system has been designed, made and tested by the BRIT institute of Beijing (PRC).

5. Lidar measurement with the three systems

In this chapter results on lidar measurements performed over the three year of the PhD period will be discussed. In particular, measurement campaign performed with MALIA system and concerning the Eyjafjallajökull ash outbreak will be discussed in the first section. Afterwards, it will be shown results about the field campaign performed on Mt. Etna in November 2010, when a moderate volcanic activity took place. Finally, preliminary results obtained with the AMPLE lidar system will be shown.

5.1 Eyjafjallajökull Lidar measurement campaign

The Eyjafjallajökull volcano in Iceland entered an explosive eruptive phase on 14 May 2010 and this event lasted until 21 April 2010. During this period, in the proximity of the volcano, the eruption plume reached a maximum height between 2 and 9.3 Km. Depending on the wind direction, the eruption plume was transported toward different regions of Continental Europe and toward the Atlantic Ocean at different altitudes. Even though this eruption had a moderate intensity, it had a strong impact on air traffic. In order to prevent possible damages to aircraft engines, the airspace over a large part of Northern Europe was closed on 15 April when the first part of the eruption plume reached Continental Europe. Air traffic restrictions and partial closure of European airspace were not uniform during the eruption period and differed from region to region depending on the volcanic ash transport pattern and the (sparse) information on height and density of volcanic aerosol at the time. The coordinated observations by the European Aerosol Lidar Network (EARLINET) and a methodology that was specifically designed for this event provided a detailed description of the 4-D distribution of the volcanic cloud over Europe for the whole event.

In this context, the MALIA apparatus was utilized in the framework of the EARLINET network to measure optical properties of the Eyjafjallajökull ash plume above the city of Napoli. After the eruption of Eyjafjallajökull volcano, ashes outbreaks measurements campaign has been performed at Naples EARLINET lidar station, starting from 15 April 2010 (table 5.1).

Day	StartTime	StopTime	Volcanic Plume
20100415	18.15	18.45	
20100416	17.05	17.35	
20100417	22.15	23.59	
20100418	0.00	2.38	
20100419	6.40	7.10	
	9.50	18.34	v
20100420	6.08	15.05	v
	18.20	19.22	v
20100421	11.27	23.59	v
20100422	0.00	1.43	v
	8.25	15.59	v
20100425	14.37	17.12	v
20100426	10.25	11.59	v
	14.35	18.48	v
20100427	14.32	15.49	v
20100428	7.54	9.29	v
20100429	6.48	19.01	v
20100430	7.46	9.13	v
	13.21	14.23	v
20100505	14.00	18.50	v
20100508	17.30	19.35	v
20100509	6.36	8.42	v
	17.41	19.36	v
20100510	12.30	14.03	v
	18.53	19.55	v
20100513	12.51	19.11	v
20100514	8.08	17.03	v
20100519	10.13	12.19	
20100520	10.20	10.50	
20100524	12.11	13.23	

To identify the origin of the sounded air masses, computed backward trajectory analysis has been used. 10-days HYSPLIT[89] back-trajectories provided by NOAA were used because such a model allows selecting the arrival time (with 1 hour of resolution) and three arrival altitudes above the lidar station. Moreover, lidar activities were programmed and performed on the base forecast by the Iceland Meteorological Office and the Met Office London Volcanic Ash Advisory Centre (VAAC).

The first signatures of ashes observed over Naples took place on 19 April (mostly between the top of planetary boundary layer and 8 Km height) and the last detection happened on 14 May, 2010. In the following, some selected days have been chosen and discussed.

The figure 5.1 reports the color maps of the logarithm of the lidar range corrected (RCS) signal for elastic measurements at 355 nm (a), at 532 nm (b), and linear volume depolarization (LVD) at 532 nm acquired on 21 April, 2010, when two ashes layers were observed above 4.5 km.

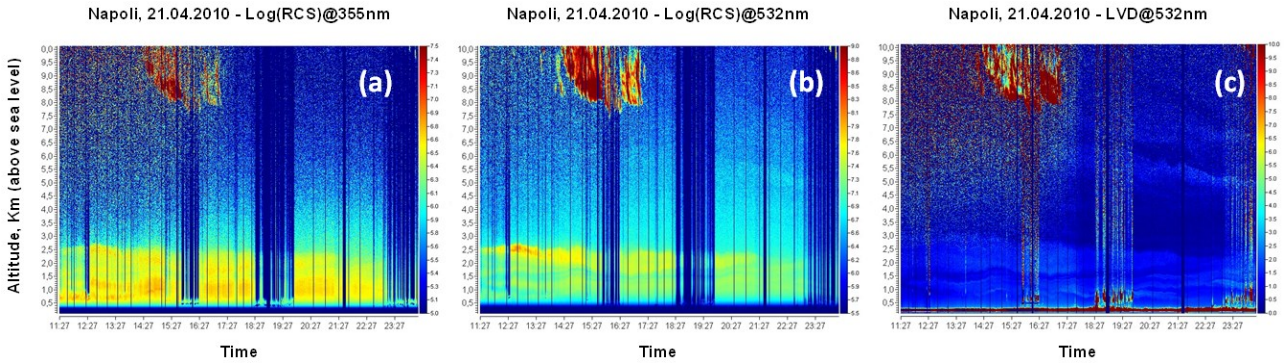

Figure 5. 1 On 21 April 2010, after 17:30UT, two thin volcanic clouds appeared between 4.7 and 8.4 Km (a.s.l.) above lidar station in Napoli. Figure (a) represent the logarithm of range corrected signal (RCS) at 355 nm, where there is no appreciable signs of aerosols above 2.6 Km. Figure (b) shows the ln(RCS) at 532 nm: some traces of particles can be seen after 21.00UT at 5 Km height. The linear volume depolarization ratio (c) colour plot shows the volcanic ash plume starting from the sunset (at about 17.30UT) at 5.5 Km and sliding dropping down at 4.7 Km. The time resolution of the plotted maps is 1 minute.

The color plots of the range corrected signal at both wavelength in figure 5.1 show that, actually, only week aerosol signature had been detect above the boundary layer (at 2.5 Km). In fact, the volcanic cloud clearly appears in the depolarization signal in figure 5.1(c). During measurements cirrostratus type (Cs) clouds appeared between 13.00 and 17.30 UT. Furthermore, low clouds were present. Hence, to evaluate the optical properties of the lifted volcanic aerosol, only lidar signals between 19.00 and 23.00 UT were considered and the low level clouds were skipped in the data integrations. In figure 5.2 the profile of particle backscatter, extinction and linear polarization coefficients are reported.

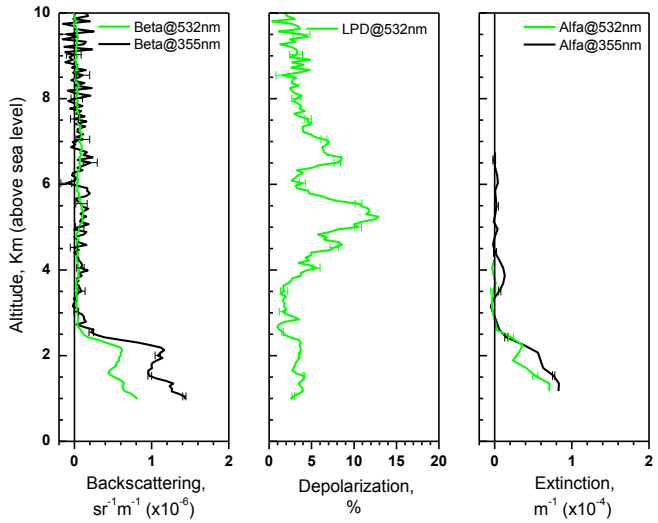

Figure 5. 2 Aerosol backscattering at 355 and 532 nm, linear particle depolarization and aerosol extinction at 355 and 532 nm measured from MALIA on 21 April, 2010. The integration time was 240 minutes, starting at 19:00 UT, corresponding to night-time conditions.

As figure 5.2 shows, the measured mean backscatter coefficient at low altitude (below 2.6 Km a.s.l.) is ~$1 \cdot 10^{-6}$ $m^{-1}sr^{-1}$ and ~$0.5 \cdot 10^{-6}$ $m^{-1}sr^{-1}$ at 355 nm and 532 nm, respectively, with a 10% of error. This wavelength dependency is typical of anthropogenic aerosol inside the planetary boundary layer. This is also confirmed by low value of linear particle depolarization (δ_{aer}) ratio below 2.5 Km, which means that such a layer is mainly composed by small particles. The low measured values for particle extinction did not allowed to evaluate the aerosol extinction to backscatter ratio (lidar ratio) for the layer of interest. In spite of this, the δ_{aer} coefficient profile was correctly evaluated and the maximum found value 13% ± 5%. Finally, the evaluated backscatter related color index in the layer between 4.5-8.7 Km was 1.1 ± 0.6.

The lidar measurements performed on 08 May 2010 had shown a clear evidence of an high depolarizing aerosol layer between 3.0 and 4.2 Km, as the figure 5.4c clearly shows.

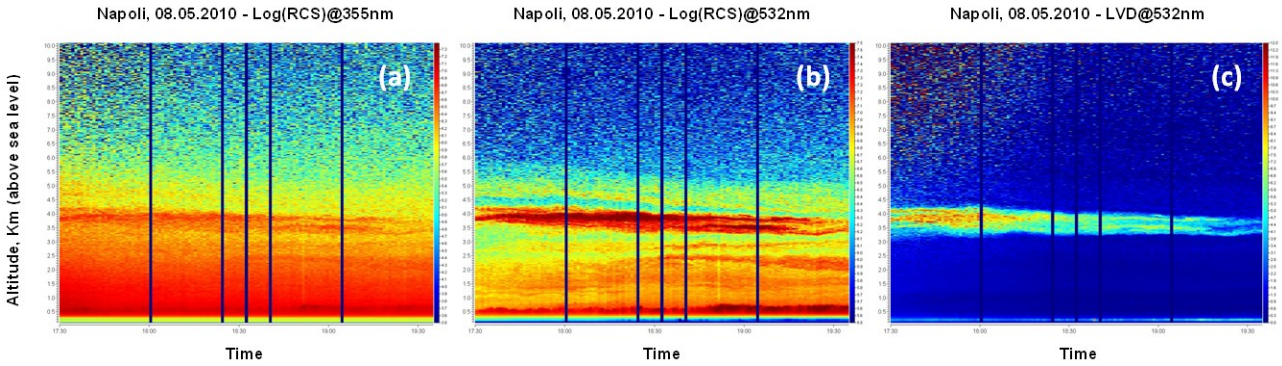

Figure 5. 3 Lidar measurements on 08 May 2010, between 17.30 and 19.35 UT. Figure (a) represent the logarithm of range corrected signal (RCS) at 355 nm. Figure (b) shows the ln(RCS) at 532 nm. The linear volume depolarization ratio (c) colour plot shows the volcanic ash plume between 3 and 4.2 Km height. The time resolution of the plotted maps is 1 minute

The two ours measurement stared just after the sunset at 17.30 UT. False color map (a) and (b) in figure above show an quite complex atmospheric layering, but only one layer is clearly depolarizing the light. In the figure 5.4 below the main features of the suspended particle are reported.

This is the best set of measurement we performed since they were acquired in night time condition and without low clouds. According to the backward trajectories, air masses came over Napoli from West, after they were transported over the Iberia Peninsula. This means that volcanic ashes remained several days above the Atlantic Oceans and this could have influence on the optical properties. The volcanic aerosol can be identified by the high value of aerosol linear depolarization, which in these measurements reaches the peak value of 11% (± 5%). It was located between 3.0 and 4.2 Km. The measured value of optical depth at 532 nm was estimated as $(5.5 \pm 1.0) \cdot 10^{-2}$ and the corresponding lidar ratio was 44 ± 5 sr.

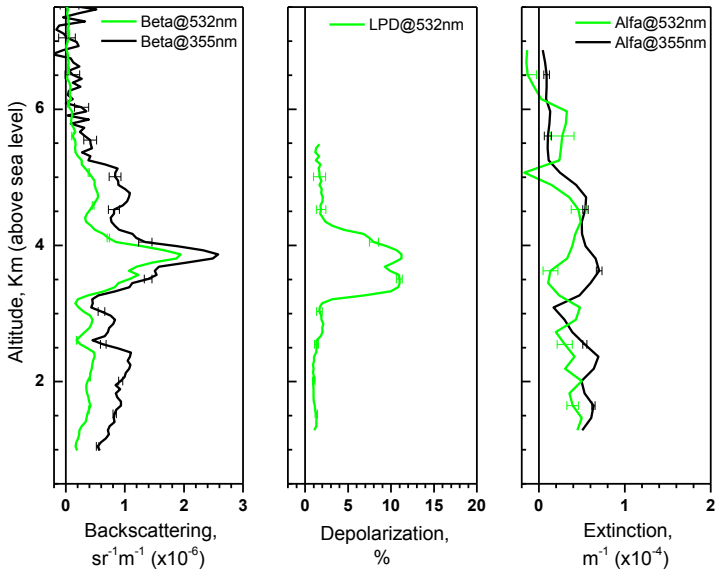

Figure 5. 4 Aerosol backscattering at 355 and 532 nm, linear particle depolarization and aerosol extinction at 355 and 532 nm measured from MALIA on 08 May, 2010. The integration time was 120 minutes, starting at 17:30 UT, corresponding to night-time conditions.

Similarly, OD measured at 355 was $(8.4\pm1.3)\cdot10^{-2}$ with a lidar ratio of 45 ± 5 sr. These valuesof L are in agrement with those measured over Potenza[90], but they are less than those observed over Germany, where Ansmann[91] and Wiegner[92] reported on values in the range from 50 sr to 60 sr. Differences can be due to the longer journey of the particle from the source up to Southern Italy.

Figure 5.5 shows another dust outbreak occurrd over Napoli, bu in this case it was a mixture of volocanic ashes and Saharan dust. In fact, from backtrajectories analysis (figure 5.6) it is clear that air masses from Iceland traveled over the Atlantic Ocean and, before reaching the Southern Italy has some time above the North Africa.

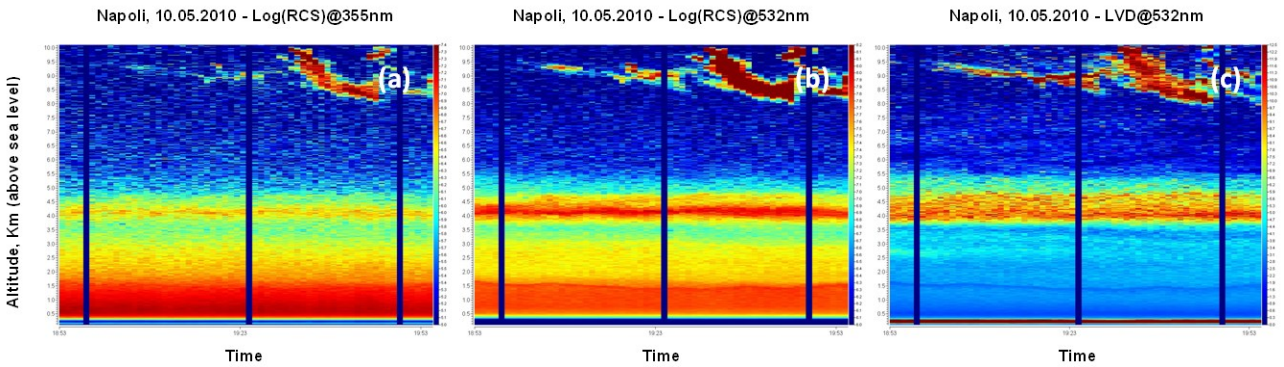

Figure 5. 5 Lidar measurements on 10 May 2010, between 18.53 and 19.55 UT. Figure (a) represent the logarithm of range corrected signal (RCS) at 355 nm. Figure (b) shows the ln(RCS) at 532 nm. The mixing of dust presence in the atmosphere above Napoli is highlighted by the high values of the linear volume depolarization ratio in the colour plot (c). The time resolution of the plotted maps is 1 minute

The logarithm of range corrected signal at both wavelength shows an aerosol layer from ground to almost 1.5 Km and depolarization value suggest that this is typical of local, anthropogenic particles. Just above this, there is another layer extening up to 3 Km and finally a third one ranging from 3.5 up to 5.5 Km. Cirrostratus type (Cs) clouds were present above 8.5 Km.

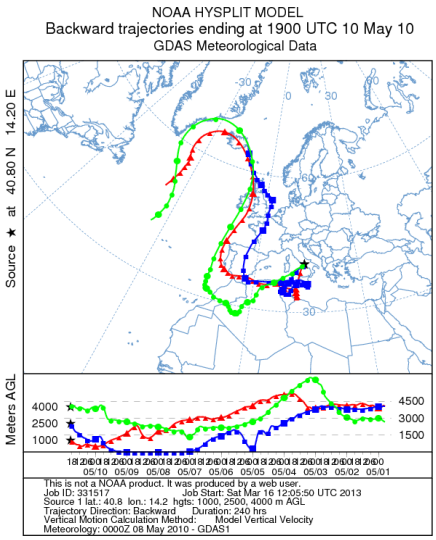

Figure 5. 6 Computed 10 days back-trajectories (by HYSPLITT model) for arrival on 10 May 2010 at 19.00 UT, at 1000, 2500, and 4000 m. As picture shows, air masses originated over Atlantic Ocean passed over the Iceland and after three days over the Sahara desert, and then ended over Napoli.

The presence of desert dust in the volcanic plume was confirmed by lidar data analysis. In fact, the color index value below 1.5 Km was found to be 0.9 ± 0.1, while in the 1.5-3 Km and 3.5-5.5 Km layers it was 0.0 ± 0.1 and 0.2 ± 0.1, respectively, clearly indicating the presence of large particles like desert soil one[93].

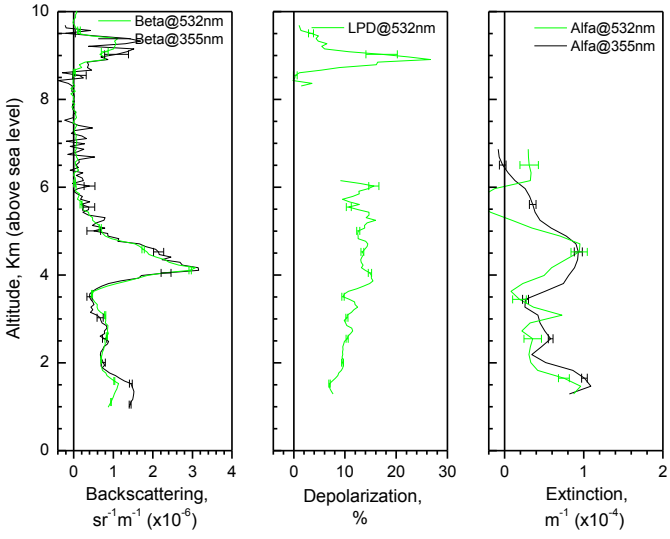

Figure 5. 7 Aerosol backscattering at 355 and 532 nm, linear particle depolarization and aerosol extinction at 355 and 532 nm measured from MALIA on 10 May, 2010. The integration time was 60 minutes, starting at 18:53 UT, corresponding to night-time conditions.

Furthermore, lower lidar ratio values (with respect to previous days) also confirm this thesis; measured values of L are 35 ± 4 and 30 ± 5 in the 1.5-3 Km and 3.5-5.5 Km layers. Linear particle depolarization was slowly increasing from 8% to 15%.

5.2 Lidar measurement campaign over the Etna volcano

The lidar measurements of volcanic clouds can play a key role for the validation of numerical dispersal models of ashes and, thus, for the mitigation and prevention of the associated risks caused. Therefore, it may be useful to install a permanent lidar station close to the active craters of the Mt. Etna for continuous monitoring of volcanic emissions.

To test the feasibility of using a high frequency lidar in dense aerosol layers, a field campaign was carried out on 2010 as collaboration of the CNISM, INGV and INAF institutions. Therefore, in July 2010, the VAMP lidar (described in the chapter 4) has been moved in July 2010 on the slope of the Mt. Etna and it was located in one of the astronomical domes of the astronomical site Serra la Nave, ~7.5 Km far away from the central craters of the volcano. Lidar measurements were performed when, under safe conditions, an explosive activity of the volcano took pace.

Lidar measurements of fresh volcanic ashes were performed on just emitted plume volcanic during the activity started at 06:40 UT of November 14, 2010, and involving two of the summit craters, namely the Bocca Nuova Crater (BNC) and the North East Crater (NEC), which produced several ash emission events. Lidar measurements were performed between 12:30 and 17:30 GMT of November 15. Volcanic ash was collected during the monitoring activities of the INGV, and was mainly composed by juvenile[c] with irregular shape[94]. During field surveys of volcanologists on duty, high degassing was continuously observed from the BNC[95]. Hence, two different plumes were present during the measurements.

Since the VAMP system was a single wavelength elastic lidar (at 532 nm), it allowed the detection of the elastic backscattered signal only. However, the knowledge of the extinction-to backscattering ratio (L) is required in order to obtain more information from measurements performed by this apparatus. To overcome this problem, the mean value of the lidar ratio in the plume was evaluated through an iterative procedure, by comparing the measured profile with a reference molecular profile in two regions located before and behind the plume, respectively. In this way, the optical depth (OD) of the plume was directly evaluated as $OD=0.5\cdot\ln(\gamma_b/\gamma_a)$, γ_b and γ_a being the normalizing factors between lidar and molecular signals, estimated in the two regions where the aerosol load could be assumed negligible[96]. In these conditions, starting from a first guess of the mean value of L (L_0 = 45 sr),

[c] The term *juvenile* indicates the material emitted during a volcanic eruption that originates directly from the magma.

the backscatter coefficient profile is obtained through the Klett-Fernald analytical algorithm, and a new mean value of the L (L_1) is evaluated from the ratio between the above estimated value of OD and the integrated value of the particle backscatter coefficient in the volcanic plume. The value L_1 is then used for a new iteration. This procedure converges after a few iterations. A change of a factor 2 of the first guess value brings no appreciable changes in the results for the mean value of L in the plume.

The presence of the two above mentioned aerosol-free regions (before and behind the volcanic plume) allowed us to check the reliability of the solution for L. Actually, a different procedure was also followed to determine the L mean value of the plume, by evaluating the backscattering profile with the constraint of null value of the particle backscatter coefficient in the two aerosol-free regions. These two different approaches allowed us to estimate the errors on L mean values evaluation as deviation of the two results; they resulted lower than 20% in all cases. Therefore, this deviation has been considered as the error of the L value in the subsequent analysis.

Detailed description of the error analysis is in the chapter 3. Here it is only underlined that the error calculations regarding the Klett-inversion affecting the particle backscatter coefficient at range z was evaluated by taking into account four contributions: i) the error on L, ii) the error on the signal at z, iii) the error on the signal at reference range (z_0), and iv) the error on the particle backscatter value at z_0. The statistical error on signals acquired with the VAMP system is a function of the distance of the sounded atmospheric volume, and of data binning on time and space. For day-time, clear sky acquisitions, at a distance of about 7 km, the typical statistical error on 1 minute integrated total elastic signal, with a spatial resolution of 30 m, was of the order of 10% and 30% for the P and S components, respectively. Moreover, in the presence of plume (at about 7 km), the high levels of both P and S signals lead to corresponding statistical errors of about 5%, and 10%, respectively, for an integration time of 60 s, and 30 m spatial resolution. In night-time conditions, and with a 20 s integration time and 30 m spatial resolution, the statistical errors were of the order of 5% for both P and S channels in the volcanic plume.

The reference point is chosen within the range where the lidar signal can be fitted with a pure molecular profile so that the particle scattering at this point is negligible with respect to Rayleigh scattering, and the fitting pure molecular profile at z_0 is considered instead of the elastic signal in the inversion algorithm. With this method the error on the backscattering profiles linked to the choice of the reference point depends, in practice, only on the atmospheric model accuracy, and can be kept as low as of 2-3%.

Another source of error can be the multiple scattering (MS) that is often observed within high depolarizing particles layers[97]. In order to avoid misinterpretation in depolarization measurement

results, an evaluation of the influence of MS in our measurements was done by plotting the mean linear volume depolarization versus the OD estimated in our volcanic ash measurement campaign. As figure 5.8 shows, no evidence of a dependence of mean linear volume depolarization on OD is found for optical depth values even up to 1.4. This is mainly due to the high depolarization nature of the volcanic ash, and their relative short distance from lidar system. As further caution, to avoid any possible MS influence only profiles corresponding to OD lower than 0.5 in the volcanic plume were considered.

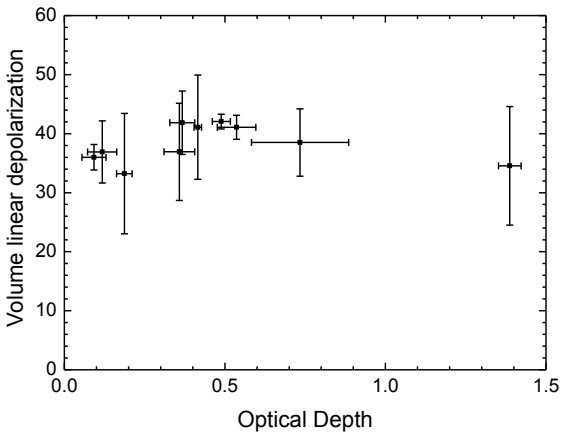

Figure 5. 8 The scatter plot of volume linear depolarization (δ_V) versus estimated optical depth (OD) of the plume from NEC indicates that there is a small influence of the multiple scattering on the signal return. Error bars represent the standard deviations on δ_V and OD. Data refers to ash emission of November 15, 2010.

The figure 5.9 shows the operative scenario. The wind was blowing from the West direction in the morning so that the two plumes from the active craters were approximately in the same line-of-view from the lidar site. Therefore, they could not be scanned separately, and appear at different time ranges in the same lidar signals.

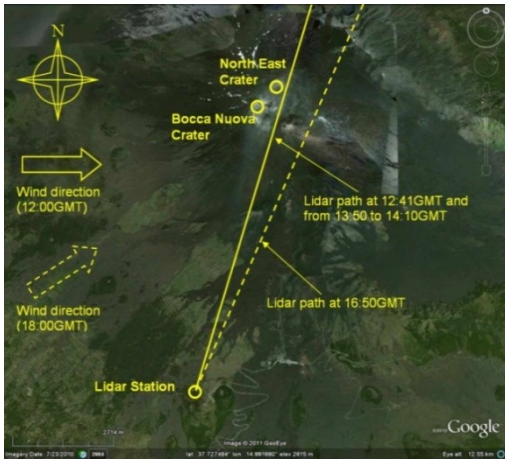

Figure 5. 9 Illustration of the measurement field. The Lidar station of INAF Serra La Nave Astronomical Observatory is located at 1760m a.s.l. (14.97°E, 37.69°N), about 7.5 Km far away from the Bocca Nuova Crater (BNC) and North East Crater (NEC) that are also are

shown. Lidar pointing directions are reported together with the corresponding wind direction at about 4600m a.s.l. (Google Earth).

During the day-time measurements (12:38 – 13:29 GMT), the plumes from the BNC and NEC showed some degree of mixing, hence, for these measurements, we only had the possibility to retrieve the mean value of particle L for the overall plume. The estimated mean values of the L for 10 lidar profiles varied between 30 sr and 45 sr. Even though the backscattering profiles did not show well separated layers, a clear difference in the δ_{aer} profile was observed.

Particle backscattering and linear particle depolarization profiles acquired in day-time condition with an integration time of 60 s are shown in Figure 5.10. Applying the Klett algorithm for backscattering retrieval, LR values of 60 sr and 30 sr were used in the ranges 4.5-6.2 km and 6.2-7.5 km, respectively. In the layer between 4.5 and 6.2 km, the mean value of δ_{aer} was (5±1)%, due to diffuse aerosol contribution, while the backscatter coefficient value was of the order of $4 \cdot 10^{-7}$ $sr^{-1}m^{-1}$.

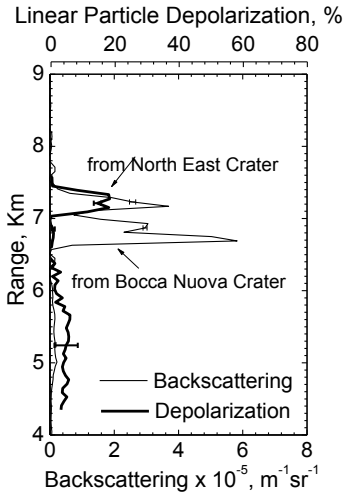

Figure 5. 10 Particle backscattering and linear particle depolarization profiles measured at Serra La Nave – Mt. Etna, November 15, 2010. Data were acquired at an elevation angle of 14° (corresponding to 250-300m of altitude above Mt Etna top) and at 17° of azimuth angle (clockwise with respect to North direction) and. Integration time was 60 s, starting at 12:41GMT.

During these measurements the mean value of δ_{aer} was <1% between 6.6 and 7km (in the plume from the BNC), and (16±2)% beyond 7 km (in the plume from the NEC), respectively. These results suggest that ashes were localized between 7 and 7.5 km from lidar station, in the plume from NEC.

Figure 5.11 reports the results of a 65-minute measurement series started at 13.44 UT performed with a temporal resolution of 30 seconds, at a fixed direction and pointing 250-300 m above the summit craters of the volcano. The particle backscatter time series in figure 5.8a clearly shows two

different layers located at 6.5-7.0 km and 7.0-7.5 km far from the lidar station and emitted from the BNC and NEC, respectively, with the mean value of linear volume depolarization (shown in figure 5.8b) lower than 1.5% in the first layer and of (15±1)% in the layer beyond 7 km.

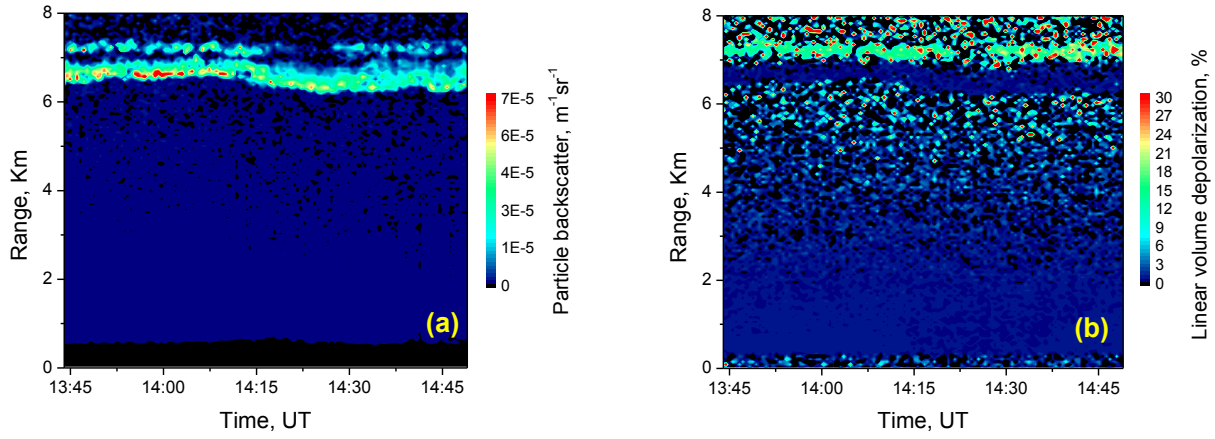

Figure 5. 11 65 minutes time series of backscattering (a) and volume linear depolarization (b) profiles at Serra La Nave – Mt. Etna, Italy, on November 15, 2010. Data were acquired with temporal resolution of 30sec at fixed direction defined by azimuth angle of 17° from North direction (solid line in Figure 5.6) and pointing 250-300m of altitude above Mt Etna top.

This figure clearly shows that volcanic ash emission was unsteady. In particular, a disappearance of the NEC emission from 14:16 to 14:23 UTC is evident. Analyzing the number of explosions between 13:45 and 14:22 UTC in one of the cameras of the surveillance system of the volcano, a drop in the ash emission episodes between 14:12 and 14:22 UTC was registered. Explosions occurred every 2.5 minutes with respect to 1.5 minutes retrieved between 13:45 and 14:12 UTC and between 14:22 and 14:45 UTC.

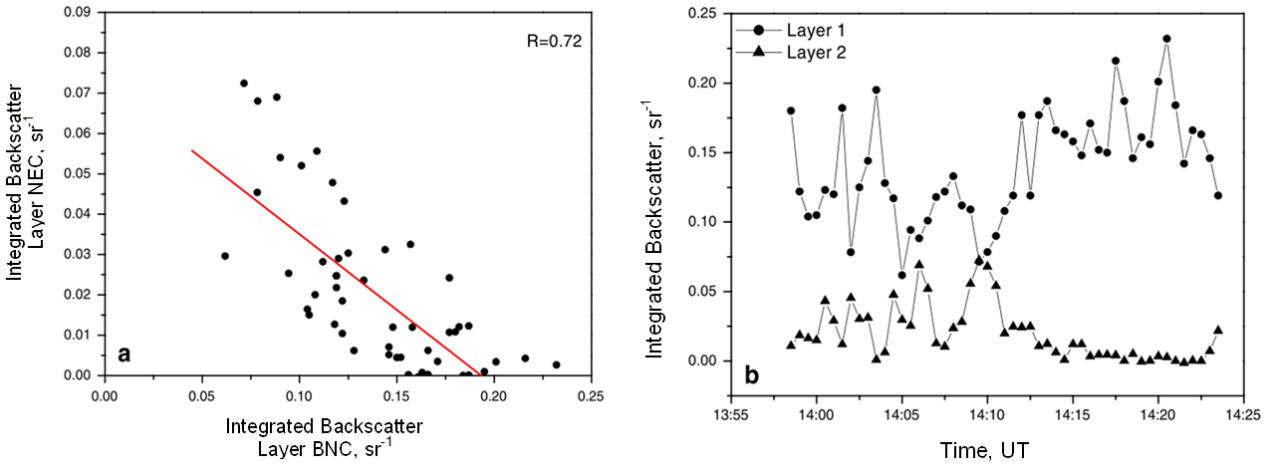

Figure 5. 12 Scatterplot of the plumes integrated backscattering from BNC (layer 1) and NEC (layer 2) and the linear best fit of the data (a) and their temporal behavior (b).

The figure 5.12 reports the scatter plot of the integrated backscattering of the two plumes. The negative correlation (R=0.72) between the two IBs shows some kind of interconnection from two different volcanic vents. In fact, summit crater can be considered a single crater named the Central Crater. It is, hence, possible that there is a connection among these different craters as suggested by Chester et al. (1985)[98].

Figure 5.13 shows the particle backscatter and depolarization profiles acquired after sunset. The plumes appear at longer distance with respect to the day-time measurements, due to a change in the wind direction and a different pointing angle (see also figure 5.6). The mean value of δ_{aer} in the plume was (5±2)% for the BNC, larger than that observed in the morning for the same plume. Moreover, an increase of the δ_{aer} mean value up to (45±3)% was observed in the plume from NEC. By averaging the LR values corresponding to fifteen 20-second measurements, we estimated the mean LR for the two plumes. We found LR values of 46 ± 10 sr and 36 ± 5 sr for BNC and NEC, respectively. These observations clearly indicate a change in the type of the emitted ashes in both plumes with respect to the day-time case. The higher value of LR in the BNC plume with respect to that of NEC can be explained by the presence of fine particles as, e.g., sulphate particles. These particles are produced by the typical gases emitted from volcanoes[99], and were also observed in the Eyjafjallajökull plume over Germany, as reported above.

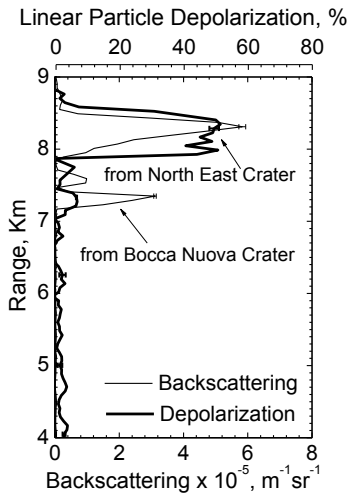

Figure 5. 13 Particle backscattering and total depolarization profiles measured at Serra La Nave – Mt. Etna, November 15, 2010. Data were acquired at 24° of azimuth angle (clockwise with respect to North direction) and corresponding at 250-300m of altitude above Mt Etna top. The integration time was 20 seconds, starting at 16:50GMT.

The contribution of depolarizing (ashes) to the depolarization ratio in the Eyjafjallajokull volcanic cloud over Lyon (France) was recently evaluated by means of the scattering matrix method[100] at 38.5%. Assuming that the plumes emitted by the two Mt. Etna craters were composed by different

concentrations of depolarizing (pure-ash) and non-depolarizing (non-ash) particles, the pure ash-related backscatter coefficient (β_a) can be retrieved from the simultaneous evaluation of the total particle backscatter coefficient β_{aer} and linear particle depolarization δ_{aer} by following the method proposed by Tesche et al.[101]:

$$\beta_a = \beta_{aer} \frac{(\delta_{aer} - \delta_{na})\,(1+\delta_a)}{(\delta_a - \delta_{na})\,(1+\delta_{aer})} \qquad (5.1),$$

where δ_a and δ_{na} are the depolarization coefficients of the depolarizing ash and of the weakly depolarizing non-ash particles, respectively. This method was already used by Ansmann et al.[91] to separate the contribution of coarse volcanic ash from non-ash aerosol in the total particle backscattering, by assuming a value of 36% for δ_a and 1% for δ_{na}. In the following calculation a value of (50±2)% for δ_a has been used, which corresponds to the maximum value of δ_{aer} measured in the ash plume, with the assumption that this value corresponds to a negligible contribution of non-polarizing particles, namely (1±1)%. Once β_a is known, the particle mass concentration of volcanic ash at emitting craters can be obtained by:

$$c = \sigma \cdot \beta_a \cdot L \cdot \varrho \qquad (5.2),$$

where L is the measured mean value of the ash lidar ratio, and ϱ the ash density, set to 2450±50 Kg/m^3, as found by Scollo et al.[102] by measuring ash particles erupted in 2002-2003 from Etna volcano, and for particle size between 0.125 and 0.006 mm, which is similar[103] to those found for particles having a diameter < 0.008 mm. In the equation (5.2), σ is the ash conversion factor, which is a function of the size distribution, and, for large values of the effective radius r_{eff}, is given by $2r_{eff}/3$[104,105]. For the volcanic ash cloud observed in Germany 50-110 hours after the Eyjafjallajokull eruption, Ansmann et al.[11] assumed a value of $0.6 \cdot 10^{-6}$ m for σ, corresponding to an effective radius of 1 μm. This assumption was based on Schumann et al.[15] findings about the removal by sedimentation of particles with radii > 15 μm after 48 hours. In our case, assuming a value of 10 μm for the effective radius of fresh emitted ashes, a value of $0.6 \cdot 10^{-5}$ m was used for the conversion factor.

The above considerations allow evaluating the ash mass concentration for just emitted plume. The errors on ash mass concentration are evaluated from statistical uncertainties of β_a, L and ϱ. The uncertainty on the effective radius and, therefore, on the conversion factor is a critical point, since it gives rise to a systematic error of the order of 50% on the ash mass concentration. Its contribution is not included in the showed results. The measurement at 12:41 GMT showed that the ash mass concentration was lower than 300 μg/m^3 and 4200±2100 μg/m^3 inside the plume from the BNC and the NEC, respectively. During the afternoon, from 13:50 to 14:10 GMT, the mean ash mass concentration emitted from the NEC was found to be 8500±4300 μg/m^3. The volcanic plume from

NEC had a maximum mass concentration of ash at 14:06 GMT, when the peak value of 24000±6000 $\mu g/m^3$ was observed. Finally, the measurement at 16:50 GMT showed ash mass concentration of 1000±900 $\mu g/m^3$ in the plume from the BNC and of 13000±5000 $\mu g/m^3$ in the plume from the NEC.

5.3 First lidar measurement with the AMPLE system

The above reported experiences highlight that the use of an high repetition rate laser in spite of a traditional one allow the use of lidar also for the detection of optical thick layers, like volcanic plumes. To improve this capability, a new apparatus has been designed to perform lidar measurements with higher dynamic. Furthermore, this lidar should operate to guarantee high efficiency volume scanning and to retrieve high quality 3D map of particle optical and microphysical properties and their time evolution. In this contest, the AMPLE (Aerosol Multi-wavelength Polarization Lidar Experiment) project was carried out as a cooperation with the Beijing Research Institute of Telemetry (BRIT) that had in charge of the design and implementation of the lidar scanning platform for the system. The main goal with this new system was to extend the dynamic range of the signal to provide accurate measurement of atmospheric optical properties. Actually, as showed in chapter 4, the dynamic of the signal could be improved by increasing the laser repetition rate and keeping constant the optical power. Indeed, just as a recall, the keystone for whole apparatus is the laser source, which is a doubled and tripled diode pumped Nd:YAG laser that is especially designed for this device, with a repetition rate of 1KHz and 0.6, 1.5, 1.0W of mean optical power at 355, 532 and 1064nm, respectively, that allowed to detect both Raman and elastic lidar returns, with depolarization measurements at 355 and 532 nm.

Hardware characterization and tests on all both optical (laser, dichroic beam splitters, interferential filters, polarizing beam splitters, depolarizer) and electronic (fast multi-channel scalers, laser controller) components have been carried out to ensure the require performances at CNISM Napoli Research Unit. Two different copies of the AMPLE have been realized. The first one has the possibility to measure backscatter at 355, 532nm, extinction at 355nm, water vapor signal at 407nm and depolarization at 355 and 532nm. The second copy has the possibility to measure elastic/Raman backscattering and depolarization at 355nm.

All optics were tested in laboratory and mounted only if they were inside the design specification. Special care has been put regarding the calibration of the measurement of the polarization. To perform such a measurement a depolarizer (Thorlabs mod DPU-25) can be inserted into the optical path through a motorized mechanism. This device was tested on optical bench to confirm that a virtually depolarized beam can be obtained (figure 5.14).

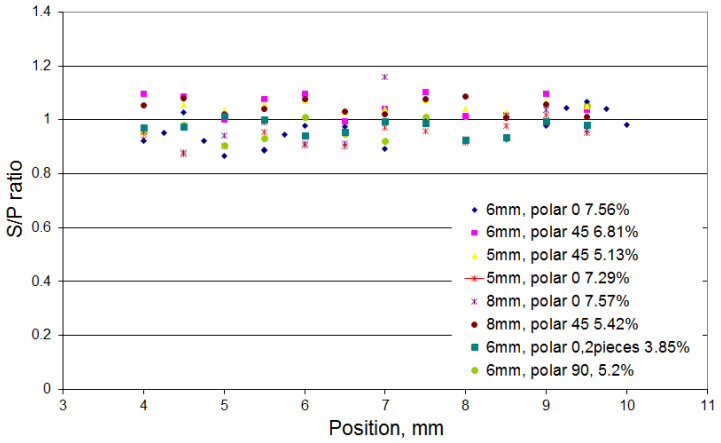

Figure 5. 14. Figure shows the optical characterization of the depolarizer performed at different position and for different sizes of the incident beam.

Then, the measurement of the normalization factor between P and S signals will be obtained by direct measurement of the ratio between the two channels (cfr. §4.1). The figure 5.15 shows the signals P and P acquired for the calibration measurement. The normalization factor is a direct measure of the system gain ratio (H).

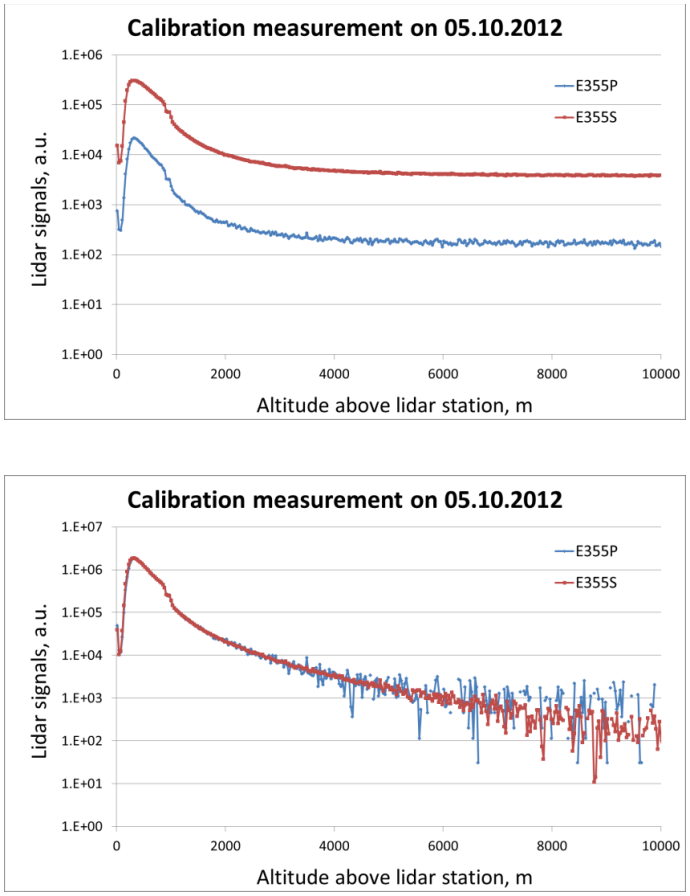

Figure 5. 15 Example of measurement for polarization calibration. The raw signals (a) were acquired on 13.34 UT on 05 October 2012. Difference in the signal amplitude can be due to the different gain of the photomultiplier used or to the different transmission optical efficiency

of the two channels. The normalization process allows making signals equal and evaluating the calibration constant (the gain ratio).

Once the calibration measurement has been performed, the system is ready to measure δ_{aer} according to the (3.17). The measurement of the ain ratio should be done often to prevent errors in the depolarization measurement due to changes in the gain of optical channel and photomultiplier modules.

Measures reported below have been performed with this new lidar system.

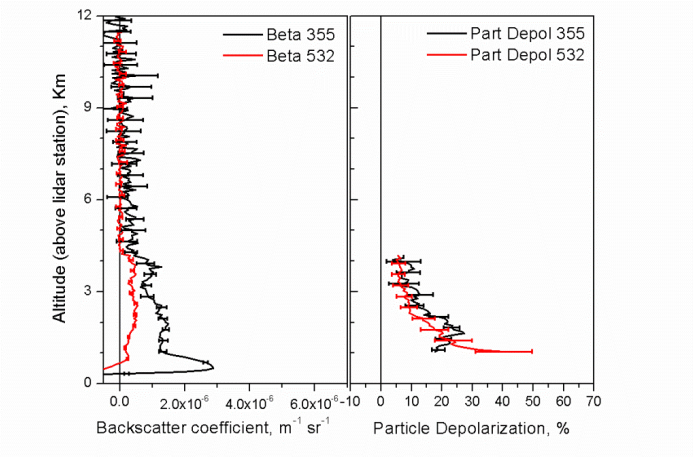

Figure 5. 16 Backscatter (left) and particle depolarization (right) profiles measure in Beijing on 10.10.2012. Integration time was 15min

Figure above shows an example of data by AMPLE system in Beijing. On the left of figure 5.16, the spectral behaviour of the backscatter coefficients at 355 and 532 nm in the 1.5 - 4 Km layer suggests that anthropogenic aerosol were present at the time of measure, whereas the measured value of particle depolarization (on the right) is consistent with the presence of desert dust. Indeed, the mixture of the two components shall be considered for that day.

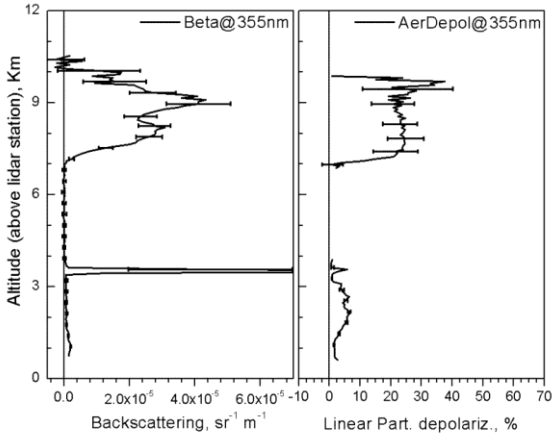

Figure 5. 17 Backscatter (left) and particle depolarization (right) profiles measure at Serra la Nave (Catania, Italy, 1760 m a.s.l.) on. Integration time was 15min

The second AMPLE instrument was installed on the slope of Mt. Etna in spite of the VAMP experiment. In figure 5.17 one of the first measures performed with this second apparatus is shown. It refers at a 30 minutes vertical measure on 16 October 2012. Figure clearly shows the presence of ice crystal in the cloud 7 Km over the Mt. Etna, while the cloud at 3.5 Km seems to be substantially a water cloud.

Conclusions

Due to the properties of the interaction between the radiation and the atmosphere constituents, the lidar technique has demonstrated to be a powerful tool to measure and monitor optical parameters of the atmosphere. The knowledge of the aerosol optical parameters with high resolution is very important because it permits to extract information about their micro-physical properties, their spatial distribution, and temporal evolution.

With respect to this general consideration, the focus of this thesis was to investigate implementation of a new, versatile and portable scanning lidar system devoted to the 4D mapping of the atmosphere. Furthermore, it has been highlighted the key role that lidar devices can play as tools to solve the problem of continuous monitoring of extremely thick aerosol layer. This need derives from the observation that in some cases the traditional instruments have difficulty in following the dynamic of lidar signals. This happens, in particular, when lidar instruments are used to probe particle layers with high optical depth. In fact, in these conditions, low repetition rate and high energy pulse lasers (traditionally used for such instruments) can cause non linearity in photo detection chain. The proposed solution for this problem is based on the adoption of a high repetition rate laser transmitter.

In the development of this thesis a short description of the atmospheric physical properties has been done, emphasizing some aspects related to aerosols. Then, the interaction between atmospheric components and sounding light was drawn: the different kinds of atmospheric scattering have been discussed as well as the extinction of the light. The remote sensing lidar technique has been introduced, describing the fundamental equations, the optical parameters that can be retrieved, and the main inversion algorithms.

The multi-wavelengths, polarization, Raman lidar system (MALIA) located in Naples has been described in detail, since it can be considered as the reference system for the two lidar devices developed afterwards, in particular VAMP and AMPLE systems, which are the two lidars that make use of a 1 KHz laser source. The VAMP lidar is also describes since it has been used to study the problems connected with the use of this configuration in a real field campaign. Furthermore, AMPLE system is depicted in detail, being this the first system designed to be a three backscattering, two extinctions, and

two polarization channel (in particular this feature with respect to traditional operating system) lidar, with scanning capability and based on high repetition rate laser source.

Interesting applications of this new lidar configuration here presented are the monitoring of volcanic plumes and high pollution aerosol layers. The former activity has arisen from the spotlight this particular type of aerosol had following the recent eruption of the volcano Eyjafjallajökull in April 2010. The latter follows from the consideration that traditional lidar systems do not allow measurements in high particle load condition, hence causing one of the more critical problems in atmospheric physics that is the lack in the characterization of the tropospheric aerosols from both optical and micro-physical properties, and their temporal and spatial distributions. To this last point, the East Asia region is a unique area in terms of photochemistry and aerosol loading and so it is a good location for testing the new apparatus.

Experimental results are reported in chapter 5. The MAILA activities concerns the measurements of Eyjafjallajökull ash clouds observed over the Europe in April/May 2010. From these measurements, it came out that the Eyjafjallajökull ash cloud above Napoli had linear particle depolarization varying from 8% to 15%, and lidar ratio, at 355 nm and 532 nm, varying in the range 30-45 sr and 35-44 sr, respectively. Depolarization ratio and lidar ratio values were found to be lower than the same values measured in Northern Europe because of the particle growth due to hygroscopic behaviour and the long permanence in the atmosphere. Just emitted volcanic ashes were, instead, probed by the VAMP system at the Mt. Etna in the plumes emitted on 15 November 2010 from Bocca Nuova Crater (BNC) and North East Crater (NEC). Results highlight the simultaneous presence of weakly depolarizing (from BNC) and solid volcanic ashes (from NEC). From the latter, a maximum aerosol linear depolarization ratio of (45 $\pm$ 3)% was measured, with a value of 36 $\pm$ 5 sr (plume from NEC) for lidar ratio at 532 nm. Finally, preliminary results of the new AMPLE lidar system were presented, showing the functionality of the lidar in the operational field. The first prototype of AMPLE was sent to Beijing (PRC) were continuous measurements on Asian anthropogenic polluted particle are planned. The second copy of the system was delivered to Catania (IT) where it represent the highlight of a new automatic system for the monitoring and forecasting of volcanic ash dispersal between Sicily and Malta (VAMOS SEGURO project in the framework of 2007 - 2013 Italy - Malta (IT-MT) cooperation).

Bibliography

[1] Randall D., et al., *In Climate Change 2007: The Physical Science Basis. Contribution of Working Group I to the Fourth Assessment Report of the Intergovernmental Panel on Climate Change*. Ed. S. Solomon, D. Qin, M. Manning, Z. Chen, M. Marquis, K. Averyt, M.Tignor, and H. Miller, Cambridge University Press, Cambridge, United Kingdom and New York, NY, USA, 2007

[2] Wandinger U. *Introduction to Lidar, in Lidar Range-Resolved Optical Remote Sensing of the Atmosphere*, Claus Weitkamp Editor, Springer series in optical sciences, ISSN 0342-4111, 102, 2005

[3] Müller D., et al., *Microphysical particle parameters from extinction and backscatter lidar data by inversion with regularization: theory*, Appl. Opt. 38, 2346–2357, 1999

[4] Folch A, et al., *Volcanic ash forecast—application to the May 2008 Chaiten eruption*. Nat Hazards Earth Syst Sci 94, 109–117, 2008.

[5] D. Randall, et al., In *Climate Change 2007: The Physical Science Basis. Contribution of Working Group I to the Fourth Assessment Report of the Intergovernmental Panel on Climate Chang*e. Ed. S. Solomon, D. Qin, M. Manning, Z. Chen, M. Marquis, K. Averyt, M.Tignor, and H. Miller, Cambridge University Press, Cambridge, United Kingdom and New York, NY, USA, 2007

[6] Holben B.N., et al., *AERONET—A Federated Instrument Network and Data Archive for Aerosol Characterization.* Remote Sens. Environ. 66, 1, 1998.

[7]GAW, Report 178, Hamburg, Germany, 2007.

[8] Barnaba F., and G. P. Gobbi, *Aerosol seasonal variability over the Mediterranean region and relative impact of maritime, continental and Saharan dust particles over the basin from MODIS data in the year 2001*. Atmos. Chem.Phys, 4, no. 9-10, 2367, 2004.

[9] K. Schepanski, et al., *A new Saharan dust source activation frequency map derived from MSG-SEVIRI IR-channels*. Geophysical Research Letters, 34, 18, L18803, 2007.

[10] D.M. Winker, et al. *Overview of the CALIPSO Mission and CALIOP Data Processing Algorithms.* Atmos.Ocean.Technol, 26, 11, 2310, 2009

[11] Kinne, S., et al., *An AeroCom initial assessment – optical properties in aerosol component modules of global models*, Atmos. Chem. Phys., 6, 1815, 2006.

[12] WMO Secretariat, Atmospheric Research and Environment Branch, 2011

[13] Liou, K N., and Y. Takano, *Interpretation of cirrus cloud polarization measurements from radiative transfer theory.* Geophys. Res. Lett., 29.1313, doi:10.1029/2001GL014613, 2002.

[14] D. Randall, et al., *In Climate Change 2007: The Physical Science Basis. Contribution of Working Group I to the Fourth Assessment Report of the Intergovernmental Panel on Climate Change*. Ed. S. Solomon, D. Qin, M. Manning, Z. Chen, M. Marquis, K. Averyt, M.Tignor, and H. Miller, Cambridge University Press, Cambridge, United Kingdom and New York, NY, USA, 2007

[15] Junge C.E., J.E. Manson. *Stratospheric Aerosol Studies.* J. Geophys. Res., 66, 2163-2182 (1961)

[16] Whitby, K. T., "The Physical Characteristics of Sulfur Aerosols," *Atmospheric Environment*, Vol.12, pp. 135-159, 1978.

[17] Birmili W., H. Berresheim, *The Hohenpeissenberg Aaerosol Formation Experiment (HAFEX): a long-term study including size-resolved aerosol, H_2SO_4, OH, and monoterpenes measurements*. Atmos. Chem. Phys. Vol 3, pp 361-376, 2003.

[18] Lunt D. J., P.J. Valdes. *The modern dust cycle: Comparison of model results with observations and study of sensitivity.* J. Geophys.Res.107 (D23), 4667, doi: 10.1029/2002JD002316, 2002.

[19] Tegen I., R. Miller. *A general circulation model study of interannual variability of soil dust aerosol.* J. Geophys.Res.103, 25,975-25,995, 1998.

[20] Seinfeld, J. H. and S.N. Pandis, *Atmospheric Chemistry and Physics, From Air Pollution to Climate Change.* John Wiley & Sons, Inc., New York: 1998.

[21] Watson, J. G., and J. C. Chow. *Reconciling Urban Fugitive Dust Emissions Inventory and Ambient Source Contribution Estimates: Summary of Current Knowledge and Needed Research.* Desert Research Institute, Energy and Environmental Engineering Center, DRI Document No. 6110.4D2, 1999.

[22] Menut L., et al., *Urban boundary-layer height determination from lidar measurements over the Paris area.* App.Opt., 38 (6), 945-954, 1999.

[23] Wehr A., U. Lohr, *Airborne laser scanning—an introduction and overview,* ISPRS Journal of Photogrammetry & Remote Sensing 54. 68–82 (1999)

[24] Santacesaria V, Marenco F, Balis D, Papayannis A, Zerefos C, Nuovo Cimento, C 21, 6, 585 (1998)

[25] J. Ackermann , *The Extinction-to-Backscatter Ratio of Tropospheric Aerosol: A Numerical Study*. J. Atmos Ocean Technol , 15, 1043, 1998.

[26] http://www.nasa.gov/mission_pages/calipso/main/index.html

[27] D. M. Winker, et al., *Initial performance assessment of CALIOP*. Geophys. Res. Lett, 34, L19803, 2007.

[28] Müller D., B et al., *EARLINET observations of the 14–22-May long-range dust transport event during SAMUM 2006: validation of results from dust transport modeling*. Tellus, 61B, 325–339, 2009.

[29] Papayannis, A., et al., *Systematic lidar observations of Saharan dust over Europe in the frame of EARLINET (2000-2002)*. G., J. Geophys. Res. 113, D10204, 2008.

[30] A. Ansmann, et al., *Influence of Saharan dust on cloud glaciation in southern Morocco during the Saharan Mineral Dust Experiment*. Geophys. Res., 113, D04210, 2008.

[31] Seinfeld, John H. and al.,*ACE-ASIA - Regional climatic and atmospheric chemical effects of Asian dust and pollution*. Bulletin of the American Meteorological Society, 85 (3). pp. 367-380, 2004.

[32] Sassen, K., et al., *Volcanic ash plume identification using polarization lidar: Augustine eruption, Alaska*. Geophys. Res. Lett34 (L08803), 4, 2007.

[33] G. Pisani et al., *Lidar depolarization measurement of fresh volcanic ash from Mt. Etna, Italy*. Atmos. Environ. 62 34, 2012.

[34] S. Scollo, et al., *Monitoring Etna volcanic plumes using a scanning LiDAR*. Bull Volcanol, 74, 2383, 2012.

[35]Pappalardo G. et al, *Four-dimensional distribution of the 2010 Eyjafjallajökull volcanic cloud over Europe observed by EARLINET*, Atmos. Chem. Phys. Discuss., 12, 30203–30257, www.atmos-chem-phys-discuss.net/12/30203/2012/ doi:10.5194/acpd-12-30203-2012, 2012.

[36] Fiocco, G., L.D. Smulli'n. *Detection of Scattering in the Upper Atmosphere (60-140 km) by Optical Radar, Nature, 199, 1275, 1963*

[37] Barrett, E.W. and O. Ben-Dov. *Application of Lidar to Air Pollution Measurements*. Journal of Applied Meteorology, 6, 500-515, 1967

[38] Collis, R.T.H. *Lidar, Advances Geophysics, edited by H.E. Landsberg, and J. Van Mieghhem, 113-138, Academic Press, New York, 1969*

[39] Collins R.T.H., Russell P.B. *Lidar Measurement of Particles and Gases*. In "Laser Monitoring of the Atmosphere", Ed. E.D.Hinkley, Springer-Verlag, 1976.

[40] G.F. Bohren and D.R. Huffmann, *Absorption and Scattering of Light by Small Particles* -Wiley, New York, 1983.

[41] R.M. Measures. *Laser Remote Sensing.* Krieger Publishing Company, Malabar, Florida

[42] Ansmann A., et al., *Independent measurements of extinction and backscatter profiles in cirrus clouds by using a combined Raman elastic-backscatter LIDAR.* Appl. Opt. vol. 31, n. 33, 1992.

[43] D'Avino L. *Inversione di segnali lidar per la determinazione delle proprietà degli aerosol atmosferici.* PhD. Thesis. 2004.

[44] J.Hadamard. Sur les problemes aux derivees parielies et les leur signification physique. Bull. Univ. Princeton, 1902

[45] Müller D., et al., *Microphysical particle parameters from extinction and backscatter lidar data by inversion with regularization: theory.* Appl. Opt.Vol. 38, No. 12 , 1999.

[46] Böckmann C. *Hybrid regularization method for the ill-posed inversion of multiwavelength lidar date in the retrieval of aerosol size distributions.* Appl. Opt.Vol. 40, No. 9, 2001.

[47] Ligon D.A., et al., *Determination of aerosol parameters from light-scattering data using an inverse Monte Carlo technique*, Applied optics vol.35 n.21, 1996.

[48] Ligon D.A., et al., *Aerosol properties from spectral extinction and backscatter estimated by an inverse Monte Carlo method,* Applied optics vol.39 n.24, 2000.

[49] J.B. Gillespie, et al., *Development of a broadband lidar system for remote determination of aerosol size distributions,* Meas. Sci. Technol. 13, 2002, 383-390.

[50] F. Barnaba G.P. Gobbi, *Lidar estimation of tropospheric aerosol extinction, surface area and volume: Maritime and desert-dust cases,* Journal of Geophysical Research, vol. 106 n.D3, 2001.

[51] Ansmann A., et al., *Measurement of atmospheric aerosol extinction profiles with a Raman lidar.* Opt. Lett. 15, 746-748, 1990.

[52] Ansmann A., et al., *Independent measurements of extinction and backscatter profiles in cirrus clouds by using a combined Raman elastic-backscatter LIDAR*. Appl. Opt. vol. 31, n. 33, 1992.

[53] Ferrare R.A., S.H. Melfi, D.N. Whiteman, K.D. Evans, R. Leifer, and Y.J. Kaufman. *Raman lidar measurements of aerosol extinction and backscattering, Part 1, Method and comparison.* J. Geophys. Res. 103, 19, 663- 19,672, 1988.

[54] Ansmann A., U. Wandinger. *Combined Raman Elastic Backscatter LIDAR for vertical profiling of moisture, aerosol extinction, backscatter and lidar ratio.* Appl. Phys.B, 55,18-28, 1992.

[55] Fenner, W. R., H. A. Haytt, et al., *Raman cross sections of simple gases*, Journal of the Optical Society of America 63(1): 73-77, 1973.

[56] Krichbaumer, W. and C. Werner, *Current state of-the-art of lidar inversion methods for atmospheres of arbitrary optical density*, Applied Physics B-Lasers and Optics 59: 517-523, 1994.

[57] Sasano, Y., Browell, E., V., and Ismail S., *Error caused by using a constant extinction/backscattering ratio in the lidar solution*, Applied Optics 24(22), 3929-3932, 1985.

[58] Fernald F. G., *Analysis of atmospheric lidar observations: some comments*. Appl. Opt., vol. 23, No. 5, 1984

[59] Klett J. *Stable analytic inversion solution for processing lidar returns*. Appl. Opt., vol. 20, No.2, 1981.

[60] V. A. Kovalev. *Lidar measurements of the vertical aerosol extinction profiles with range-dependent backscatter-to extinction ratios.* Appl. Opt. 32, 6053-6065, 1993.

[61] Ackermann J., *The Extinction-to-Backscatter Ratio of Tropospheric Aerosol: A Numerical Study.* American Meteorological Society, 1043-1050, 1998.

[62] Müller D., et al., *Aerosol-type-dependent lidar ratios observed with Raman lidar*, Jour. Geoph. Res., 112, D16202, doi:10.1029/2006JD008292, 2007.

[63] Sassen, K., *Polarization lidar*. In: Weitkamp, C. (Ed.), LIDAR Range-Resolved Optical Remote Sensing of the Atmosphere. Springer, NY, USA, pp. 19e42, 2005.

[64] Biele, J., et al., *Polarization lidar: corrections of instrumental effects*. Optics Express 7, 427e435. http://dx.doi.org/10.1364/ OE.7.000427, 2000.

[65] Behrendt A. and Nakamura T. *Calculation of the calibration constant of polarization lidar and its dependency on atmospheric temperature*. Optics Express 10(16), 805-817, 2002

[66] Omar, A. H., *Observations by the LIDAR in-Space Technology Experiment (LITE) of high-altitude cirrus clouds over the equator in regions exhibiting extremely cold temperatures*. J. Geophys. Res., 106 (D1), 1227-1236, 2001.

[67] Santacesaria V., et al., *A climatological study of polar stratospheric clouds (1989-1997) from LIDAR measurements over Dumont d'Urville (Antarctica)*. Tellus (B), 53 (3), 306-321, 2001.

[68] Douglass L. R., et al., *A composite view of ozone evolution in the 1995-1996 northern winter polar vortex developed from airborne LIDAR and satellite observations*. J. Geophys. Res., 106 (D9), 9879-9895, 2001.

[69] Barnaba F, and G. P. Gobbi. *LIDAR estimation of tropospheric aerosol extinction, surface area and volume: Maritime and desert-dust cases*. J. Geophys. Res., 106 (D3), 3005-3018, 2001.

[70] Boselli A., et al. *Characterization of atmospheric aerosol in the urban area of Napoli in the framework of EARLINET Project*. SPIE Vo. 5235, pp. 643-650, 2004.

[71] Bösenberg J. and V. Matthias. *EARLINET: A European Aerosol Research Lidar Network to Establish an Aerosol Climatology*. Contract EVR1-CT1999-40003 Final report. June 23, 2003.

[72] Halldorsson T. and J. Langerholc. *Geometrical form factor for the lidar function.* Appl. Opt., 240-244,1978.

[73] U. Wandinger, A. Ansmann. *Experimental Determination of the Lidar Overlap Profile with Raman Lidar*. Applied Optics, vol. 41, n. 3, 2002.

[74] Melfi J. D. ,et al. *Observation of Raman Scattering by Water Vapor in the Atmosphere*. Applied Physics Letters. 15, 9, 295-297, 1969.

[75] http://weather.uwyo.edu/upperair/europe.htmlS. H

[76] Sassen K., 2000, *Lidar backscatter depolarization technique. Light Scattering by Nonspherical Particles*, M.I.Mishchenko, J.W.Hovenier and L.D.Travis, Academic Press, 393-416

[77] McGill, et al, *The cloud physics lidar: Instrument description and initial measurement results*. Appl. Opt., 41, 3725–3734, 2002.

[78] Sassen K., and S. Benson, *A midlatitude cirrus cloud climatology from the Facility for Atmospheric Remote Sensing. Part II: Microphysical properties derived from lidar depolarization*. J. Atmos. Sci., 58, 2103–2112, 2001.

[79] Eloranta, E. W., and P. Piironen, *Depolarization measurements with the high spectral resolution lidar*. Abstracts, 17th Int. Laser Radar Conf., Sendai, Japan, Laser Radar Society of Japan, ICLAS, NASDA, and NIES, 127–128, 1994.

[80] Beyerle, G., et al., *A lidar and backscatter sonde measurement campaign at Table Mountain during February–March 1997: Observations of cirrus clouds*. J. Atmos. Sci., 58, 1275–1287, 2001.

[81] Sauvage, Let al., *Remote sensing of cirrus radiative parameters during EUCREX'94. Case study of 17 April 1994. Part I: Observations*. Mon. Wea. Rev., 127, 486–503, 1999.

[82] Behrendt, A., Nakamura, T., *Calculation of the calibration constant of polarization lidar and its dependency on atmospheric temperature*. Optics Express 10 (16), 805e817, 2002.

[83] Spinhirne, J. D., et al., *Cloud top remote sensing by airborne lidar*. Appl. Opt., 21, 1564–1571, 1982.

[84] Alvarez, JM et al. *Calibration technique for polarization-sensitive lidars*. Journal of Atmospheric and Oceanic Technology, 23, 5, 683-699, Doi: 10.1175/JTECH1872, 2006.

[85] Freudenthaler, V., et al., *Depolarization ratio profiling at several wavelengths in pure Saharan dust during SAMUM 2006*. Tellus 61B, 165e179, 2009.

[86] Pica G., et al., *New prototype of very compact LIDAR for atmospheric particulate monitoring*, Journal of Optoelectronics and Advanced Materials, Vol. 10, No. 11, p. 3111 – 3116, 2008.

[87] Behrendt, A., Nakamura, T., 2002. *Calculation of the calibration constant of polarization lidar and its dependency on atmospheric temperature*. Optics Express 10 (16), 805e817.

[88] http://www.radiantzemax.com/

[89]Draxler, R.R. and Rolph, G.D., *HYSPLIT (HYbridSingle-Particle Lagrangian Integrated Trajectory)* Model access via NOAA ARL READY Website (http://ready.arl.noaa.gov/HYSPLIT.php), NOAA Air Resources Laboratory, Silver Spring, MD, 2011.

[90] Mona L., et al., *Multi-wavelength Raman lidar observations of the Eyjafjallajökull volcanic cloud over Potenza, Southern Italy*. Atmos. Chem. Phys., 12, 2229–2244, www.atmos-chem-phys.net/12/2229/2012/ doi:10.5194/acp-12-2229-2012, 2012.

[91] Ansmann A., et al., *Ash and fine-mode particle mass profiles from EARLINET-AERONET observations over central Europe after the eruptions of the Eyjafjallajökull volcano in 2010*. Journal of Geophysical Research, 116, D00U02, doi:10.1029/2010JD015567, 2011.

[92] Wiegner, M., et al., *Characterization of the Eyjafjallajökull ash-plume: Potential of lidar remote sensing,* Physics and Chemistry of the Earth, V. 45–46, 79–86, doi:10.1016/j.pce.2011.01.006, 2012.

[93] Tesche M., et al., *Vertical profiling of Saharan dust with Raman lidars and airborne HSRL in southern Morocco during SAMUM*, Tellus, 61B, 144–164, 2009.

[94] Andronico, D., and D. Lo Castro, *Analisi tessiturale della cenere emessa dal Cratere di NE il 14-15 novembre 2010*, INGV-Prot. int. n° UFVG2010/34, Catania, Italy, 2010.

[95] Behncke B., et al., *Osservazioni in area sommitale dell'Etna, 12 novembre 2010*, INGV-Prot. Int. n° UFVG2010/33, 2010.

[96] Di Girolamo, P., et al., *Two wavelength lidar analysis of stratospheric aerosol size distribution.* Journal of Aerosol Science, 26, 6, 989-1001, 1995.

[97] Bissonnette, L. R., *Lidar and Multiple scattering*, in Lidar Range-Resolved Optical Remote Sensing of the Atmosphere, edited by Claus Weitkamp, pp. 43-103, Springer, NY, USA, 2005.

[98] Chester DK, et al., *Mount Etna, Anatomy of a Volcano*, Stanford University Press, Stanford, California,1985.

[99] Oppenheimer, C., *Volcanic Degassing*, in: Turekian, K.K., Holland, H.D. (Eds), Treatise On Geochemistry, Vol.3, Elsevier Ltd, Amsterdam, Netherlands, 2003.

[100] Miffre, A., et al., *Atmospheric non-spherical particles optical properties from UV-polarization Lidar and scattering matrix*. Geophysical Research Letters, 38, L16804, doi:10.1029/2011GL048310, 2011.

[101] Tesche, M., et al., *Separation of dust and smoke profiles over Cape Verde by using multiwavelength Raman and polarization lidars during SAMUM 2008*. Journal of Geophysical Research, 114, D13202, doi:10.1029/2009JD011862, 2009.

[102] Scollo S., et al., *Terminal settling velocity measurements of volcanic ash during the 2002–2003 Etna eruption by an X-band microwave rain gauge disdrometer*. Geophisical Research Letters. 32, L10302, doi:10.1029/2004GL022100, 2005.

[103] Bonadonna, C. and Phillips, J.C., *Sedimentation from strong volcanic plumes*. Journal of Geophysical Research, 108, B7, 2340, doi:10.1029/2002JB002034, 2003.

[104] Gasteiger, J., et al. *Volcanic ash from Iceland over Munich: mass concentration retrieved from ground-based remote sensing measurements*. Atmospheric Chemistry and Physics, 11, 2209–2223, doi:10.5194/acp-11-2209-2011, 2011

[105] Schumann, U. et al. *Airborne observations of the Eyjafjalla volcano ash cloud over Europe during air space closure in April and May 2010*. Atmospheric Chemistry and Physics, 11, 2245–2279, doi:10.5194/acp-11-2245-2011.